Spring 5-13-2017

Adsorption and Wetting in Model Mesoporous Silicas and in Complex Metal Oxide Catalysts

Karthik Jayaraman
Seton Hall University, jayaraka@shu.edu

Adsorption and Wetting in Model Mesoporous Silicas and in Complex Metal Oxide Catalysts

By:

Karthik Jayaraman

Dissertation submitted to the Department of Chemistry and Biochemistry of Seton Hall University in fulfillment of the requirements for the degree of

Doctor of Philosophy

Spring 2017

South Orange, New Jersey

Dedication (to my well-wishers)

My parents Mr. N. Jayaraman &
Mrs. J. Jayam

My wife Ramya

My mentor Frank Tomasella Ph.D. at
Bristol Myers Squibb

My brother Ganesh

na coryahāryaṃ na ca rājahāryaṃ na bhrātṛbhājyaṃ na ca bhārakāri |
vyaye kṛte vardhate eva nityaṃ vidyādhanaṃ sarvadhanapradhānam ||
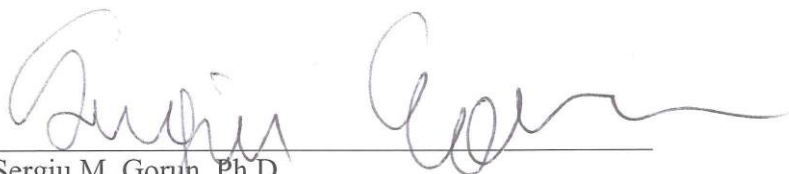
– an Ancient Indian adage.

Not stolen by thieves, not seized by kings, not divided amongst brothers, not heavy to carry. The more you spend, the more it flourishes always --- the wealth of knowledge is the most important among all kinds of wealth.

We certify that we have read this dissertation and that in our opinion it is sufficient in scientific scope and quality as a dissertation for the degree of Doctor of Philosophy.

APPROVED

_____
Alexander Y. Fadeev, Ph.D.
Research Mentor

_____
Sergiu M. Gorun, Ph.D.
Co-Research Mentor

_____
David Sabatino, Ph.D.
Member of Dissertation Committee

_____
Cecilia Marzabadi, Ph.D.
Chair, Department of Chemistry and Biochemistry

Acknowledgments

I extend my sincere thanks to Professor Alexander Y Fadeev for being my research advisor and for challenging my thinking, writing and research skills. I also thank him wholeheartedly for providing me valuable guidance, and encouragement throughout this work. Prof. Fadeev was always available to provide assistance to comprehend the concepts and techniques to carry out the research.

I would like to thank Professor Sergiu M Gorun for his willingness to share his research expertise by being a part of my research (related to phthalocyanines) and dissertation examining committee. My genuine gratitude goes to Professor Yuri V Kazakevich, Professor David Sabatino and Professor Stephen P Kelty for being part of my dissertation matriculation committee and enabling me to progress with my research.

This work has benefitted from discussions with and help from fellow graduate students: Gabe Graffius, Henry Grau, Edwin Vega and Frank Bernardoni. I would also like to acknowledge Erik Carrion from Dr. Gorun's research group for synthesis and isolation of the phthalocyanines. My profound acknowledgment goes to the Seton Hall University, specifically the Department of Chemistry and Biochemistry, which has been a great place of learning.

I would like to thank Bristol-Myers Squibb (BMS) Company for supporting my PhD by providing doctoral fellowship and access to instruments in the lab. I would like to thank Dr. Frank Tomasella at BMS for fueling my interest in pursuing PhD, for suggesting Seton Hall University and motivating me periodically to stay on the path to complete the doctoral degree. I would like to thank Dr. Shasad Sharif at BMS who assisted me immensely to become familiar with much of the instrumentation or equipment required to perform my experiments.

Abstract

The surface of most metal oxides is covered by hydroxyl groups which influence many surface phenomena such as adsorption and wetting, catalysis and surface reactions. Surface chemistry of silica is a subject of exhaustive studies owing to a wide variety of practical applications of silica. In Chapter 1, a brief review of classification, synthesis and characterization of silica is provided. The hydroxylation of silica surface i.e the number of hydroxyl (-OH) groups on the surface is of utmost importance for its practical applications. In Chapter 2, a brief introduction to surface hydration of silica is provided followed by the gas adsorption measurements and characterization.

Pore wetting is critical to many applications of mesoporous adsorbents, catalysts, and separation materials. In the work presented in Chapter 3, we employed the combined vapor adsorption study using nitrogen (77K) and water (293K) isotherms to evaluate the water contact angles for a series of ordered mesoporous silicas (ex:SBA-15). The proposed method of contact angle relies on the statistical film thickness (t-curve) of the adsorbed water. There were no t-curves for water for dehydroxylated or hydrophobic surfaces in literature and we addressed this issue by measuring t-curves for a series of model surfaces with known and varying silanol coverage. Using the radius of menisci ((H_2O)), statistical film thickness t(H_2O) from water isotherm, and the true radius of pores ($r_p(N_2)$), from nitrogen isotherms, the water contact angle inside pores were calculated. As it was anticipated, the results obtained showed that the silica pore contact angles were strongly influenced by the number of the surface silanol groups and, therefore, by the thermal and hydration treatments of silicas.

Phthalocyanines (Pcs) present an interesting class of catalytically active of molecules with unique spectroscopic, photoelectric, and sometimes magnetic properties. In the work

presented in Chapter 4, we have undertaken a systematic study to explore the possibility of preparing a supported catalyst material i.e loading fluorinated metal phthalocyanines onto metal oxide surfaces by two other techniques in addition to solution adsorption. Techniques or procedures that have been used to immobilize MPcs include: i) physical adsorption (from solution) onto metal oxide surface, ii) deposition by pore filling and encapsulation and iii) mesopore entrapment or confinement. The MPcs are loaded on to metal oxides with an aim to: a) maximize the surface area of the Pcs by distributing it over the support, b) immobilize the Pcs so that they do not leach into the solution environment, c) improve the thermal stability of the Pcs and d) attempt to achieve single-site catalysis. All the immobilization techniques were carried out with $F_{64}PcZn$ as the model MPc, acetone as the immobilization solvent and silica or alumina as adsorbents (solid support).

An understanding of gas adsorption mechanisms on metal phthalocyanines (MPcs) is essential for their practical application in biological processes, gas sensing, and catalysis. In this work, the surface characteristics were probed by performing nitrogen and water adsorption on the free-form MPcs (without immobilization on solid support) and characterization of their physical properties. The combined vapor adsorption study (developed in Chapter 3) enabled in understanding the affinity of Pcs towards water vapor i.e number of water molecules adsorbed per phthalocyanine molecule was obtained. This information is very relevant towards using Pcs as catalyst since water vapor is guaranteed to be present in most of the catalytic reaction environment.

Table of Contents

List of Figures

List of Tables

List of Symbols and Abbreviations

IUPAC	International Union of Pure and Applied Chemistry
SBA-15	Santa Barbara Amorphous number 15
MCM-41	Mobil Crystalline Materials number 41
VPI-5	Virginia Polytechnic Institute number 5
JDF-20	Jilin David Faraday number 20
M41S	Mesoporous class of materials
MCM-50	Mobil Crystalline Materials number 50
MCM-58	Mobil Crystalline Materials number 58
MSU	Michigan State University
KIT	Korea Advanced Institute of Science and Technology
FDU	Fudan University
AMS	Anionic-surfactant-templated Mesoporous Silica
HA	Hyaluronic Acid
TEOS	Tetra Ethoxy Ortho Silane
BET	Brunauer, Emmett and Teller
TGA	Thermo Gravimetric Analysis
IR	Infra-Red
DTG	Differential Thermo Gravimetric
BJH	Barret, Joyner and Halenda
TMS	TriMethylSilyl
WL	Weight Loss (in TGA)
MW	Molecular weight
PSD	Pore Size Distribution
CA	Contact Angle
PC or Pc	Phthalocyanine
PCS or Pcs	Phthalocyanines
MPC or MPc	MetalloPhthalocyanine
MPCs or MPcs	MetalloPhthalocyanines
CSA	Cross-Sectional Area
ΔH	Change in Enthalpy
ΔS	Change in Entropy
ΔG	Gibbs Free Energy
n	Quantity of gas adsorbed in moles per gram of adsorbent
n_m	Monolayer capacity
p	Vapor pressure
p^o	Saturation vapor pressure of the adsorptive
a_1	Condensation coefficient
R	Gas constant
k	Constant given by kinetic theory of gases
q_1	Isoteric heat of adsorption
T	Temperature

z_m	Number of sites per unit area
p	Vapor pressure
v_1	Frequency of oscillation
c	c-constant
N_A	Avogadro constant
a_m	Adsorbate molecular area
v_m	Volume of gas(reduced to STP)
γ	Surface tension of the liquid adsorptive
r_m	Radius of menisci
p/p^o	Relative vapor pressure
r_c	Radius of the core
r_p	Radius of the pore
θ	Contact angle
V_L	Molar volume of the liquid adsorptive
t	Adsorbed film thickness or statistical thickness
ρ	Grafting density
S or S_{BET} or $S(N_2)$	BET surface area
n_c	Number of carbon atoms
%C	Carbon weight percent
n_{OH}	Amount of surface silanols
$V_{ads.liq.}$	Amount of liquid water adsorbed in cm^3/g
Γ	Amount of water adsorbed in $\mu mole/m^2$
f_1	Solid-liquid interface fraction
f_2	Air-liquid interface fraction
h	Average thickness of grafted layer
C_o	Liquid phase concentration of Pc at initial condition
C_e	Liquid phase concentration of Pc at equilibrium condition
V	Volume of Pc solution
W	Mass of dry adsorbent
R	Absolute reflectance of the sampled layer
k	Molar absorption coefficient
s	Scattering coefficient
ω	Cross-sectional area
Γ_{max}	Maximum monolayer adsorption capacity in $\mu mole/m^2$
$V(N_2)$	Pore Volume by nitrogen adsorption
$r(N_2)$	Radius by nitrogen adsorption

Chapter 1: Classification, Synthesis and Characterization of Silica

1.1 Introduction to Silica

Silicon dioxide (SiO_2) or silica is the most abundant of all the oxide minerals in the earth's crust. Besides being the abundant metal oxide, silica is very important to life. The human body consists of about half gram of silica that promotes the formation and growth of bones, hair and teeth. The solubility of silica in water is adequate enough to play important roles in many forms of life. The term silica encompasses silicon dioxide in its natural, synthetic, crystalline or amorphous and chemically combined forms in which the silicon atom is surrounded by four or six oxygen atoms[1]. Solid silica can be classified on the basis of four main attributes namely crystal structure, dispersity, surface composition and porosity[2].

1.1.1 Classification based on the crystal structure

Silica is classified as crystalline or amorphous (non-crystalline). Crystalline silica is found in nature and also exist as synthetic forms. Quartz, tridymite, cristobalite are three main crystalline silicas found naturally and each have different polymorphic forms that are stable in different temperature ranges. The transformation between three silica forms and the vitreous silica glass at atmospheric pressure is show below:

$$\text{quartz} \underset{870°C}{\rightleftharpoons} \text{tridymite} \underset{1470°C}{\rightleftharpoons} \text{cristobalite} \underset{1700°C}{\rightleftharpoons} \text{vitreous} \qquad \textbf{(1-1)}$$
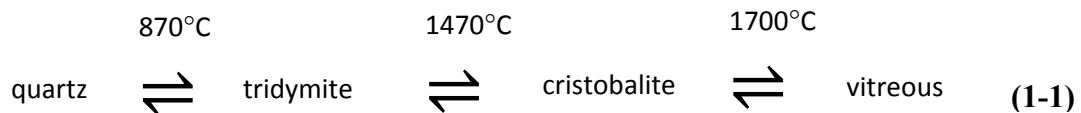
Keatite, coesite and stishovite are synthetic crystalline silicas with well-ordered structures[2-3]. The crystalline form involves a high degree of ordering and the surface area is limited to the external surface of the crystalline particles. With the exception of stishovite and coesite which has a six

fold octahedral coordination of the silicon, in all other silicas the silicon atom is surrounded by four oxygen atoms forming the $[SiO_4]^{4-}$ tetrahedral unit[1] as shown in Figure 1.

Quartz glass (super cooled liquid silica) is an intermediate between crystalline and amorphous form. Opal (naturally occurring silica) and synthetic silicas such as silica gels, pyrogenic silicas and precipitated silica are some examples of amorphous silica. They lack regular ordered structure and exhibits higher degree of hydration as compared to crystalline silica[2-3]. Amorphous silica forms are porous and the porosity introduces a large surface area inside the particles[4]. In both amorphous and crystalline silicas, each silicon atom and each oxygen atom have essentially the same local surroundings, however, there is no long-range periodicity in the amorphous structure.
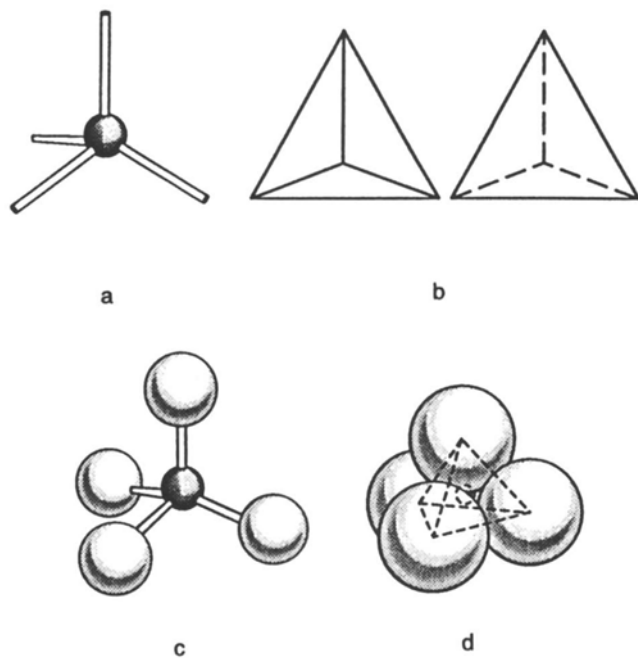
Figure 1. Methods of representing the tetrahedral coordination of oxygen ions with silicon: (a) ball and stick model, (b) solid tetrahedron, (c) skeletal tetrahedron, and (d) space-filling model based on packed sphere. Adapted from ref. [1].

1.1.2 Classification based on dispersity

Silica can be classified as soluble silica, silica sols, silica gels (hydrogels, xerogels, and aerogels), precipitated silica and pyrogenic silicas. Soluble silica is a molecular solution of silica (mainly monosilicic acid at low concentrations) formed when amorphous or crystalline silica comes in contact with water. It is neutral, hydrophilic, non-ionized and cannot be isolated from water[2-3]. Silica sols consists of discrete silica particles that are amorphous, non-porous and spherical in shape. Silica sols are made by partially neutralizing a dilute solution of soluble silicates with acid to a pH of 8-9. Under these conditions, polysilicic acids are formed by polycondensation and grows into colloidal silica particles[2-3].The behavior of silica sols is greatly dependent on pH and a small change in pH converts the sol into a gel or a solution.

Stabilization of silica sols to prevent aggregation, involves understanding of the surface chemistry of silica and the nature of interaction of silica and water over a wide pH range. If the silica sols are not stabilized, the dispersed silica particles will aggregate by one of the typical aggregation processes namely gelling, coagulation, flocculation or coacervation. When the aggregation happens via the process of gelling, the silica particles are linked to one another leading to three dimensional packing of silica and finally results in a gelatinous mass called silica gel. The gel is formed when two silica particles with sufficiently low charges collide with each other to form siloxane bonds, holding the particles irreversibly bonded. This gel is referred to as hydrogel or organogel if the continuous liquid phase is water or an organic solvent respectively. The rate of gel formation depends on pH, particle size, silica concentration, electrolytes, organic liquids and temperature. For example, the rate of gel formation (in the pH range 3-5) increases with pH and is proportional to the concentration of hydroxyl ions[3]. A xerogel is obtained when a gel is dried by evaporation under normal conditions and a xerogel is reduced in volume by factor of 5 to 10

compared to the original wet gel[1]. The reduction or shrinkage is a result of stresses exerted by capillary tension in the liquid during drying. An aerogel is obtained when a gel is dried by evaporation in an autoclave above the critical point of the liquid, so that there is no capillary pressure leading to minimal or no shrinkage of the gel structure.

Precipitated silicas are obtained from a solution phase such as sodium silicate solution, fluoride solution, organic liquids and colloidal silica sols by the process of precipitation. The presence of a coagulant such as sodium ions, ammonium salts, calcium salts, polyvalent metal ions or organic materials is crucial for silica to precipitate from the solution phase[1].

Pyrogenic silicas are made at high temperatures by precipitation of silica from the vapor phase. They are colloidal dispersion of particles in the gas phase and can be referred to as aerosols. Pyrogenic silica can be obtained by one of the many processes such as vaporization of SiO_2, oxidation of SiO vapor, oxidation and hydrolysis of $SiCl_4$ vapor or silicon ester vapors, hydrolysis of SiF_4 vapors[1, 3]. The most commonly used pyrogenic silicas or fumed silicas are made by the flame hydrolysis process which involves oxidation and hydrolysis of $SiCl_4$ vapors[5]. Aerosil and Cab-O-Sil produced by Evonik industries and Cabot Corporation respectively are the most widely used fumed silicas. The preparation of fumed silica is discussed in detail in the section 1.2. Arc silicas are made by the reduction of high purity sand and plasma silicas are ultra-fine silica powders obtained by direct volatilization of sand in a plasma jet.

Among the various silicas discussed above, there is variation in physical properties from one type to another due to the inherent differences in the process of making these silicas. The size of the primary particle, density and degree of agglomeration and aggregation decides the porosity and specific surface area of these silicas. For example, xerogels and aerogels have a porous

structure, while fumed silica has a non-porous structure. Table 1 illustrates the differences in the physical properties of silica obtained through different methods[4].

Table 1. Physical properties of various silicas[4].

Characteristics		Pyrogenic silicas		Silicas made by wet method		
		fumed silica	arc silica	precipitated silica	xerogels	aerogels
Specific BET area	m^2/g	50 to 600	25 to 300	30 to 800	250 to 1000	250 to 400
Size primary particles	nm	5 to 50	5 to 500	5 to 100	3 to 20	3 to 20
Size aggregation/ agglomeration	μm	NA	2 to 15	1 to 40	1 to 20	1 to 15
Density	g/cm^3	2.2	2.2	1.9 to 2.1	2.0	2.0
Volume	ml/ 100g	1000 to 2000	500 to 1000	200 to 2000	100 to 200	800 to 2000
Mean pore diameter	nm	non porous till ca. 300 m^2/g	non porous	>30	2 to 20	> 25
Pore diameter distribution		NA	NA	very broad	narrow	narrow
Shape of interior surface		0	0	poor	very much	much
Aggregation and agglomeration structure		Chain-like agglomeration (open surface)	Dense spherical aggregates/ particles non-agglomerated	Slightly aggregated nearly spherical particles	highly porous agglomerated particles	macroporous agglomerated particles

NA- not applicable

1.1.3 Classification based on surface composition

The hydrated silica surface without any surface modification consists of physically adsorbed surface water and hydroxyl groups (silanols) that are bonded to a silicon atom in different ways. The silanols ($\equiv$Si-OH) are involved in a temperature dependent dehydroxylation-hydroxylation reaction written as

$$2 \equiv \text{Si-OH} \quad \rightleftharpoons \quad \equiv \text{Si-O-Si} \equiv \; + \text{H}_2\text{O} \qquad \textbf{(1-2)}$$
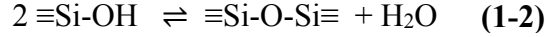
As dehydroxylation occurs (by heating or annealing), silanols are converted to less polar siloxane groups ($\equiv$Si-O-Si$\equiv$). The number and type of surface silanols and surface siloxane groups varies from silica to silica depending on the synthesis process and post synthesis treatment procedures[6]. Based on the surface water, hydroxyl groups and siloxane linkages, silica can be broadly classified as hydroxylated or partially dehydroxylated or fully dehydroxylated silica. Generally, a completely hydroxylated silica can be considered as a hydrophilic surface and removal of hydroxyl groups by the process of dehydroxylation leads to surface with hydrophobic properties. In this research, chapter 3 is focused on obtaining well defined silica surfaces with various degree of surface hydroxylation.

Chemical modification of a silica surface is described as covalent bonding of certain functional groups on to the silica surface as a result of chemical reaction between surface species and an appropriate surface modifier. Based on the bond by which functional groups are attached at the surface silicon atoms[2], they can be categorized as: (1) $\equiv$Si$-$O$-$C$\equiv$ (2) $\equiv$Si$-$C$\equiv$ and (3) $\equiv$Si$-$N=. In the history of silica chemistry, chemical modification is mainly performed to alter the wettability of silica products depending on the end use. Numerous types of silica are widely used as adsorbents in liquid chromatography, catalytic bed supports, fillers for polymeric systems, co-binders in nonstick coatings, enhancers in paper manufacturing processes, stabilizers (for weave structures) in textiles, as well as dispersant in pigments and fillers, binding agents for molding materials etc[6]. Hence, chemical modification of the surface of silica has gained significant attention in order to meet the technological demands for making several novel silica materials.

1.1.4 Classification based on porosity

All solids can be classified in two categories: porous and non-porous solids. Solid silica with a pore system is defined as porous silica and solid silica without a pore system is non-porous silica. The presence or absence of a pore system depends on the process used to obtain the silica material. An assembly of smooth discrete particles or chain like agglomeration of primary silica particles results in non-porous structures. Fumed silicas such as aerosil are non-porous, possess no interior surface and specific surface area is simply the external surface of the particles.

Porosity originates when dispersed silicas particles are compacted together. The pore space is being created by the interstices and voids between the particles. The three measure of a porous material are surface area, pore size and its distribution and pore volume[7]. As per IUPAC classification, pores are classified as below in Table 2.

Table 2. Pores as per IUPAC classification.

Type of Pores	Width
Micropores	< 2 nm
Mesopores	2- 50 nm
Macropores	> 50 nm

Each pore size range corresponds to a characteristic adsorption mechanism and this forms the basis of this classification. The width would correspond to the diameter in case of the cylindrical pores and the distance between opposite walls in case of slit pores[8]. The specific surface area of porous silica is a combination of both exterior and interior surface with major contribution from the interior surface.

The type of pores[7] can be further classified as open and closed as shown in Figure 2. Open pores are accessible whereas closed pores are inaccessible. Open pores can be inter-connected, passing or can form dead ends. The shape of pores[7] in a silica material could be cylindrical, conical, spherical (ink bottle), interstices and slits as shown in Figure 3.
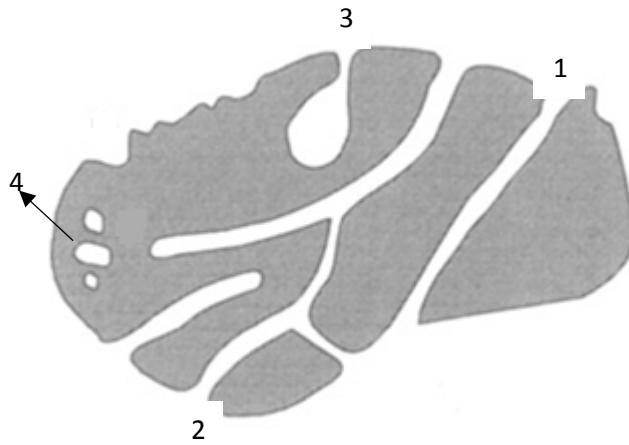
Figure 2. Cross section of a hypothetical porous material showing various types of pores[7] 1) Open passing 2) Open interconnected 3) Open dead end and 4) Closed pores.
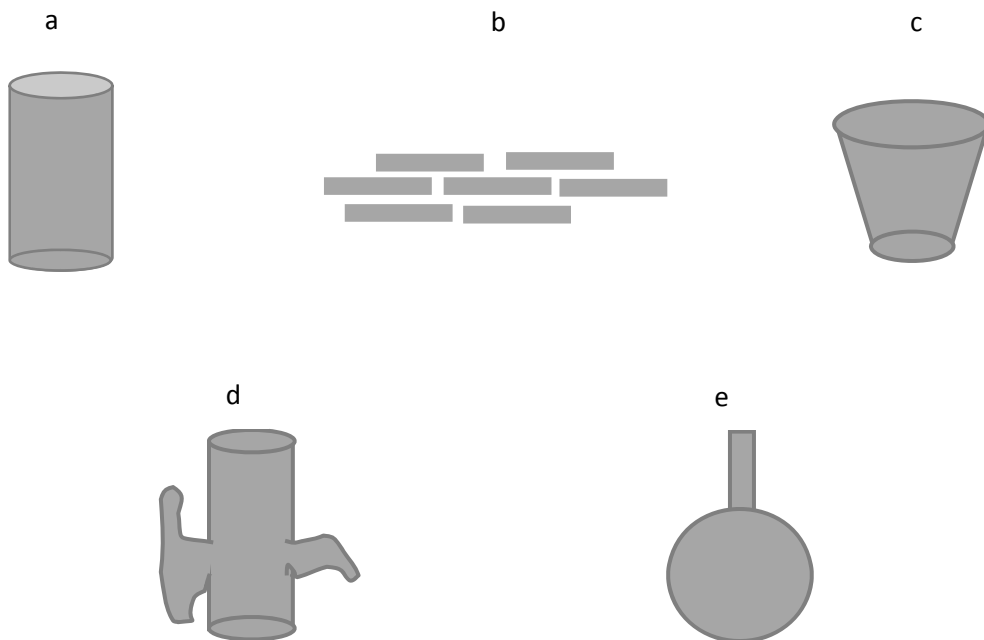
Figure 3. Shapes of Pores[7] a) Cylindrical b) Slit c) Conical d) Interstices e) Ink Bottle (Spherical).

Zeolites are a classic example of microporous materials. Zeolites are microporous inorganic crystalline materials containing Si, Al and O atoms in their framework. Zeolites have well defined pore structures with large surface area and they are used in shape selective catalysis. With the advent of a wide variety of new zeolites (types A, X and Y) they were used in large scale for separation and purification of small molecules[9]. The small pore size of zeolites (0.4 nm in Zeolite A) were initially attractive for some commercial applications as they paved the way for selective adsorption of gas molecules based on small size differences. However, with the increased interest to use zeolites in applications like separation of heavy metal ions, separation and selective adsorption of large organic molecules from waste water, cracking activity in oil industry, the smaller pore size turned out to be a limiting factor. Research studies were done to expand the pore sizes of zeolites which eventually paved way to some ultra large pore zeolites (0.8–1.3 nm) like VPI-5, JDF-20 etc. However these large pore zeolites did not find any significant applications due to poor stability and weak acidity [9].

In 1992, M41S family of silicate/aluminosilicate mesoporous molecular sieves with large uniform pores structures were discovered by researchers at Mobil Corporation[10-11]. The synthesis of M41S type materials is based on the combination of the sol-gel science and surfactant templating science. Unlike in zeolite synthesis where single molecules serve as templates, surfactant liquid-crystal structures serve as organic templates in the synthesis of these M41S type materials[12]. Using a self-assembled surfactant molecular array, a series of M41S materials namely MCM-41 (hexagonal), MCM-48 (cubic) and MCM-50 (lamellar) were synthesized[13]. Figure 4 shows the graphic representation of the M41S family type of silicas[12].
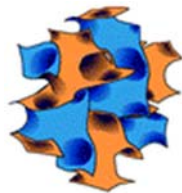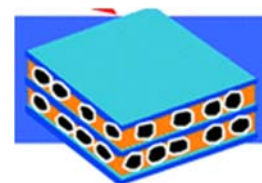
MCM-41	MCM-48	MCM-50

Figure 4. Schematic representation[12] of M41s family of materials.

The hexagonal mesophase MCM-41 consists of highly regular arrays of uniformly sized channels with diameters ranging from 1.5-10 nm depending on the templates used. The pores of MCM-41 are larger than those present in conventional synthetic zeolites thereby offering new opportunities for applications such as adsorption, catalysis, sensing, and separation. In 1998, a group of researchers at University of California, Santa Barbara produced another type of hexagonal array pores called the Santa Barbara Amorphous number 15 (SBA-15)[14]. SBA-15 was synthesized using amphiphilic triblock copolymers (Pluronic P-123) in strong acidic media. SBA-15 was found to possess larger pore size (4.6-30 nm) with thermal, mechanical and chemical resistance properties. SBA-16 was synthesized using the triblock copolymer Pluronic F-127 and has spherical pores arranged in body centered cubic structures[14]. In addition to MCM and SBA type silicas, there are many other families of mesoporous silicas such as MSU[15], KIT[16], FDU[17], AMS[18] synthesized by varying the synthesis conditions and type of surfactants. This breakthrough in the synthesis of mesoporous silica materials with controlled particle size, morphology, and porosity, along with their chemical stability, has made mesoporous silica matrices highly attractive for a wide variety of nanotechnological applications. One major limitation of mesoporous materials is their low thermal and hydrothermal stability owing to their amorphous morphology.

Macroporous materials are prevalent in nature (e.g. opals) and they have also been synthesized by various laboratory techniques. However, with the advent of meso micro and nano

10

porous materials in the last few decades, macroporous solids lost their appeal for a while. However, inspired by the hierarchical structure of biological materials, mechanical performance as well as diffusion limits within micro and mesopores, the interest in macroporous materials has recently increased. Microporous catalysts are less suited for liquid-phase processes of large molecules. Mesoporous materials have walls that are only partially crystalline. On the other hand, macroporous structures would pave the way to catalysts with large, periodically ordered, connected, and uniform macropores.

Macroporous solids with pore sizes in the range 100 nm to a few mm are being sought after as absorbents, catalytic supports for degradation of organic molecules and functionalized composites for controlled release systems. These materials are generally prepared by holding together small crystallites with an organic binder ensuring that particles do not pack densely. When this composite is calcined, the organic binder burns away leaving behind connected pores in an inorganic network. Macroporous materials including silica, titania and zirconia have been made by use of crystalline arrays of polystyrene or silica spheres[19-20]. The voids in the colloidal crystals are filled with inorganic materials and finally the colloidal template is removed by dissolution or calcination leaving behind a repeating macroporous structures. The emulsion-assisted approaches have been developed in order to fabricate spherical assemblies of colloidal particles or colloidal clusters using confined geometries of droplets. In a ground breaking work, Velev, Lenhoff, and Kaler (2000) demonstrated that microstructured particles can be synthesized by growing colloidal crystals in aqueous droplets suspended on fluorinated oil[21]. The results from this work opened the way to controllable formation of a wide variety of microstructures. Iskandar, Nandiyanto, Widiyastuti, Young, Okuyama and Gradon (2009) demonstrated that hyaluronic acid (HA) porous particles with controllable porosity and pore size, ranging from 100 to 300 nm, can be prepared

using a colloidal templating and spray-drying method[22]. Such relatively large particles in micron size with low apparent density can be used in dry powder inhalers. Lee, Gradon, Janeczko, Iskandar and Okuyama (2010) demonstrated that ordered macroporous particles can be produced via spray drying process using an aerosol reactor, in which droplets with polymeric beads and inorganic nanoparticles were atomized, dried and annealed inside high-temperature tubular furnace[23]. Cho, Choi, Kim and Yi (2012) demonstrated the bulk synthesis of ordered mesopores silica particles by emulsion templating process[24]. In this process large polystyrene beads and small silica nanoparticles were assembled inside an emulsion, leading to composite structure particles during the evaporation of droplets. The polystyrene beads were burned away by calcination leading to macroporous solid film on the substrate. The macroporous particle film was further coated with fluorinated molecules, thereby imparting super hydrophobic property with multi-scale roughness. The macroporous structures obtained by the above methods have unique optical and thermal properties due to its high degree of order. These three dimensional colloidal crystals resemble naturally occurring opals, and have excellent structure, periodicity, low density, a highly accessible surface, and compositional variety which make them ideal for wide variety of applications such as battery materials, thermal insulators, composite ceramic materials, photonic crystals, cosmetics and catalysis.

1.2 Synthesis of Silica

Different types of silica are available and they can be classified as crystalline or amorphous silica, silica gels or precipitated silica or pyrogenic silica, hydrophobic or hydrophilic silica, porous or non-porous silica. It is important to note that most of the silicas used in countless number of industrial applications are synthetic amorphous silicas (silica gels, pyrogenic or fumed silica, and precipitated silica). Each of these silica have different properties and used for different

12

applications, and the differences in the properties mainly arise from the preparation or synthetic procedures to obtain the silica material. Briefly, the synthetic process can be classified as wet process for silica gels and thermal or pyrogenic process for fumed silica. The most documented method for the preparation of silica gels through wet process is the sol-gel process and the heavily used method for industrial preparation of fumed silica is flame hydrolysis. All the silicas that were used to understand water adsorption behavior in chapter 3 of this dissertation were prepared either by sol-gel process or flame hydrolysis. Hence, in the following section, both continuous flame hydrolysis and sol-gel process will be discussed in detail.

1.2.1 Continuous flame hydrolysis of fumed silica

Fumed silicas are obtained by continuous flame hydrolysis of silicon tetrachloride ($SiCl_4$) i.e burning of $SiCl_4$ in the presence of oxygen and hydrogen under high temperature. $SiCl_4$ is converted to the gas phase (using vaporizer) separately before it is mixed with oxygen and hydrogen and fed into the combustion chamber. A hydrogen flame containing $SiCl_4$ burns continuously inside the reaction chamber. As water gets formed, it reacts spontaneously and quantitatively with $SiCl_4$ inside the flame producing hydrochloric acid and the desired product silicon dioxide (SiO_2). The chemical reactions are listed below and Figure 5 shows the production of fumed silica[5].

$$2H_2 + O_2 \rightarrow 2H_2O$$

$$\underline{SiCl_4 + 2H_2O \rightarrow SiO_2 + 4HCl} \qquad \textbf{(1-3)}$$

$$2H_2 + O_2 + SiCl_4 \rightarrow SiO_2 + 4HCl$$
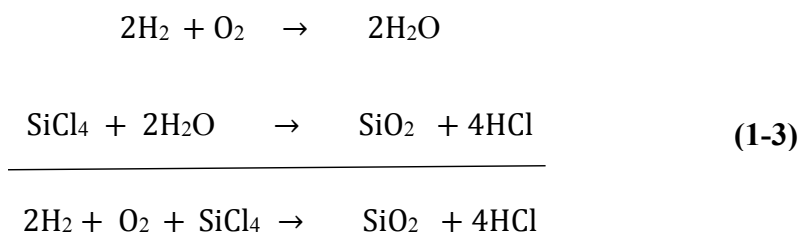
The flame hydrolysis process and eventually the properties of fumed silica can be explained using the droplet model of particle genesis[5] which is schematically illustrated in Figure 6. Some key points of the droplet model[5] is listed below:

1. Reaction gases first pass through the base of the flame and minute droplets (nuclides) of SiO_2 are formed. Droplets collide with one another and merge to form bigger and heavier droplets. This process continues as long as the flame is hot enough to keep the droplets in the liquid state.

2. As these bigger droplets enter the relatively cold region of the flame, they partially solidify. When they collide with each other they do not merge and coalesce completely to form spherical droplets, instead they partially merge to form aggregates.

3. As they go through the colder parts of the flame, the aggregates become fully solidified. When these aggregates collide, they are unable to merge, but instead attach to each other forming agglomerates.

The particle size, particle size distribution, the specific surface and surface properties can be controlled by varying the concentration of the reactants, the flame temperature, and the residence (dwell) time of the silica in the combustion chamber. The specific surface increases as the particle diameter increases and this fundamental correlation is shown in Figure 7. The hydrophilic fumed silica can be further treated with functional silanes to obtain modified silicas (hydrophobic silicas, aminated silicas) for various applications.
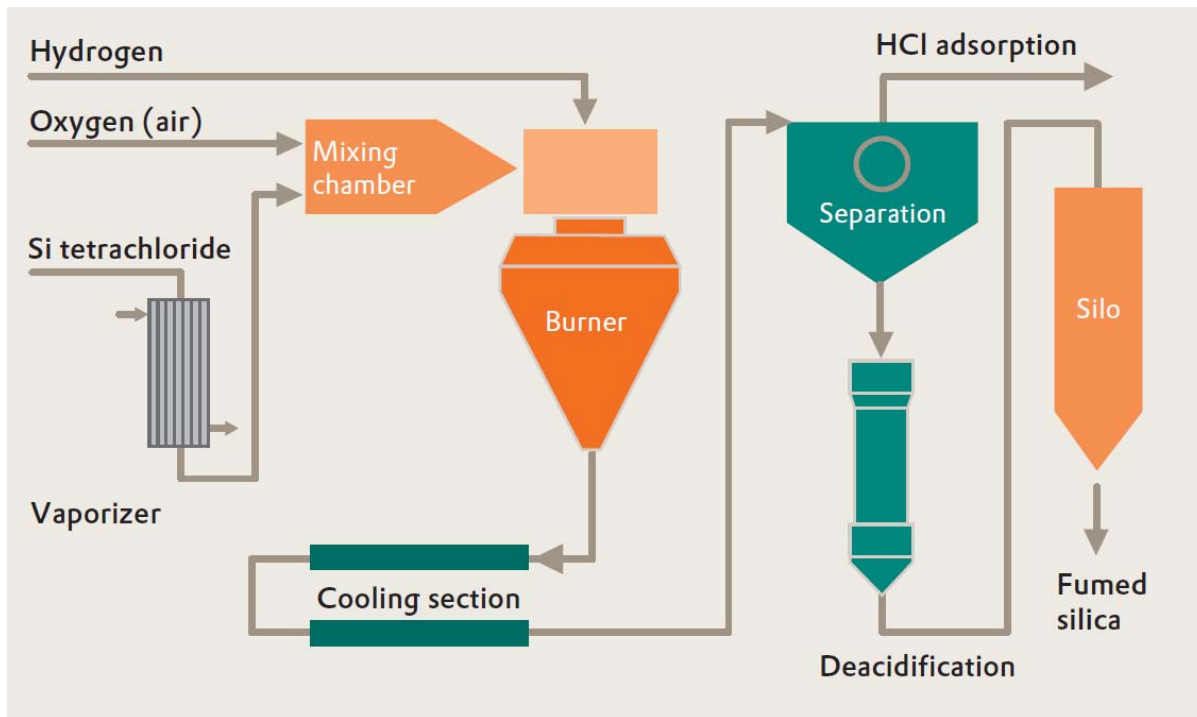
Figure 5. Flowchart depicting the production of Aerosil® fumed silica. Adapted from ref.[5].
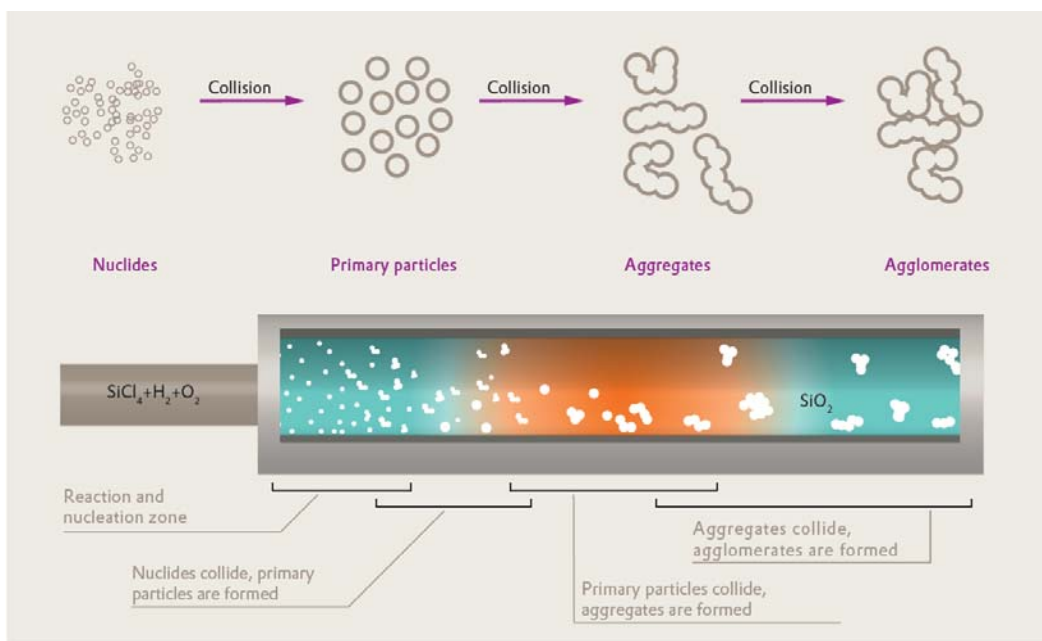
Figure 6. Schematic representation of droplet model of particles genesis in the flame. Adapted from ref. [5].
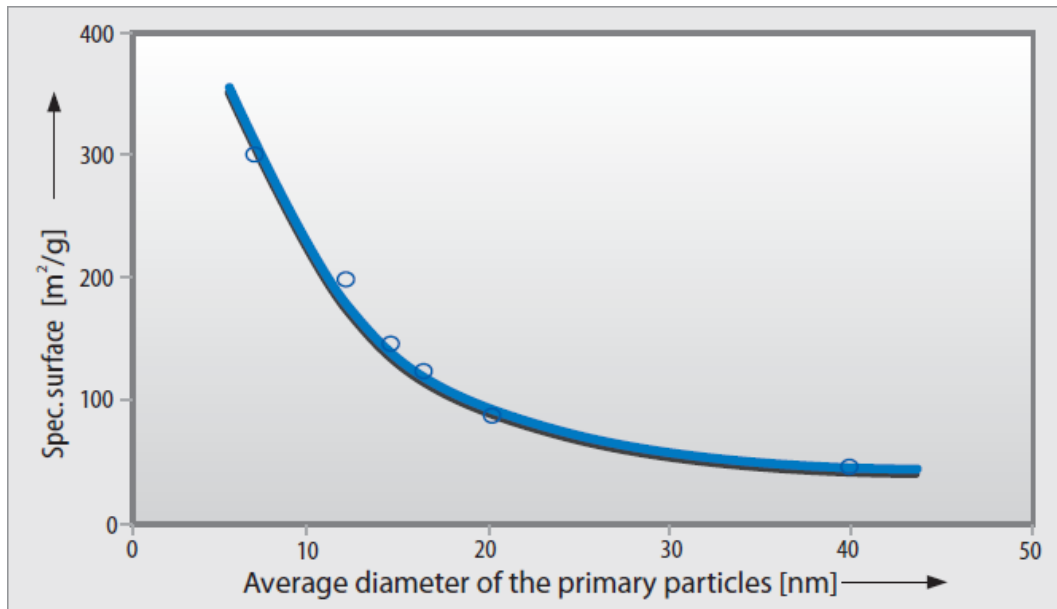
Figure 7. Specific surface area as a function of particle diameter. Adapted from ref. [5].

1.2.2 Sol-gel process of silica gels

A sol is a colloidal dispersion of small solid particles in a liquid, while a gel is a non-fluid three dimensional network that extends through a fluid phase. The origin of sol-gel chemistry can be traced back to an observation made in 1846 where an alkoxide prepared from $SiCl_4$ formed into a gel when exposed to air[25-26]. For almost a century, it remained as an interest only among few chemists and finally in 1930 it was recognized that alkoxides can be used in the preparation of oxide films. In the 1930s various competing theories of gel structures (solid network with continuous porosity, coagulated sol with each particles surrounded by a layer of water, emulsion etc) were proposed[27]. In 1932, the process of supercritical drying to produce aerogels was invented by Kistler[28] and the existence of solid skeleton of the gel was later demonstrated. Later around 1935 to 1950, mineralogists showed interest in the use of sols and gels for preparation of homogenous powders, which was further adopted and popularized by the researchers in the field of ceramics[27, 29]. In the 1970s much more sophisticated technological work was accomplished by

researchers in the nuclear-fuel industry to prepare small spheres of radioactive oxides to be packed into fuel cells for reactors[27]. From the 1970s onward, sol-gel chemistry has been studied and investigated extensively since it has the ability to produce a solid-state material from a chemically homogeneous precursor. Additionally sol-gel chemistry enables greater control over particle morphology and size. The term sol-gel is now used for a diverse range of chemistries involving materials synthesis and as of April 2016, a Scifinder™ search of the word "sol-gel" yielded 134,230 references.

The sol-gel process describes the number of processes through which a sol undergoes a sol-gel transition leading to a rigid porous mass. The required precursors, chemistry, mechanisms involved in the chemistry and the process of making silicate gels are detailed into simple sections as below:

1. Precursors: In the sol-gel process, the term precursor refers to the starting compound that consists of a metal or metalloid elements surrounded by various ligands. The precursors for making metal oxides could be inorganic salts (e.g. $Al(NO_3)_3$ for aluminum oxide) or organic compounds (e.g. $Al(OC_4H_9)_3$ for aluminum oxide). Metal alkoxides belong to the family of metalorganic compounds, which have an organic ligand (an alkoxy group) attached to a metal or metalloid atom. Metal alkoxides are popular precursors owing to their ability to react instantly with water. The suitability of various alkoxides for sol-gel chemistry heavily depends on; a) Ionic character of the M-O bond (arising from electronegativity differences) b) electron donating or withdrawing ability of the alkyl chain on the stability of alkoxy groups[26]. Although sol-gel science involves solution chemistry of inorganic precursors (in aqueous solution) and metal alkoxide precursors (in mixed solvents) of various metals (transition metals such as Ti, V, Zr and Group IIIB metals like B, Al) the main focus of this section will be on silica gels made from silicon alkoxides. One common

example of a sol-gel process related to preparation of silica gel involves the system of tetraethoxyorthosilane (TEOS, $Si(OC_2H_5)_4$), ethanol and water. The one phase solution of the above three component undergoes a sol-gel transition to a rigid two-phase system of solid silica (SiO_2) and solvent-filled pores[30].

2. Hydrolysis and Condensation of Alkoxides: The key step to sol-gel process is the series of hydrolysis and condensation reactions of alkoxides. Hydrolysis and condensation occur almost simultaneously, in the aqueous alkoxide solution. The sol-gel general reaction scheme can be understood by the example of silica gel synthesis using the system of tetraalkoxysilanes ($Si(OR)_4$), ethanol and water. At the functional group level, the following reactions can be used to understand the sol-gel process. The R in the reaction scheme can be CH_3, C_2H_5, n-C_3H_7 or n-C_4H_9 etc.

a) Hydrolysis: The hydrolysis reaction replaces –OR (alkaoxide) groups with –OH (hydroxyl) groups.

$$\equiv Si - OR + H_2O \quad \rightleftharpoons \quad \equiv Si - OH\ +\ ROH$$
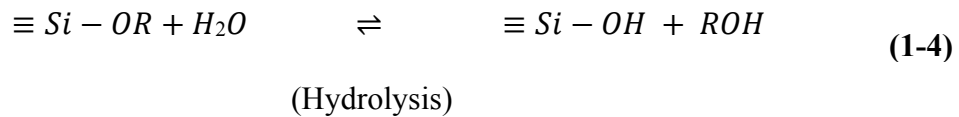
$$\text{(Hydrolysis)} \tag{1-4}$$

b) Condensation: Condensation may occur either between two silanols or a silanol and an ethoxy group to form a siloxane group (Si-O-Si)

$$\equiv Si - OR + HO - Si \equiv \quad \rightleftharpoons \quad \equiv Si - O - Si \equiv\ +\ ROH$$

$$\tag{1-5}$$

$$\text{(Alcohol condensation)}$$

$$\equiv Si - OH + HO - Si \equiv \quad \rightleftharpoons \quad \equiv Si - O - Si \equiv\ +\ H_2O$$

$$\text{(Water condensation)} \tag{1-6}$$
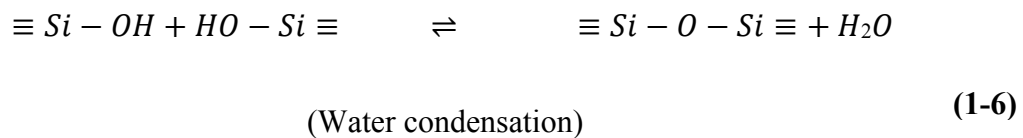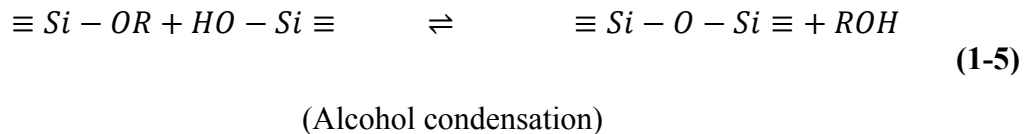
c) Mechanism of acid and base catalyzed hydrolysis: The structure of the resulting gel depends on the rate of hydrolysis and condensation reactions which in turn depends upon the catalyst used[26, 30]. The sol-gel chemistry is driven by acid or base catalyst as neutral reactions are generally slow. The rate of each hydrolysis step depends on the transition state stability which consecutively depends on the electron withdrawing or donation power of the –OH versus –OR groups[26]. In acid catalyzed reactions, the alkoxide group is protonated in a rapid first step and leads to withdrawal of electron density from the Si atom. The Si atom becomes more electrophilic and prone to attack by water. The water molecule attacks the Si, acquires a partial positive charge and weakens the positive charge of the protonated alkoxide, making the alcohol a better leaving group. The transition state decays due to the leaving of the alcohol group and inversion of silicon's tetrahedron geometry. Under acidic conditions, the hydrolysis rate decreases with each subsequent hydrolysis step[3-4, 26-27]. In base catalyzed reactions, water dissociates to produce nucleophilic hydroxyl anions in a raid first step. The hydroxyl anions attacks the silicon atom and displaces the OR with inversion of silicon's tetrahedron geometry. Under basic conditions the hydrolysis rate increases with each subsequent hydrolysis step. In both acid and base catalyzed hydrolysis, it is believed that mechanism is affected by both steric and inductive factors. However, steric factors seems to be more important since Si acquires little charge in the transition state [3-4, 26-27]. Figure 8a illustrates the mechanism of acid and base catalyzed hydrolysis. It is to be noted that the mechanism mentioned here is just one possible pathway for hydrolysis and several other mechanisms are also proposed in the literature[27]. Essentially the process of hydrolysis is affected or governed by the acid or base catalysts, H_2O:Si ratio, solvent, steric and inductive factors on the mechanism of hydrolysis of silicon alkoxides and the reverse reaction esterification.
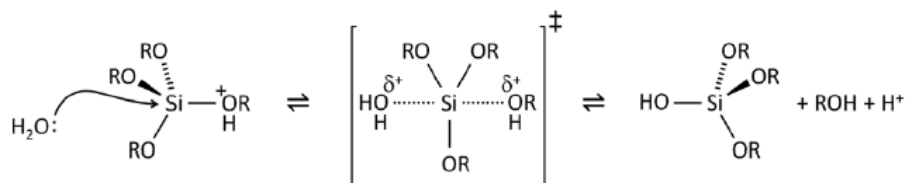
Acid catalysed hydrolysis of silicon alkoxides.
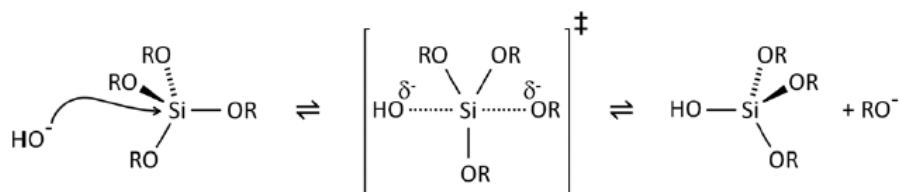
Base catalysed hydrolysis of silicon alkoxides.

Figure 8a. Mechanism of acid and base catalyzed hydrolysis of silicon alkoxides[27].

d) Mechanism of acid and base catalyzed condensation: Since at least one silanol group is a requirement for the condensation reaction to occur, the progress of condensation depends on the degree of hydrolysis. Under acidic conditions, the first hydrolysis step is faster, but the progressive steps of hydrolysis is slower and hence condensation begins even before hydrolysis is completed. Hence, condensation often occurs on terminal silanols leading to chain like structures in the sol which further leads to gel-type networks. In acid catalyzed condensation, the mechanism involves protonation of silanol species and the protonated silanol make the silicon electrophilic and susceptible to nucleophilic attack. Under basic conditions, successive hydrolysis steps are faster and hence hydrolysis is complete before condensation begins. Completion of hydrolysis results in a product $((OH)_3Si\text{-}O\text{-}Si\text{-}(OH)_3)$ that has 6 sites for subsequent condensation. Hence, multiple condensation steps lead to small highly branched agglomerates in the sol which further crosslinks leading to a colloidal gel[26-27, 30]. In base catalyzed condensation, the most widely

accepted mechanism is the attack of the nucleophilic deprotonated silanol on a neutral silicate species. Essentially the process of condensation is affected or governed by catalyst, solvent, steric and inductive factors on the mechanism of condensation of silanols and the reverse reactions (hydrolysis or alcoholysis) [3-4, 26-27]. Figure 8b illustrates the mechanism of acid and base catalyzed condensation.
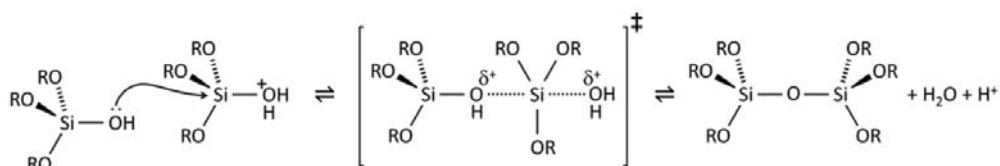
Acid catalysed condensation of silicon alkoxides.
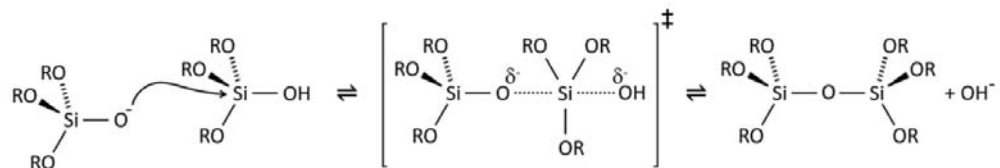
Base catalysed condensation of silicon alkoxides.

Figure 8b. Mechanism of acid and base catalyzed condensation of silicon alkoxides[27].

3. Gelation: The relative rates of hydrolysis and condensation determine the structure of the gel and it is established at the time of this gelation step. Gel formation (gelation) occurs when the sol particles undergo adequate condensation reactions leading to formation of a network (gel). At gelation, the viscosity increases sharply leading to a solid object taking the shape of its container[30-31].

4. Aging: During the aging process, four processes namely polycondensation, syneresis, and coarsening can occur. Polycondensation reactions continue to occur within the gel network as long as neighboring silanols are close to each other. Syneresis is the shrinkage of gel network leading

to expulsion of solvent from the pores. The rate of syneresis depends on the composition of the liquid inside the pores[27, 31]. The process of shrinking will continue as long as there is flexibility in the gel. Coarsening is the irreversible decrease in surface area through dissolution and re-precipitation process.

5. Drying: At first the gel shrinks by the amount equal to the volume of liquid that evaporates from the structure and the liquid-vapor interface remains at the exterior surface of the body. Secondly, the gel becomes rigid to shrink and the liquid recedes into the interior resulting in air-filled pores near the surface and evaporation rate drops. Eventually, the liquid becomes isolated into pockets and drying proceeds by evaporation of liquid within the gel and diffusion of the vapor to the outside[27, 31].

1.2.3 Templated sol-gel process of ordered mesoporous silica

Zeolites or microporous materials were not able to meet the demands of growing applications such as adsorption, separation, catalysis, drug delivery photonics, energy storage & conversion and chemical sensors. However, mesoporous materials with structural capabilities at the scale of few nanometers and high surface areas shows great potential for the above mentioned applications. However the mesoporous materials developed since the 1980s were amorphous with disordered pore systems and broad pore size distributions[9, 13, 32-33]. The necessity to obtain mesoporous materials with controllable structures (uniformity within the pore size, shape and volume) and tunable pore architecture led to the fast expansion of mesoporous materials leveraging the technical advances in the fields of chemistry, material science and engineering. Besides, the design and synthesis of novel mesoporous materials with ordered and well-defined pore structure are important for academic research work. Regardless of the synthetic process to obtain ordered mesoporous materials, the common element is the use of a 'template' to obtain mesoporous

materials with controllable structures[32, 34]. Table 3 list some of the important milestones in the development of ordered mesoporous materials using template synthesis.

Table 3. Key milestones in the evolution of ordered mesoporous materials via templating method.

Year	Milestones
1969	Vincent and his co-workers (1971) had prepared MCM-41 analogues in the presence of a cationic surface active agent but they claimed low-bulk density silica due to the lack of detailed characterizations[35].
1990	Japanese scientists reported the synthesis of alkyltrimethylammonium-kanemtie complexes with a mixed phase[36]. Nitrogen sorption isotherms showed narrow pore size distribution at 2-4 nm, but authors did not characterize the material as mesopores.
1992	Mobil scientists reported the synthesis of ordered mesoporous molecular sieves (M41S) from liquid crystal templates[10-11]. This is the first time the term "mesoporous molecular sieves" showed up in a publication.
1993	Inagaki, Fukushima and Kuroda optimized the synthesis conditions and obtained a pure ordered mesoporous silicate[37].
1994	Using a self-assembled surfactant molecular array, a series of M41S materials namely MCM-41 (hexagonal), MCM-50(lamellar) and MCM-58 (cubic) were synthesized[13].
1998	Zhao, Huo, Feng, Chmelka and Stucky (1998) reported the preparation of large pore ordered mesoporous silica (SBA-15 silica) with a 2D hexagonal structure by using triblock copolymers as templates[14].

The template synthesis involves building a material around some molecule, macromolecules or liquid crystal. One of the commonly employed templating methods for mesoporous materials is soft templating method. Soft templating method involves two synthetic strategies namely a) cooperative self-assembly and b) true liquid crystal templating processes.

As illustrated in Figure 8b, the cooperative self-assembly strategy[38] involves the following steps: i) driven by coulomb forces, covalent bonding or hydrogen bonding, inorganic species interact with surfactants, polymerize at the interface, crosslink and cooperatively assemble with the surfactants. ii) As the reaction proceeds, cooperative arrangements between surfactants and the charge density between inorganic and organic species influence each other leading to varied compositions of inorganic-organic hybrids. iii) The cooperative assembly process is governed by the balance of charge density at the surfactant/inorganic interfaces, resulting in phase separation and reorganization and finally leading to formation of ordered 3-D arrangement with the lowest energy[10, 12, 32, 38].

The term liquid crystal is used to describe the fourth state of matter, which exists between the liquid and solid phases. Liquid crystals possess both long-range orientation order of solids and the fluidity and viscosity of liquids. As illustrated in Figure 9, the true liquid crystal templating process[38] involves the following steps: i) formation of semi liquid crystal mesophase micelles from high concentration surfactants that act as templates. ii) Condensation of inorganic precursors and confined growth around surfactants leading to ceramic-like frameworks and iii) removal of organic templates leading to mesoporous frameworks[10, 12, 32, 38].

Considering the very fast proliferation of synthetic strategies to obtain ordered mesoporous materials, it is important to understand the influence of the choice of method and surfactants on the final mesostructures (pore structure, symmetry, connectivity) and pore sizes of mesoporous

materials. The final mesostructure is influenced by surfactant concentration, temperature and hydrophilic/hydrophobic volume ratio of the template molecule. The pore sizes of the mesoporous materials mainly depend on the hydrophobic groups in surfactants. Table 4 illustrates the pore sizes of ordered mesostructure[38] obtained by various methods.
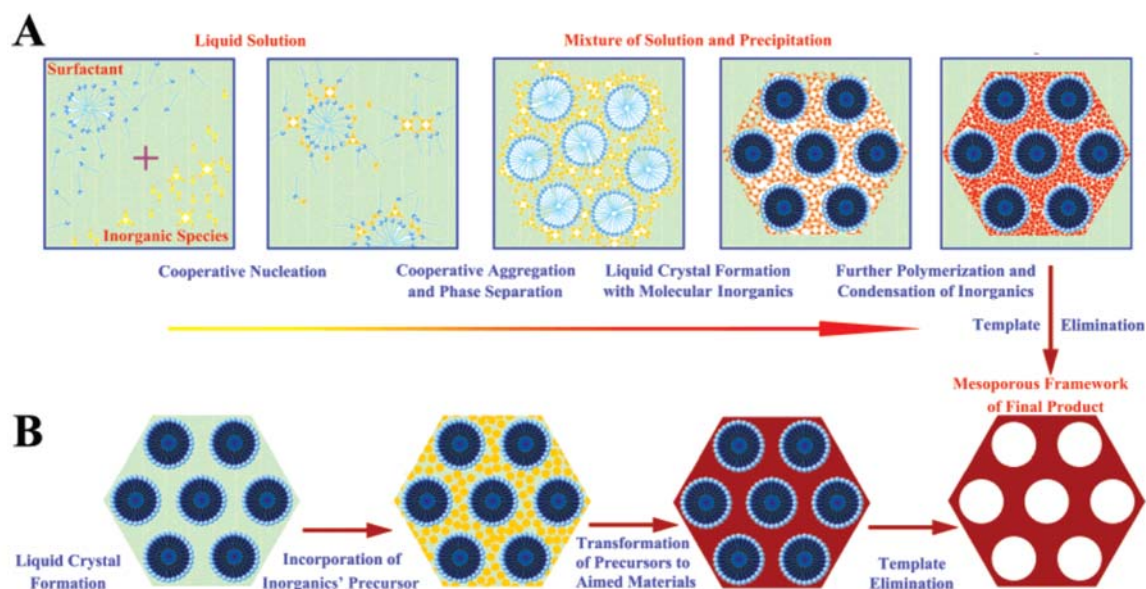
Figure 9. Two synthetic strategies of soft templating synthesis of mesoporous materials: (A) cooperative self- assembly; (B) true liquid-crystal templating process. Adapted from ref.[38].

Table 4. Pore sizes of ordered mesostructures obtained by various method.[38].

pore size (nm)	method
2-5	surfactants with different chain lengths including long-chain quaternary cationic salts and neutral organoamines
4-7	long-chain quaternary cationic salts as surfactants high-temperature hydrothermal treatment
5-8	charged surfactants with the addition of organic swelling agents such as TMB and midchain amines
2-8	nonionic surfactants
4-20	triblock copolymer surfactants
4-11	secondary synthesis, for example, water-amine post synthesis
10-27	high molecular weight block copolymers, such as PI-*b*-PEO, PIB-*b*-PEO and PS-*b*-PEO triblock copolymers with the addition of swelling agents TMB and inorganic salts low-temperature synthesis.

1.3. Characterization of the Silica Surface

Many of the adsorption, chemical and catalytic properties of a silica material depends on the surface chemistry and pore geometry of the silica surfaces. Hence, a comprehensive characterization study of the silica surface includes surface area (m^2/g), pore volume (porosity), pore size distribution (based on pore volume and pore area) and surface silanols is required to properly define the complex material of interest and to optimize the performance of these silica materials for many industrial applications[33, 39]. In this study gas adsorption is used as an experimental method for surface area, pore volume, pore diameter & pore size characterization of silica materials and thermogravimetric analysis for obtaining the number of surface silanols. A brief introduction of the two techniques, namely gas adsorption, and thermogravimetric analysis is provided. A more detailed description with calculation procedures is presented in Chapter 2.

1.3.1 Surface area, pore volume, pore diameter and pore size distribution

Gas adsorption is a widely used technique for surface area, pore volume, pore diameter and pore size distribution since it allows assessment of a wide range of pore sizes (0.4 nm to 100 nm) namely, micropores and mesopores. Surface area and pore volume play complementary roles in adsorption phenomena and hence measurements of adsorption of gases on a solid surface can be used to understand the surface area and pore structure of that solid material. Adsorption simply denotes to the condensation of gases on free surfaces. This includes, the accumulation of molecular species at the surface rather than in the bulk of a solid or liquid is termed adsorption. The gas is referred to as the adsorbate and the solid (surface) is referred to as adsorbent.

Adsorption arises due to surface particles of the adsorbent not in the same environment as the particles inside the bulk. The unbalanced or residual attractive forces on the surface of the adsorbent are responsible for attracting the adsorbate particles to its surface. The extent of

adsorption increases with the increase of surface area per unit mass of the adsorbent at a given temperature and pressure. During adsorption, there is always a decrease in residual forces of the surface, i.e there is a decrease in surface energy which appears a heat. Hence, adsorption is always an exothermic process (ΔH is negative). When a gas is adsorbed, the freedom of movement of its molecules is reduced, i.e there is decrease in entropy (ΔS is negative). Hence, adsorption is accompanied by decreases in enthalpy and entropy of the system. For any process to be spontaneous, the thermodynamic requirement is that Gibbs energy ΔG (= ΔH-TΔS) should be negative. In the adsorption process, ΔG can be negative only if ΔH has high negative value since -TΔS is positive due to negative entropy. In spontaneous adsorption, ΔH is highly negative to begin with and as the adsorption proceeds ΔH becomes less and less negative until ΔH becomes equal to TΔS and ΔG becomes zero (equilibrium state is attained).

The adsorption is brought about by the forces acting between solid and gas molecules and the acting forces can be of two types, namely physical (van der Waals) and chemical, leading to physisorption and chemisorption respectively. Chemisorption occurs through chemical bonding, site specific, mostly irreversible and accompanied with heats of adsorption. On the other hand, physisorption occurs through van der Waals forces, not site specific, reversible and accompanied with low heats of adsorption. It is to be noted that these two processes (physisorption and chemisorption) can also occur simultaneously and it is not easy to ascertain the type of adsorption. However, gas adsorption must be a physisorption process to ensure accurate measurements. Physisorption is most suitable for surface area determinations and the forces involved in physisorption van der Waals forces including the long range London dispersion forces and short range intermolecular repulsion. It is important to note that physisorption is fully reversible, enabling both the adsorption and desorption process to be studied[8, 40].

In gas adsorption, the amount of gas adsorbed on a given surface (adsorbent) is measured as a function of the equilibrium partial pressure at constant temperature. The quantity of gas adsorbed on an adsorbent maintained at a fixed temperature (T) is expressed as:

$$n = f(p/p^o)_{T,gas,solid} \qquad \textbf{(1-7)}$$

where, n is the quantity of gas adsorbed in moles per gram of adsorbent, p is vapor pressure and p^o is the saturation vapor pressure of the adsorptive[8]. An adsorption isotherm is a curve obtained by plotting adsorbed amount (n) as a function of relative pressure (p/p^o) at constant temperature. The majority of the isotherms resulting from physisorption will fall under one of the six isotherms as shown in Figure 10. The isotherms I to V was originally proposed by Brunauer, Deming, Deming and Teller (BDDT) and also referred to as the Brunauer, Emmett and Teller (BET) or simply Brunauer classification. Type 1 isotherms are obtained when adsorption is limited to a few molecular layers and seen in physical adsorption on microporous materials or observed in chemisorption. Type II isotherms are observed in non-porous or macroporous materials demonstrating unrestricted monolayer-multilayer adsorption. Type III isotherm is not common and it represents a very weak adsorbate-adsorbent interaction (e.g. nitrogen on polyethylene or water vapor on graphite). Type IV and V isotherms are characteristic of mesoporous materials and possess a hysteresis loop, the lower branch and upper branch obtained by adsorption (progressive addition of gas) and desorption (progressive withdrawal of gas) respectively. The hysteresis loop is associated with pore condensation and the plateau in isotherm at high p/p^o indicates pore filling. The initial part of type IV depicts monolayer-multilayer adsorption as seen in type II and the initial part of type V indicates weak adsorbate-adsorbent interaction as seen in type III. The stepped isotherm as seen in type VI is of rare occurrence and is seen with argon or krypton adsorption on graphitized carbons at liquid nitrogen temperature[4, 8, 39-40].
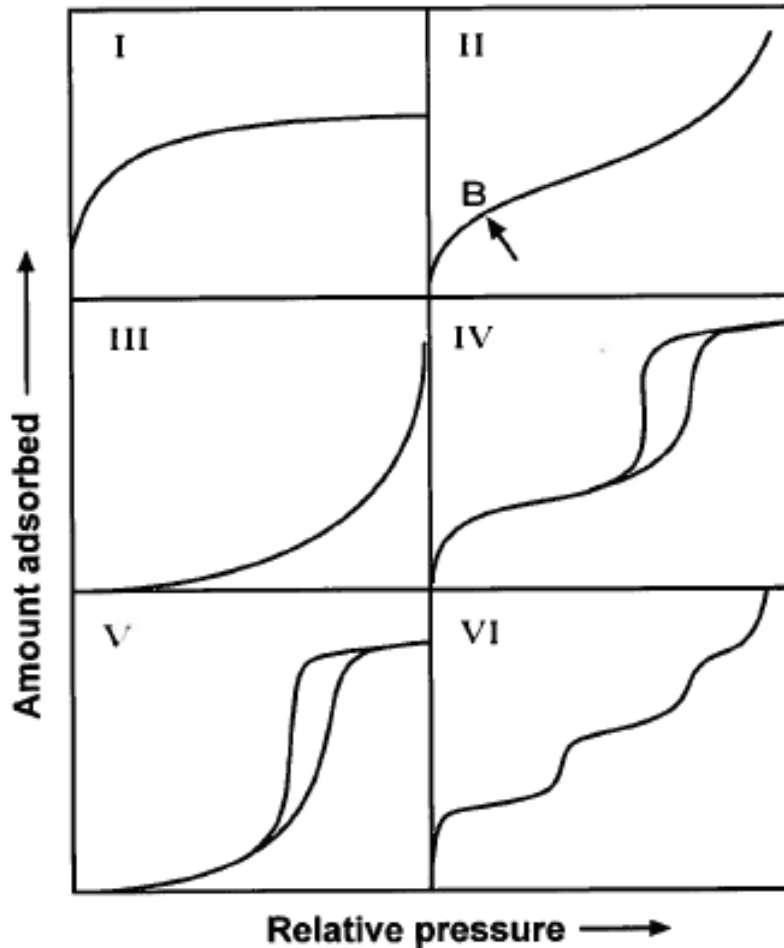
Figure 10. IUPAC classification of sorption isotherms. Adapted from ref.[40].

Gravimetric and volumetric methods are the two most commonly employed techniques for making adsorption measurements. Gravimetric method is preferred for the study of vapor adsorption at temperatures close to room temperature while volumetric method is the method of choice for study of vapor adsorption at cryogenic temperatures. Nitrogen at 77K is the gold standard for surface area and pore size analysis, however alternative probe molecules such as krypton, argon, carbon dioxide are being used in several studies such as krytpon for low surface area analysis, argon for assessing microporous systems (zeolites) and carbon dioxide for ultramicropores in carbonaceous materials[8, 39-40].

While several probe molecules (adsorbates) are being studied and used currently for characterization of various surfaces, it is important to note that a classification of adsorbents and adsorbates based on their capacity for non-specific and specific molecular interaction has been discussed by Kiselev[41] as early as 1965. The non-specific interactions (predominantly dispersion interactions) are universal and exists almost in all cases, while the specific interactions exist wherever there is concentration of negative or positive charges leading to Coulomb interactions. As listed in Table 5, Kiselev schematically classified adsorbates and adsorbents based on their abilities for specific and non-specific interactions.

Table 5. Classification of adsorbates and adsorbents based on their capacity for no-specific and specific interactions[41].

groups of adsorbate molecules	types of adsorbents		
	I. Carrying neither ions, nor active groups (graphitized carbon blacks, BN, surfaces carrying only saturated groups)	II. Carrying concentrated positive charges (acid hydroxyls. exchange cations of small radius)	III. Carrying concentrated negative charges (ether, nitrile, carbonyl groups, exchange anions of small radius)
(a) With spherical symmetrical shells or σ-bonds (noble gases, saturated hydrocarbons)	non-specific interactions depending mainly on dispersion forces		
(b) With electron density locally concentrated on the peripheries of bonds and links: π-bonds (N_2, unsaturated and aromatic hydrocarbons), and lone electron pairs (ethers, ketones, tertiary amines, nitriles, pyridine)	non-specific interactions	non-specific + specific interactions	
(c) With positive charges locally concentrated on the peripheries of links (e.g., certain organometallic compounds)	non-specific interactions	non-specific + specific interactions	
(d) With functional groups with both electron density and a positive charge concentrated on the peripheries of their individual links (molecules with OH or NH groups)	non-specific interactions	non-specific + specific interactions	

This research will study the adsorption of nitrogen and water on well-defined dehydroxylated, partially hydroxylated, and fully hydroxylated silica surfaces. As per the classification in Table 5, the adsorbates nitrogen and water would fall under the molecules of type b and d respectively. The dehydroxylated silica would be a non-specific adsorbent (type I), the partially hydroxylated silica could be a mix of type I & II and the fully hydroxylated silicas would come under type II adsorbents.

Surface area is an important parameter for optimizing the use of porous materials in many applications. Nitrogen is the preferred standard adsorptive for determining surface area through adsorption. A number of theories have been outlined periodically to interpret the isotherm in quantitative terms, none with complete success. Out of all, the most useful and highly used model for surface area determination is the Brunauer, Emmett and Teller (BET) theory or model. Details of the BET model or equation and calculation of surface area from adsorption isotherms using BET equation is discussed in chapter 2 of this work.

The study of pore structure of any porous solid involves the interpretation of the adsorption and desorption branches of the full isotherm (Type IV for mesoporous). A characteristic feature of type IV isotherm is the hysteresis loop and it is attributed to the concept or phenomenon of capillary condensation that happens within the pores during adsorption process. The theory of capillary condensation and its quantitative expression Kelvin equation for calculation of pore size distribution is discussed in Chapter 2 of this thesis.

Nitrogen adsorption–desorption isotherms (77 K) were measured using an Autosorb-1 and Autosorb IQ analyzer (Quantachrome Instruments, Boynton Beach, FL, USA). The surface area (using a_{N2} = 16.2 Å2) was calculated via the Brunauer–Emmett–Teller (BET) method in the range of relative pressure from 0.05 to 0.25. The cumulative volume of the pores was determined from

adsorption at 0.98 p/p^0. The pore size distribution and average pore diameter was calculated with the Barrett–Joyner–Halenda (BJH) algorithm using the adsorption branch of the adsorption–desorption hysteresis. Water adsorption-desorption isotherms (293K) were measured using an Autosorb-1 analyzer (Quantachrome Instruments, Boynton Beach, FL, USA) and IGASORP , dynamic vapor sorption analyzer (Hiden Isochema, Warrington, UK).

1.3.2 Surface silanols

The existence of silanol groups (hydroxyls) was postulated as early as 1934 and various analytical techniques have been used to confirm and expand the view of silica surface group in terms of silanol groups, siloxane bridges and hydrogen-bonded water[1]. The silanol groups are formed on the surface of silica by two main processes: a) during the condensation-polymerization of $Si(OH)_4$ in the course of synthesis of silica and b) rehydroxylation of dehydroxylated silica when exposed to water or aqueous solutions. Silanols are found not only on the surface of silica but also within the structure of silica particles, referred to as internal silanols. Silanols on the surface of silica can be classified according to their nature, multiplicity of sites and type of association and this classification is discussed in detail in Chapter 2. The silanols on the surface of silica are the main centers of adsorption of water molecules. The surface silanols can be increased or decreased by the procedures of hydroxylation (exposure to water) and dehydroxylation (thermal treatment) respectively. The concentration of hydroxyl groups, the procedures of hydroxylation & dehydroxylation and the nature of structurally bound water has been well studied [1, 3, 6, 8, 41-42] . The concentration of silanols on the surface of silica is expressed in number of OH groups per square nanometers. It is denoted as α_{OH} and is often called as the silanol number. Zhuravlev[42] obtained a value of α_{OH} = 4.6 OH groups per square nanometer and it is very close the number obtained various researchers.

Hockey and Pethica (1961) studied the dehydration and hydration of silica powders by infrared, water adsorption and gravimetric methods[43]. Smith and Kellum (1966) determined the OH surface density of silica samples using both thermo gravimetric analysis (TGA) and a modified Karl Fischer reagent[44]. The Karl Fischer titration technique provided the physically adsorbed water content while TGA gave the total weight loss from physically adsorbed and chemically bound water. Mueller, Kammler, Wegner and Pratsinis (2003) and Wisser et al (2012) studied the surface hydroxyl content of silica and other oxides using thermo gravimetric analysis and lithium alanate method[45-46]. In this work, we will be using the thermo gravimetric analysis to determine the surface hydroxyl content of silica. Thermal analyses of the adsorbents were performed using a Q500 Thermogravimetric Analyzer (TA Instruments, USA). Samples were analyzed using a temperature program from 25°C to 1000°C at a heating rate of 10°C/min. The -OH groups were calculated based the formula:

$$\text{No of} - \text{OH groups} = \frac{(\% \, Weight \, loss \, \times 667)}{S_{N_2}} \qquad \textbf{(1-8)}$$

where % Weight loss is the weight loss from TGA for the temperature range 200°C to 1000°C and S_{N_2} is the BET surface area obtained from nitrogen sorption measurements.

Chapter 2: Surface Hydration and Physical Characterization of Silica

2.1 Introduction

Silica continues to receive great attention in surface and material sciences with prominent applications in catalysis, nanocomposites, separations, drug delivery etc. All the above mentioned applications of silica are decisively influenced by the properties of the silica surface. Silica surfaces are often covered with hydroxyl groups and even physically adsorbed water, under ambient conditions. The presence of hydroxyl groups and physically adsorbed water influences the reactivity and performance of silica and hence understanding the silica-water system is of utmost importance[6, 42-43, 47-48]. The formation of hydroxyl groups on silica surface, type of hydroxyls present on the silica surface and the process of surface hydroxylation and dehydroxylation reactions will be discussed. In addition, the characterization of hydroxyl groups by thermo gravimetric method and adsorption measurements will be discussed. These studies will eventually lead to the experimental work described in Chapter 3, in which water adsorption on a wide variety of silica surfaces will be presented with results and conclusions.

2.2 Surface Hydration

2.2.1 Formation of surface hydroxyls (silanols)

Silanol groups are formed on the surface of silica by two main processes namely: a)during silica synthesis the supersaturated solution of the silicic acid gets converted to polymeric form, which eventually changes to spherical colloidal particles with $\equiv$Si-OH groups on the surface upon drying. b) Surface silanols are also formed when fully or partially dehydroxylated silica surface (with siloxanes) is hydroxylated upon treatment with water or aqueous solutions. Figure 11 illustrates the formation of silanol groups on the surface[6, 42].
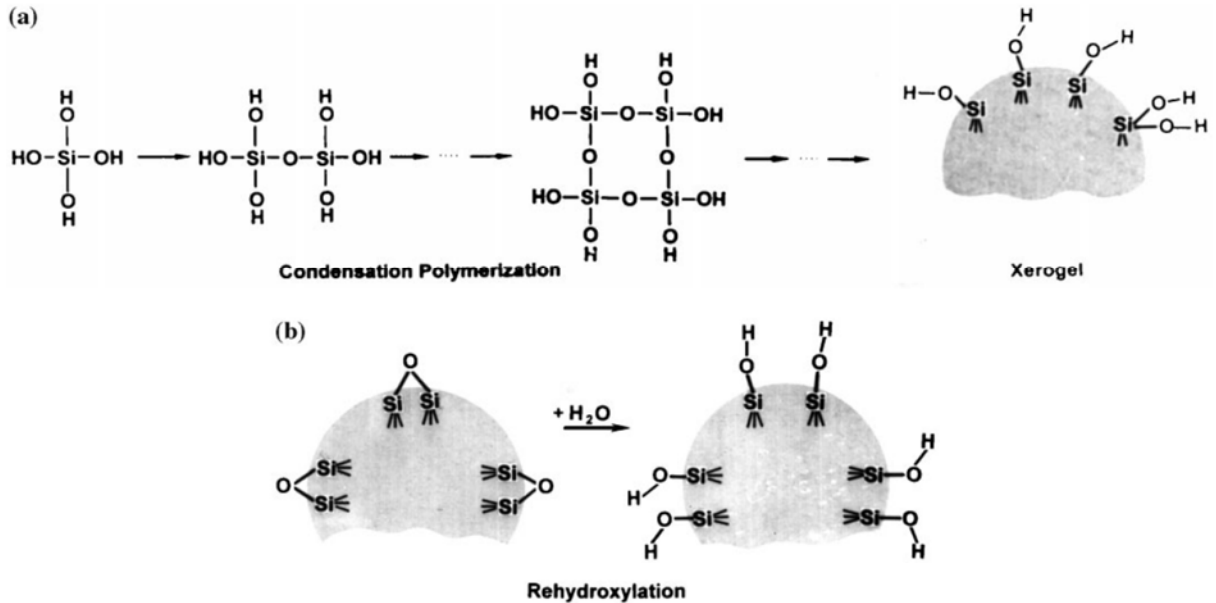
Figure 11. The formation of silanol groups on the silica surface: (a) Condensation polymerization; (b) rehydroxylation. Adapted from ref.[6].

2.2.2 Type of surface hydroxyls (silanols)

The silanol groups on the surface of silica are classified according to their nature, multiplicity of sites and type of association. Surface silanols are categorized as below:

(i) isolated free (single silanols), ≡Si-OH: these include an OH groups located at a distance sufficiently far from neighboring hydroxyl groups and hence hydrogen bonding is prevented. The isolated silanol exhibits a sharp band at around 3750 cm^{-1} in the infrared spectrum.

(ii) geminal free (geminal silanols or silanediols), =Si-(OH)$_2$: these include silanediols i.e two hydroxyl groups attached to the same silicon atom.

(iii) vicinal, or bridged, or OH groups bound through the hydrogen bond (H-bonded single silanols, H-bonded geminals, and their H-bonded combinations): these are Si-OH groups in which the OH

to O distance is sufficiently small that hydrogen bonding occurs. The vicinal OHs exhibit a characteristic band at around 3660 cm^{-1} in the infrared spectrum.

Silanol groups are found not only on the surface but also within the structure of silica colloidal particles and are called internal silanols. These internal silanols are sometimes classified as structurally bound water whose concentration levels depend upon the synthesis, temperature and other variables. Additionally, surface and internal silanols will condense to form siloxane groups ($\equiv$Si-O-Si$\equiv$) with oxygen atoms on the surface accompanied by loss of water. Figure 12 illustrates the type of silanol groups and siloxane bridges on the surface of silica.
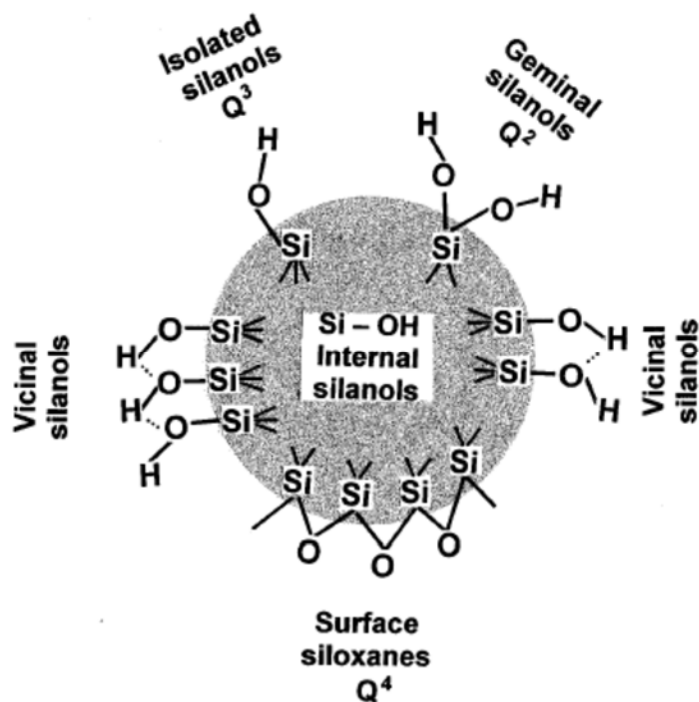
Figure 12. Type of silanols and siloxane bridges on the surface of amorphous silica. Q^n terminology is used in NMR; n indicates the number of bridging oxygens (-O-Si) bonded to the central, silicon (n = 0-4) Adapted from ref.[6].

The silica surface silanols are the main centers of adsorption of water molecules. Water can be associated through hydrogen bonding to any type of surface silanols and this water adsorbed on the surface is referred to as physically adsorbed water. By performing molecular dynamics calculations Grivtsov, Zhuravlev, Gerasimova and Khazin(1988)[49] showed that mutual orientation of water molecules and hydroxyl groups prevents the adsorption of two water molecules simultaneously and hence one molecule of water is adsorbed per silanol group on average. The water can be adsorbed to the surface silanols via two different pathways as shown in Figure 13. In the first pathway (most probable), the hydrogen atom in the water molecule is bonded to the oxygen atom of the $\equiv$Si-OH group. In the second pathway, the oxygen atom in the water molecule is bonded to the hydrogen atom of the $\equiv$Si-OH group[49].
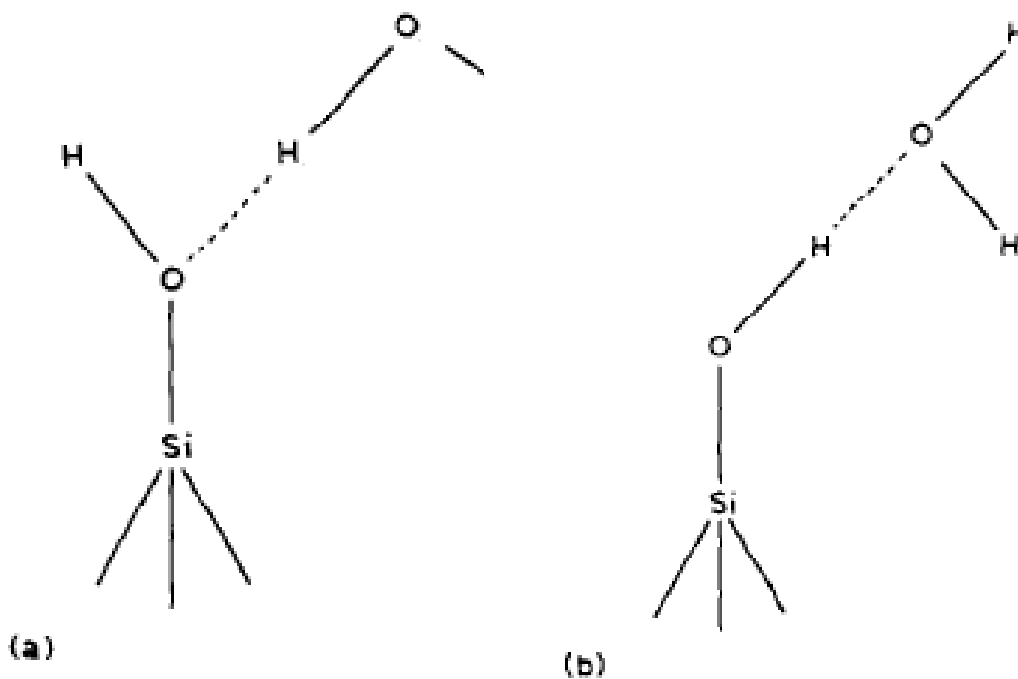
Figure 13. Two types of physically adsorbed water (a) the hydrogen atom in the water molecule is bonded to the oxygen atom of the $\equiv$Si-OH group (b) the oxygen atom in the water molecule is bonded to the hydrogen atom of the $\equiv$Si-OH group[42, 49].

2.2.3 Dehydration, dehydroxylation and rehydroxylation of silica

The amount of water (physically adsorbed), concentration of surface silanol groups and siloxanes are all dependent on various factors including but not limited to silica synthesis conditions, storage conditions (extent of exposure to environment) and specific pretreatment (thermal heating or hydroxylation) of the silica.. At sufficient concentrations of hydroxyl groups, the silica surface is hydrophilic and the removal of hydroxyl groups makes the surface hydrophobic. The scale of hydrophilic or hydrophobicity of surface, chemical reactivity of the silica surface are all very crucial in deciding the final application of the silica material. Since surface hydroxyl groups play an active role in determining the applications of silica material, it is necessary to obtain both qualitative and quantitative information on the surface concentration of silanol groups. To obtain this information, several silica samples with varying amounts of surface silanols are required and to obtain such samples, understanding of dehydration, dehyroxylation and rehydroxylation procedures are very important. It is to be noted that much of the nature of hydroxyl groups on silica surfaces were obtained earlier by the Infra-Red (IR) spectroscopic investigations[48] and later by thermal gravimetric and titration methods.

2.2.3.1 Dehydration of silica surface

It is important that a distinction is made between surface silanols and physically adsorbed water and the process of removal of physically adsorbed water from the surface of silica is referred to as dehydration of silica surface. In the absence of micropores, most of the physically adsorbed water can be removed by heating up to 120°C but all the surface hydroxyls will be retained according to Boer and Vleeskens. Lange[50] suggested that strongly adsorbed water, especially retained in micropores can be removed only at 180°C. By combined use of thermogravimetric

measurements, deuterium exchange and mass spectral analysis, it has been established that the physically adsorbed water can be removed from the surface of silica by heating the silica sample from room temperature to 200°C under vacuum[42]. The physically adsorbed water (weakly held) can be removed by solvent extraction and determined by Karl Fischer titration. Smith and Kellum (1966) determined the OH surface density of silica samples using both thermogravimetric analysis (TGA) and a modified Karl Fischer reagent[44]. The Karl Fischer titration technique provided the physically adsorbed water content (the Karl Fisher reagent reacts only with adsorbed water and not with the silanol groups), while TGA gave the total weight loss from physically adsorbed and chemically bound water. Mueller et al and Wisser et al studied the surface hydroxyl content of silica and other oxides using thermo gravimetric analysis and lithium alanate method[45-46]. However, the most common prevailing view is that physically adsorbed water is completely removed by heating the silica sample from room temperature to 200°C under vacuum[6, 42]. Figure 14 shows a typical thermogram of hydroxylated silica with physically adsorbed water on the surface.
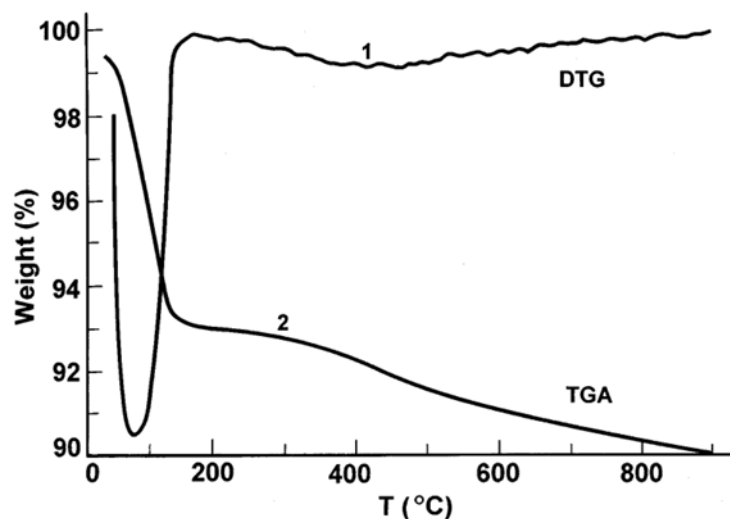
Figure 14. Thermogravimetric analysis of a hydroxylated silica with physically adsorbed water on the surface (mesoporous silica gel) (1) DTG curve, (2) TGA curve) Adapted from ref.[4, 6].

The profiles of curve 1 (differential thermogravimetric analysis curve (DTG)) and curve 2 (TGA curve) indicate the loss of physically adsorbed water and is completed around ~150 - 200°C. It is important to keep in mind that storage conditions contribute the maximum to the physically adsorbed water. Chemical modification of the surface of silica continue to receive great interest and hence the physically adsorbed water should be removed in order to obtain reaction with the surface silanol groups for any type of silica surface modification.

2.2.3.2 Dehydroxylation of silica surface

The dehyroxylation of a silica surface refers to the removal of silanol groups by thermal pretreatment *in vacuo* (i.e treating silica at various temperatures). Pretreatment of silica at temperatures ranging from 200°C to 1100°C leads to various extent of dehydroxylation and the dehyroxylation is quantified by measuring the number of silanol groups per unit area (silanol number, α_{OH}) after thermal pretreatment up to a particular temperature. Figure 15 shows silanol number as a function of pretreatment temperature for different samples of silica with knows surface area. The total silanol number($\alpha_{OH,\,T}$) decrease considerably in the pretreatment temperature range of 200 to 400°C and the decrease in α_{OH} becomes notably smaller in the pretreatment temperature range of 400 to 1100°C. Table 6 lists the different types of silanols that are present after thermal pretreatment at a particular temperature. It is to be noted that the initial state (temperature treatment of 180-200°C, i.e after removing only physically adsorbed water) corresponds to the maximum degree of surface hydroxylation (first row in Table 6). During the transition (thermal treatment) range of 200 to 400°C, all different types of silanol groups (isolated, geminals, vicinals) are present. At 400°C, all vicinal groups are gone and only isolated and vicinal groups remain on the surface. During the transition from 400 to 900°C, isolated silanols and geminals continue to

remain, but their concentration continues to decrease. At 900°C, there is complete removal of geminals and isolated silanols remain on the surface. During the transition from 900 to 1200°C, concentration of isolated silanols continue to decrease. At 1200°C, there are no silanols present on the surface and the surface is covered with SiOSi groups.
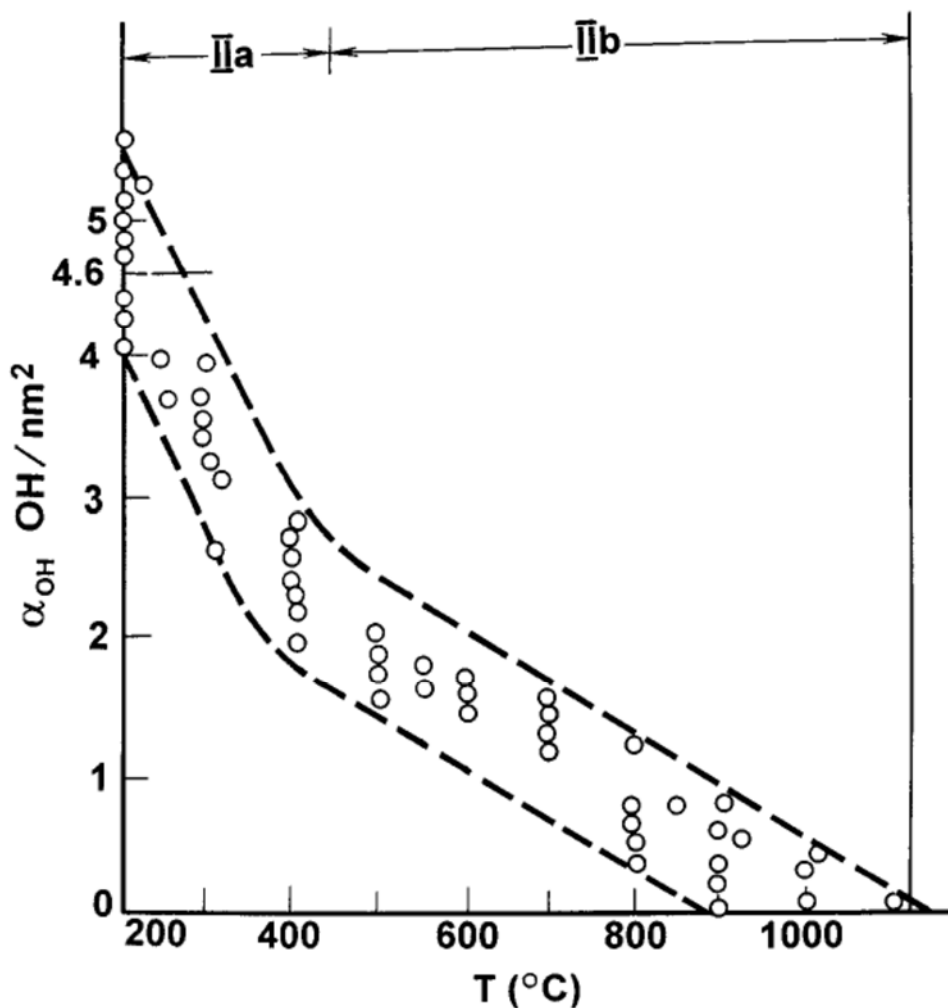
Figure 15. Silanol as a function of the temperature of pretreatment in vacuo for different samples of silica. The broken lines delimit the range of experimental data (16 samples with different surface area from 11 to 905 m²/g). The sub regions of dehydroxylation are: IIa from 200 to ~400°C, and IIb from 400 to 1100°C. Adapted from ref.[6].

Table 6. Surface concentration of the different types of OH groups as a function of pretreatment temperature in vacuo, with the initial state corresponding to the maximum degree of surface hydroxylation (first row)[6].

Temperature of vacuum pretreatment, T (°C)	Total OH groups, $\alpha_{OH,\,T}$ (OH nm^{-2})	Isolated OH groups, $\alpha_{OH,\,I}$ (OH nm^{-2})	Geminal OH groups, $\alpha_{OH,\,G}{}^b$ (OH nm^{-2})	Vicinal OH groups, $\alpha_{OH,\,V}$ (OH nm^{-2})
180-200	4.60	1.20	0.60	2.80
300	3.55	1.65	0.50	1.40
400	2.35	2.05	0.30	0
500	1.80	1.55	0.25	0
600	1.50	1.30	0.20	0
700	1.15	0.90	0.25	0
800	0.70	0.60	0.10	0
900	0.40	0.40	0	0
1000	0.25	0.25	0	0
1100	0.15	0.15	0	0
1200	0	0	0	0

There is a lot of ambiguity in the literature with regards to the use of the terms dehydration (section 2.2.3.1) and dehyroxylation (section 2.2.3.2). With an intent to sort out the ambiguity in all future references to the two terms in this work, the two processes are defined as: a) dehydration referring to the loss of physically adsorbed water due to increases in temperature and b) dehydroxylation refers to the condensation of silanols to form siloxane bonds. Figure 16 illustrates the process of dehydration and dehydroxylation both resulting in the elimination of water.

Figure 16. Process of dehydration and dehydroxylation. Adapted from ref.[4].

2.2.3.3 Rehydroxylation of silica surface

When the dehydroxylated silica surface reacts with water in a vapor or liquid state, silanols groups are formed again and this process is referred to as rehydroxylation (the term rehydration is also used). Young[51] pointed out that complete rehydroxylation of surface can be achieved for only surfaces that has been subjected to thermal pretreatment at temperatures below 400°C. The rate of rehydroxylation is also faster with silica surface subjected to calcination (thermal treatment) less than 400°C due to the fact that the concentration of siloxane bridges is low and each $\equiv Si - O - Si \equiv$ is surrounded by OH groups. It was also stated that any silica surface that has been subjected to calcination in the range of 400- 1100°C can only be partially rehydroxylated and the rate of rehydroxylation is also slower[51-52]. The rate of rehydroxylation is slower because of the increased concentration of siloxane bridges (hydrophobic regions) and decreased concentration of -OH groups. However Agzamkhodzhaev, Zhuravlev, Kiselev and Shengeliya (1969) showed that silica dehydroxylated in the range of 673-1373K can be completely restored to the maximum hydroxylated state (4.6 OH groups per nm^2) by treating with water at room temperature[53]. It was also shown by Agzamkhodzhaev et al[53] that the more surface was dehydroxylated, the longer it took for rehydroxylation and that rehydroxylation can be accelerated by subjecting the silica surface to hydrothermal treatment at 100°C. The reaction that takes place during rehydroxylation is the opposite of condensation reaction and involves the breaking of surface siloxane bonds as shown in Figure 11. It is postulated that rehydration occurs only next to a hydroxyl group and the hydroxylated area grows in certain areas as the hydration proceeds along the boundary between hydrophilic (hydroxylated) and hydrophobic (siloxane) regions[3].

2.2.4 Infrared studies of the silica surface

The discussion of dehydration, dehydroxylation and rehydroxylation is not complete without mentioning the role of IR spectroscopic studies in understanding these processes. Figure 17 shows the IR spectrum of a cabosil sample. The spectrum "a" is that of a sample exposed to laboratory atmosphere and three bands via 3450, 3660 and 3747 cm^{-1} are apparent. The spectrum "b" is that of the same sample after being degassed to remove physically adsorbed water. In this "b" the band 3450 cm^{-1} has disappeared, the intensity of 3660 cm^{-1} has increased and 3747 cm^{-1} is unchanged. As the sample is being calcined (thermal treatment), the band at 3660 cm^{-1} continues to diminish (spectrum "c" is after exposure to 500°C) and finally at 800°C (spectrum "d") only the band 3747 cm^{-1} remains[48, 54]. Table 7 lists all the type of hydroxyl groups and the infrared absorption peaks associated with particular hydroxyl groups[3, 48, 54].
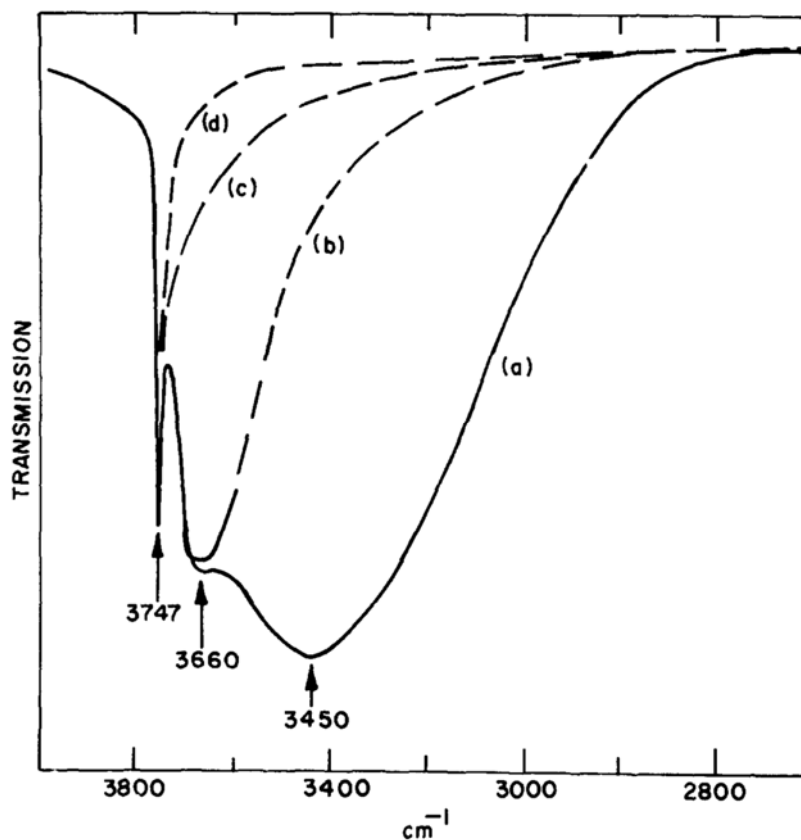
Figure 17. Infrared spectrum of Cabosil. (a) original, (b) after degassing at room temperature, (c)after heating to 500°C, (d) after heating to 800°C Adapted from ref.[48].

Table 7. Absorption peaks of various hydroxyl groups[3].

Type of OH group	Peak (cm^{-1})
Isolated, single SiOH or "free hydroxyl groups	3745-3750
Isolated pairs of adjacent SiOH group (vicinal) mutual hydrogen bonded	3650-3660
Adjacent pairs of SiOH groups with hydrogen bonded to each other	3450-3550
Water molecule adsorbed on the above	3400-3500

2.2.5 Quantification of the silanol number by thermogravimetric analysis

Traditionally IR spectroscopy has been most commonly used for monitoring the surface hydroxylation of silica. However, it is difficult to distinguish between adsorbed water and actual surface hydroxyl groups. It is also challenging to quantify the number of surface hydroxyl groups per unit surface area (silanol number) using IR analysis. Hence, to determine the physically adsorbed water and the silanol number, thermogravimetric analysis (TGA) will be used in this work. TGA offers simple sample preparation, relatively fast analysis and a reasonably accurate quantification of the total silanol number. Figure 18 shows a typical thermo gravimetric analysis of a silica sample. The weight loss within each temperature range can be correlated with loss of one or more particular type of silanols. The content of -OH groups is calculated based on the following formula:

$$No \ of \ hydroxyl \ groups \ per \ nm^2 = \frac{2N_A}{M_{H_2O}} \times \frac{\%weight \ loss}{S_{N_2}} \times \frac{10^{-2}}{10^{18}} \qquad \textbf{(2-1)}$$

where % weight loss is the TGA weight loss for a selected temperature range, N_A is the Avogadro constant, M_{H_2O} is the molecular weight of water and S_{N_2} is the BET surface area obtained from nitrogen sorption measurements.
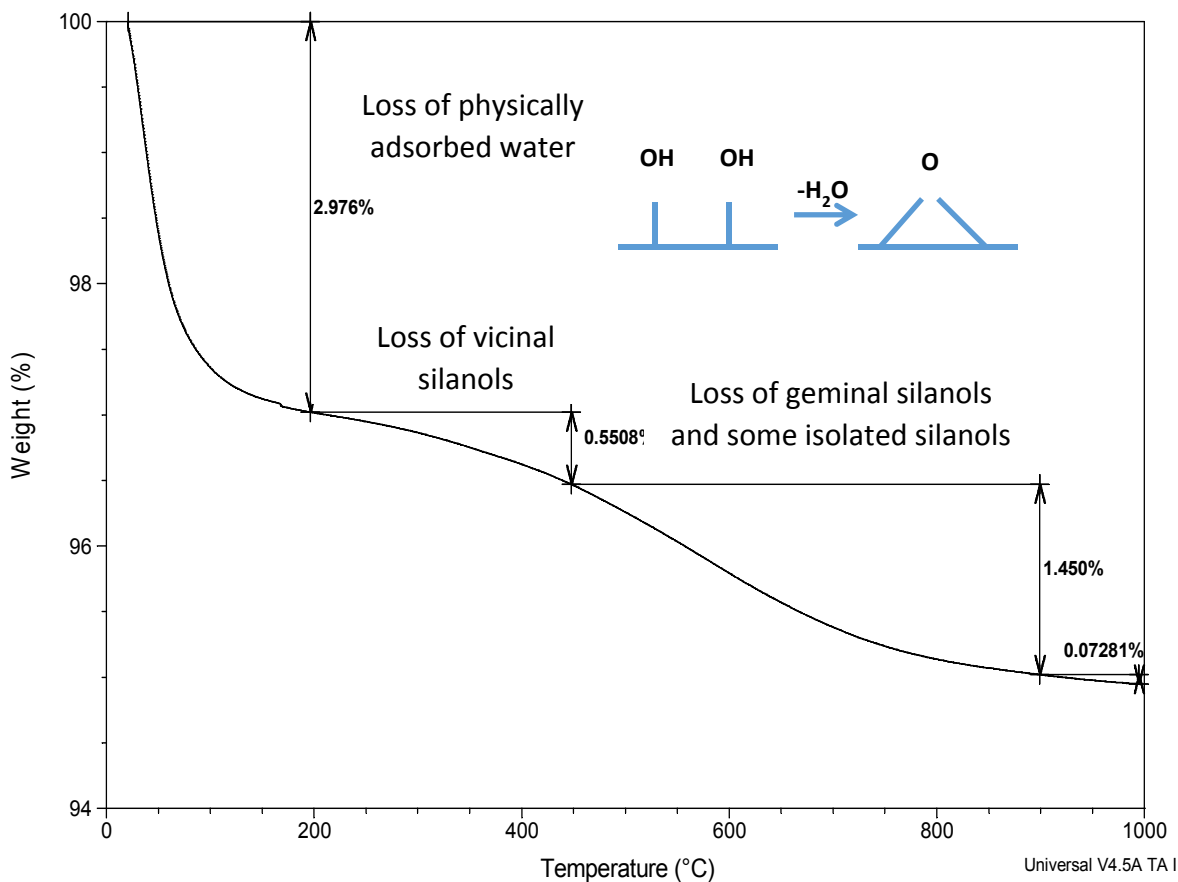
Figure 18. Typical thermogram of thermogravimetric analysis of a silica sample.

Figure 19 shows the distribution of surface groups as a function of thermal pretreatment. Curves 1, 2, 3 and 4 indicates the number of total silanols, number of isolated silanols, number of vicinal silanols and number of Si atoms that are part of siloxane bridges respectively. Figure 14 also indicates that the dehydroxylation proceeds through two stages via subregion IIa (ambient to 400°C and subregion IIb (400°C to 1100°C).
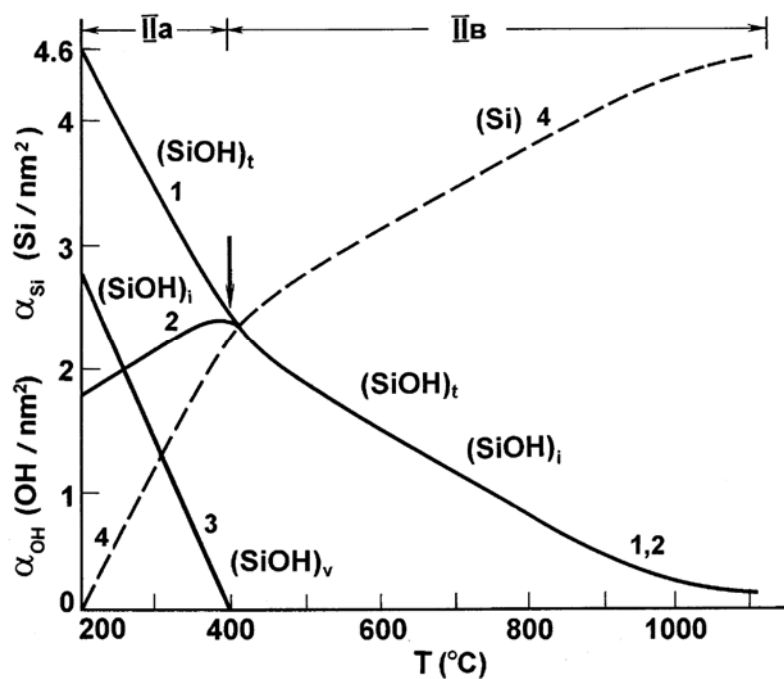
Figure 19. Distribution of the surface groups as a function of the temperature of pretreatment in vacuo (Zhuravlev model-1). Adapted from ref.[6].

2.3 Gas Adsorption Measurements and Characterization

Gas adsorption plays an important role in characterization of wide range of porous materials and amidst all gases and vapors that could be used as adsorptive, nitrogen has remained the most universal adsorptive. With the commercial instrumentation now available, it is relatively easy to determine nitrogen adsorption-desorption isotherms at 77K over a wide range of relative pressures[55].

2.3.1 Determination of surface area

Langmuir's classic work on monolayer adsorption[56] has led to the interpretation of adsorption data for more useful applications. Langmuir regarded the surface as an array of

adsorption sites and according to Langmuir model, the amount adsorbed at the plateau of a Type 1 isotherm (refer Figure 10) corresponds to complete monolayer coverage. When adsorption is confined to monolayer the below Langmuir equation is used

$$\frac{n}{n_m} = \frac{Bp}{1 + Bp} \qquad \textbf{(2-2)}$$

where
$$B = \frac{a_1 k}{z_m \, v_1} e^{q_1/RT} \qquad \textbf{(2-3)}$$

where n is the amount adsorbed on 1 g of adsorbent, n_m is the monolayer capacity, p is the pressure, a_1 is the condensation coefficient, k is a constant given by kinetic theory of gases, q_1 is the isoteric heat of adsorption, R is gas constant, T is the temperature, z_m is the number of sites per unit area and v_1 is the frequency of oscillation of the molecule in a direction normal to the surface[8, 55].

In 1931 Benton and White[57] measured the isothermal sorptions of nitrogen, carbon monoxide and hydrogen by reduced iron, at pressures up to one atmosphere and over a range of temperatures, including 78 K. This work prompted Brunauer and Emmett[58] to adopt gas adsorption for surface area determination and they found that adsorption of isotherms of nitrogen and several other gases were all of sigmoidal shape (Type II isotherm). Figure 20 shows a typical Type II isotherm showing "Point A" and "Point B". The point at which the linear portion of the isotherm begins termed as "Point B" indicates the completion of the monolayer capacity and the adsorption at Point B should be equal to the monolayer capacity. Point A, which is the extrapolated linear branch cutting the adsorption axis was previously thought to represent the monolayer capacity but was later discarded in favor of Point B.
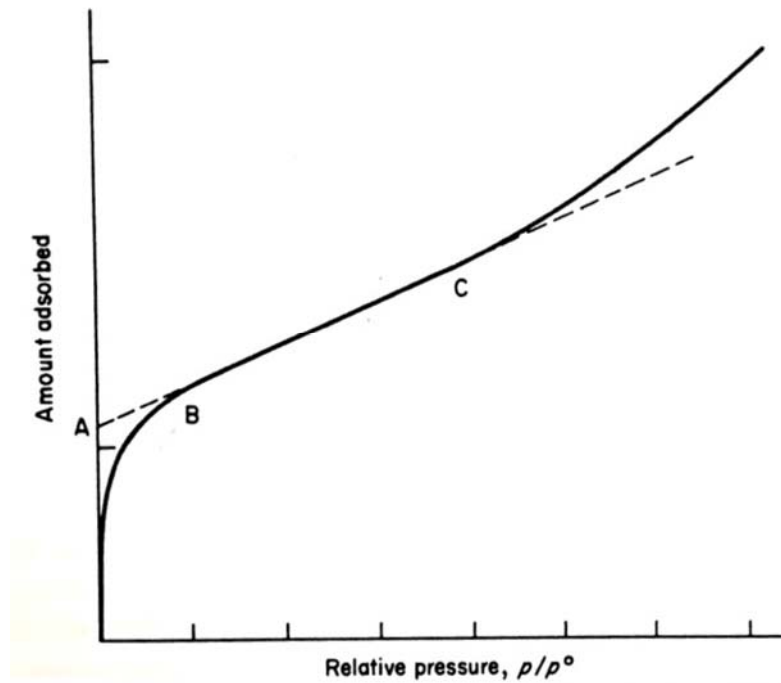
Figure 20. Typical Type II isotherm showing "Point A" and "Point B"[8].

Brunauer, Emmett and Teller[59] in their 1938 work derived the classical Brunauer, Emmett and Teller (BET) model or equation by adopting Langmuir mechanism and introducing a number of simplifying assumptions. BET model enables an experimental determination of the number of molecules required to form a monolayer, despite the fact that exactly one monomolecular layer is never actually formed.

The BET equation obtained from the BET model or theory is listed below:

$$\frac{n}{n_m} = \frac{c\left(\frac{p}{p^0}\right)}{(1 - p/p^0)(1 + (c-1)\frac{p}{p^0})} \qquad \text{(2-4)}$$

For convenience of plotting the above equation can be rewritten as

$$\frac{1}{n(p/p^0 - 1)} = \frac{1}{n_m c} + \frac{c-1}{n_m c}\frac{p}{p^0} \qquad \text{(2-5)}$$

49

where, p^0 is the saturation vapor pressure, c is known as c-constant and given as

$$c = e^{(q_1 - q_L)/RT}$$
(2-6)

where $(q_1 - q_L)$ is net heat of adsorption, R is gas constant and T is temperature.

When n/n_m is plotted against p/p^o BET equation provides a curve with the shape of type II isotherm as long as the value of c is greater than 2. Two major criticisms of the BET model include: 1) the model assumes all adsorption sites on the surface to be energetically identical (when in fact most surface are energetically heterogeneous), 2) the model considers only the vertical interactions (between adsorbent and adsorbate molecules) and ignores the horizontal interactions (between two neighboring adsorbate molecules). Irrespective of the few assumptions that draw criticisms, the BET equation is the mostly widely used for determination of surface area of adsorbents. In the region of relative pressures near completed monolayers ($0.05 \leq p/p^o \leq 0.3$) the BET model and experimental isotherms agree very well, leading to a reliable method of surface area determination. Surface area can be obtained using a single point BET method (only one point in the isotherm) or multi point BET method (at least 3 points up to 7 points or 11 points) in this lower p/p^o region. Figure 21 shows a typical BET (multi point) plot, which is linear plot of $\frac{1}{n(p/p^0 - 1)}$ against p/p^0 as related in equation 2-5. From the BET plot, monolayer capacity n_m is obtained as:

$$n_m = \frac{1}{slope + intercept}$$
(2-7)

where, slope is equal to $\frac{c-1}{n_m c}$ and intercept is equal to $\frac{1}{n_m c}$.

Using the obtained n_m, the monolayer capacity, and with reasonable estimate of adsorbate (nitrogen) molecular area a_m, the surface area of the porous material (A, m²/g) can be calculated using the equation below:

$$A = (n_m a_m N_A)10^{-20} \qquad \text{(2-8)}$$

where n_m is expressed in moles per gram (moles of adsorbate per gram of adsorbent), a_m is in Å² per molecule and N_A is the Avogadro constant. If the monolayer capacity n_m is expressed as the volume of gas (reduced to STP) v_m, the above equation becomes

$$A = (\frac{v_m}{22414} a_m N_A)10^{-20} \qquad \text{(2-9)}$$
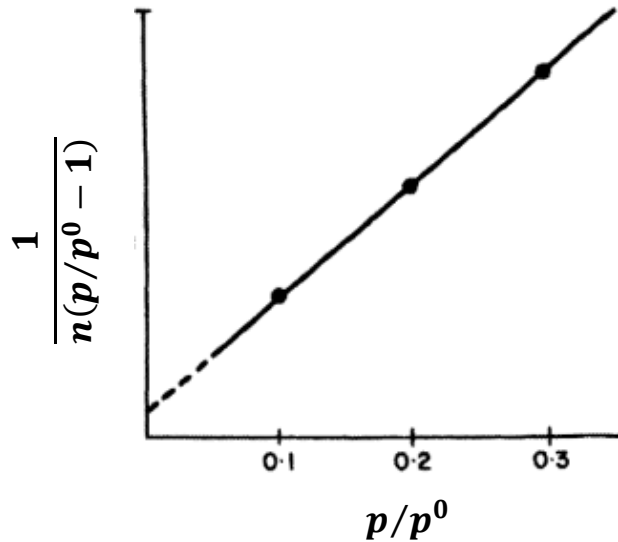
Figure 21. Typical BET plot[40].

The BET plot is dependent on the adsorption system (both adsorbent and adsorbate) and the operational temperature and hence the monolayer capacity, n_m, should be obtained from the best linear fit for that region of the isotherm which includes point B as shown in Figure 20. Brunauer, Emmett and Teller[59] proposed that a value of 16.2 Å² be used as the value of a_m of

nitrogen independently of the nature of the surface. However the correctness of that value has been questioned by several researchers[3, 8] leading to several studies trying to understand the dependence of a_m on the nature of the surface.

Jelinek and Kovats (1994) demonstrated that on highly energetic surfaces, such as surface hydrated SiO_2 or partially dehydrated silica, the orientation of N_2 is upright with a cross-sectional area of 13.5 $Å^2$. For a low energy surface, such as organic modified silicas (C_8,C_{18} modified), a cross-sectional area of 16.2 $Å^2$ is used because it will lay flat on the surface[60]. High c-constant value (which is associated with a sharp point B) indicates strong adsorbent-adsorbate interactions. Typical c-constant values are in the range of 80-150 for nitrogen at 77 K for well-defined monolayers on many non-porous and mesoporous adsorbents. To attain a value of a_m that is characteristic of an adsorbate, two opposing requirements need to met: a) "c-constant shall be high enough to ensure adequate separation between monolayer and multilayer formation"[8] and b) "c-constant must be low enough to avoid appreciable localization of the adsorbate"[8]. With nitrogen, these two requirements can be met on most of the adsorbents and use of a_m equal to 16.2 $Å^2$ will lead to a surface area value that will fall within 20% of the true value.

The monolayer formation occurs by the same mechanism whether the surface is wholly external (Type II isotherm as in non-porous or macroporous solids, see Figure 10) or is largely located on the walls of the mesopores (Type IV isotherm as in mesoporous solids, see Figure 10). Hence, the application of the BET procedure to determine surface area will be the same for non-porous and mesoporous silica surfaces which were studied in this work. Even when nitrogen (preferred adsorbate) is being used as an adsorbate, a divergence of at least 10% in the surface area value must be must be reckoned with. The divergence could be traced to many factors but not limited to variations in outgassing conditions, variations in temperature of the sample during

experiment, inadequate monitoring of the saturation vapor pressure, instrument or apparatus leaks and the purity of nitrogen used.

2.3.2 Pore size characterization

The use of nitrogen adsorption for pore size analysis is based on the application of the Kelvin equation. This expression includes a correction for the multilayer thickness on the pore walls and this approach dates back to late 1940[61]. The first computational procedure was proposed by Schull[61], but the method devised by Barret, Joyner and Halenda (BJH) in 1951 continues to be the most widely used procedure of deriving the pore size distribution from nitrogen isotherm[62]. Prior to pore size characterization of the mesoporous solids, understanding and interpretation of the type IV isotherm is critical to characterize the pore structure of the mesoporous solids. Figure 22 illustrates the typical type IV isotherm which are often seen with inorganic oxide xerogels and other porous solids.

In the low-pressure region, both Type IV and Type II isotherm follows the same ABC path, however, after this point, Type IV begins to deviate upwards taking the path CDE (while Type II follows CN) until high pressure after which the slope decreases as seen in the path EFG. As the saturation vapor pressure is reached it will take the path FGH or FGH'. The hysteresis loop is characteristic of the Type IV and the loop varies from one adsorption system to another. However, at any given relative pressure, the amount adsorbed along the desorption branch FJD is always greater than the adsorption branch DEF. According to Zsigmondy, adsorption is limited to thin layer on the walls along the path ABC of Figure 22, until at D (starting of the hysteresis) capillary condensation commences in the finest pores. Wider pores get filled progressively as the pressure increases and at the saturation pressure, entire pore system is full of condensate[8, 55, 63-64].
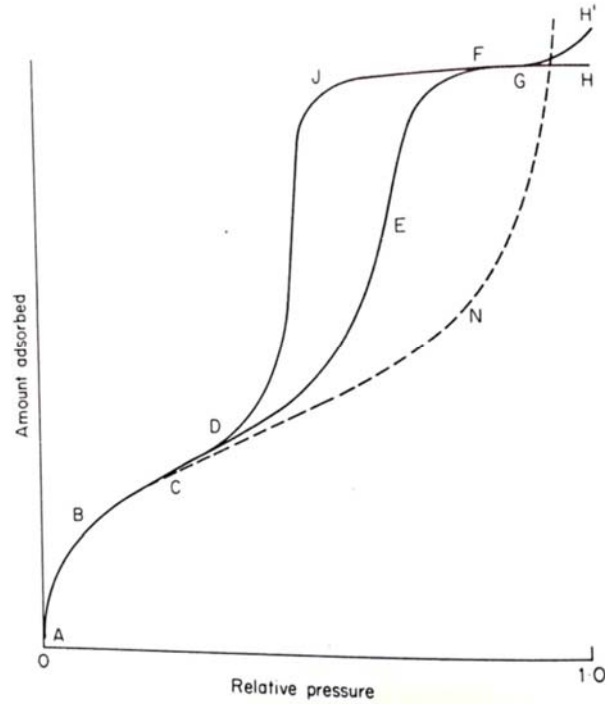
Figure 22. A Type IV isotherm characteristic of mesoporous solids. The corresponding Type II isotherm (dotted line) follows the course ABCN. Adapted from ref.[8].

2.3.2.1 Capillary condensation, hysteresis and the Kelvin equation

The concept of capillary condensation and its quantitative expression in Kelvin equation holds a very important place in the study of mesoporous solids. This Kelvin equation is invariably the basis for all the various procedures for the calculation of pore size distribution from the Type IV isotherm. Using the Kelvin equation rightly helps in understanding the pore system of a mesoporous solid, however the limitations imposed by the thermodynamics of the equation need to be understood. The implicit assumptions involved in the Kelvin equation can be understood by deriving the Kelvin equation, which has been thoroughly discussed in the book chapter by Gregg and Sing[8]. Since capillary condensation is connected with the curvature of liquid meniscus, the discussion and the derivation starts from Young-Laplace equation which relates the pressures on opposite sides of a liquid-vapor interface.

54

To provide an interpretation for the hysteresis, Zsigmondy[8, 64] put forward the theory of capillary condensation by making use of the principle established by Thomson[63] (later Lord Kelvin) on thermodynamic grounds. Thomson established that the "equilibrium vapor pressure, p, over a concave meniscus of liquid, must be less than the saturation vapor pressure, p^o, at the same temperature, which implies that a vapor will be able to condense to a liquid in the pores of a solid, even when its relative pressure is less than unity"[8]. Thompson's original equation was further customized to suit adsorption data and resulted in the "Kelvin equation" which is as follows:

$$ln\frac{p}{p^o} = \frac{-2\gamma V_L}{RT}\frac{1}{r_m}$$

(2-10)

where p/p^o is the relative pressure of vapor in equilibrium with a meniscus having a radius of curvature r_m, γ is the surface tension of the liquid adsorptive, V_L is the molar volume of the liquid adsorptive, R is gas constant and T is the temperature.

It is to be noted that during the process of capillary condensation during adsorption, the pore walls are already covered with an adsorbed film, having a thickness t (referred to as statistical thickness). Hence, the capillary condensation does not happen directly in the pore itself but somewhat inside the inner core. The process of multilayer adsorption, pore condensation and hysteresis in a single cylindrical pore is schematically illustrated in Figure 23. At lower relative pressures, the adsorption process in mesopores is comparable to that on planar surfaces. After completion of monolayer formation (A) multilayer adsorption (B) commences and continues until a critical thickness (C) is reached. Capillary condensation then occurs inside the core of the pore (transition from C to D in the isotherm) and D (plateau region of the isotherm) reflects the state where the pore is completely filled with liquid and separated from the bulk gas phase by a hemispherical meniscus. At relative pressures corresponding to E (less than the pore condensation

pressure corresponding to C), pore evaporation begins by a receding meniscus and continues until the hysteresis closes at relative pressure corresponding to F. The point F represents the situation of an adsorbed multilayer film which is in equilibrium with a vapor in the core of the pore and the bulk gas phase[40].
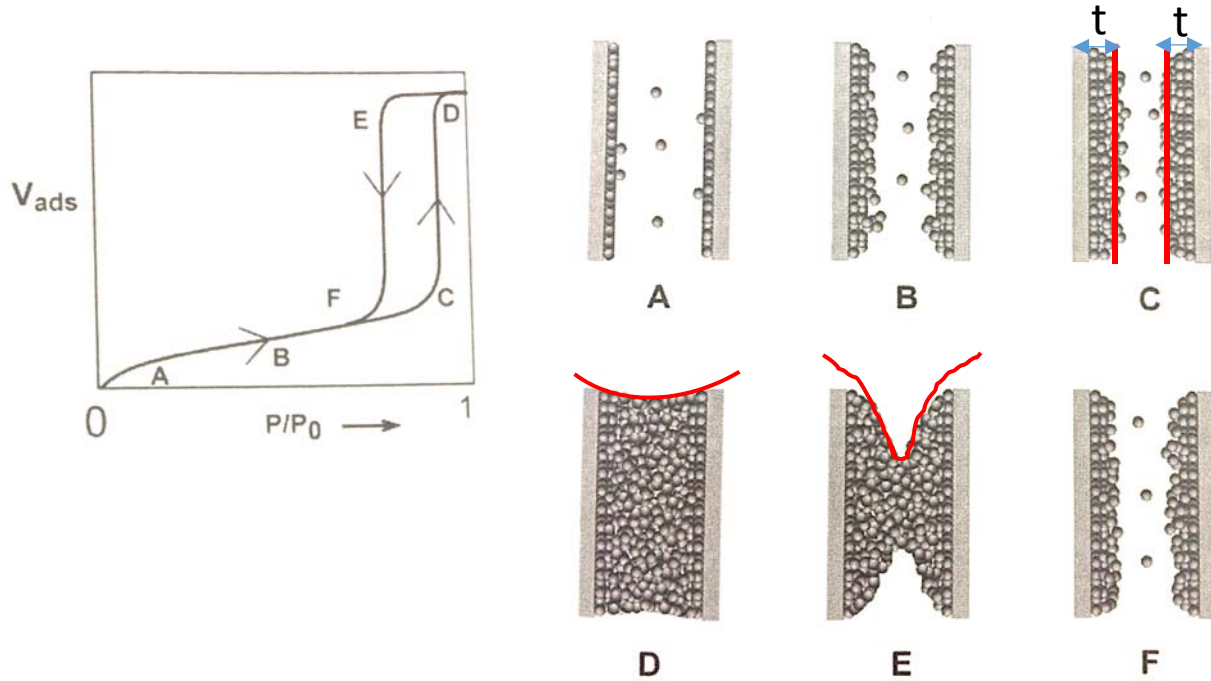
Figure 23. Schematic representation of multilayer adsorption, pore condensation and hysteresis in a single cylindrical pore. Adapted from ref.[40].

To obtain pore size using the conventional Kelvin equation, r_m needs to be converted to pore radius (r_p), which involves resorting to a pore shape model (cylindrical pore and spherical meniscus). The contact angle (θ) between the capillary condensate and the adsorbed film on the walls is also required to correctly use the Kelvin equation to determine the pore size. Figure 24 illustrates the relation between r_m, r_p, r_c (core radius), t and θ.
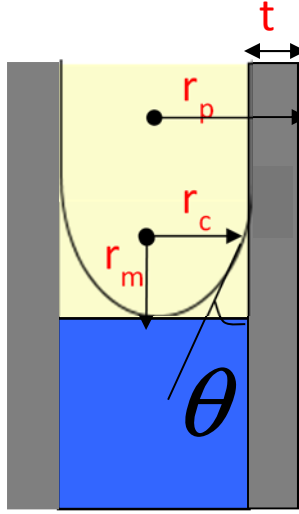
Figure 24. Relation between r_m of the Kelvin equation and the core radius r_c for a cylindrical pore with hemispherical meniscus. θ is the angle of contact, t is the statistical thickness and r_p is the pore radius (sum of r_c and t).

From the relation shown in Figure 24, we can obtain:

$$r_m = \frac{r_c}{\cos\theta} \qquad \text{(2-11)}$$

Hence Kelvin equation can be rewritten as

$$\ln\frac{p}{p^o} = \frac{-2\gamma V_L}{RT}\frac{1}{r_c}\cos\theta \qquad \text{(2-12)}$$

$$r_p = r_c + t \qquad \text{(2-13)}$$

Hysteresis loops, which appear in the multilayer range of physisorption isotherms, are generally associated with the filling and emptying of mesopores. The region of the Type IV isotherm involved in performing calculations of pore size using the Kelvin equation is the hysteresis loop, where the capillary condensation occurs. IUPAC provides an empirical classification of hysteresis loops[65] as shown in Figure 25. There is a correlation between the shape of the hysteresis loop and the surface (pore size distribution, pore geometry and connectivity) of a

57

mesopore adsorbent. As shown in Figure 25, type H1 is associated with porous materials consisting of well-defined cylindrical-like pore channels. Type H2 is associated with materials that does not have a well-defined pore shape and pore size distribution. Type H3 (no limiting adsorption at high p/p^o) is observed in aggregates that has slit-shape pores. Type H4 is associated with narrow slit pores and in pores in the micropore region[39-40, 65-66]. The origin and mechanism of hysteresis is a still a subject of discussion and the book chapters in Gregg and Sing (1982)[8] and Lowell, Shields, Thomas and Thommes (2006)[40] presents a great discussion on this topic by considering simple pore models such as the cylinder, the parallel-sided slit, the wedge-shape and the cavity between spheres in contact. In all the discussions, a simplifying assumption that the contact angle θ is zero (*cos θ =1*) is made.
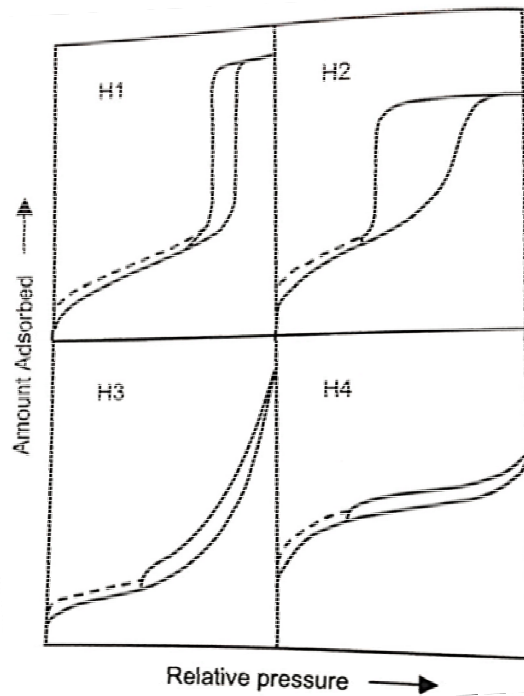
Figure 25. IUPAC classification of hysteresis loops. Adapted from ref.[65].

Briefly, in the independent single pore model where the pores are cylindrical and the cylinder closed at one end B as shown in Figure 26 (a), the condensation and evaporation occur at same

relative pressures leading to no hysteresis. In the case of a cylinder closed at one end, the meniscus is hemispherical (leading to $r_m=r_c$) during both capillary condensation and evaporation and the Kelvin equation in its further simplified exponential form listed as below, provides relative pressure at which both condensation and evaporation takes place[8].

$$\frac{p}{p^o} = \exp\left(\frac{-2K}{r_c}\right) \qquad \text{(2-14)}$$

where $K = \dfrac{-2\gamma V_L}{RT}$
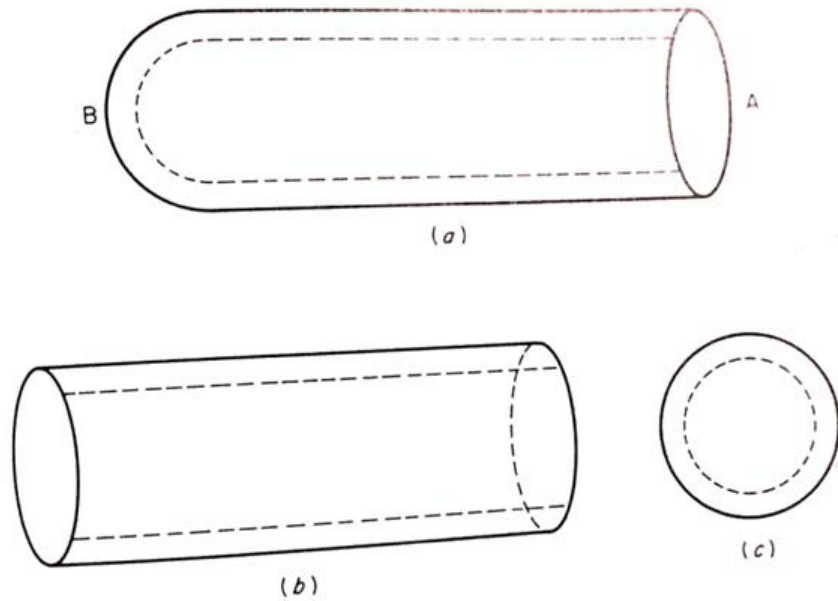
Figure 26. Capillary condensation in cylindrical pores. (a) Cylinder closed at one end, B. The meniscus is hemispherical during both capillary condensation and capillary evaporation. (b) & (c) Cylinder open at both ends. The meniscus is cylindrical during capillary condensation and hemispherical during capillary evaporation. Dotted lines denote the adsorbed film. Adapted from ref.[8].

In the independent single pore model where the pores are cylindrical and the cylinder open at both ends as shown in Figure 26 (b), the condensation and evaporation occur at different relative pressures leading to hysteresis. In this case of the cylinder open at both ends, the meniscus is

cylindrical (leading to $r_m=2r_c$) during capillary condensation and hemispherical ((leading to $r_m=r_c$) during capillary evaporation. The Kelvin equation in its further simplified exponential form listed as below, provides relative pressure at which condensation and evaporation takes place[8]. The values of r_c obtained by either using the adsorption branch (using the relative pressure from condensation) or desorption branch (using the relative pressure from evaporation) should be the same ideally, but in practice this rarely happens.

$$For\ condensation \quad \left(\frac{p}{p^o}\right)_{ads} = \exp\left(\frac{-K}{r_c}\right) \quad \textbf{(2-15)}$$

$$For\ evaporation \quad \left(\frac{p}{p^o}\right)_{des} = \exp\left(\frac{-2K}{r_c}\right) \quad \textbf{(2-16)}$$

The value of the contact angle θ (=0) is subject to a great deal of uncertainty. It has to be kept in mind that in principle the contact angle θ during capillary condensation can differ from zero (can be anything between 0° and 180°). Presently there exists no means for direct evaluation of contact angle for a liquid present in a pore having measurements in the mesopore range. Hence the possible divergence of θ is ignored and θ is assumed as zero in all pore size calculations using capillary condensation data. This assumption of complete wetting of the pores by liquid nitrogen ($\cos \theta = 1$) is assumed for all practical purposes and this assumption has raised attention from theoreticians.

It is important to remember that contact angle θ varies according to the thickness t (statistical thickness) of the adsorbed layer lining the pore walls. Contact angle θ decreases as t increases and approaches zero when t reaches close to 3 or 4 molecular diameters[7-8, 65].

2.3.2.2 Pore size distribution, statistical thickness (t) and Kelvin equation

The computation of mesopore size distribution of a porous solid from the capillary condensation is valid only if the isotherm is of Type IV. Some of the implicit assumptions that are

made in the calculations of pore size distribution are that: (a) the pores are rigid and of a regular shape (e.g. cylindrical capillaries or parallel-sided slits), (b) micropores are absent, and (c) the size distribution does not extend continuously from the mesopore into the macropore range[7-8, 65]. An important question to be addressed while obtaining pore size distribution is the selection of adsorption or desorption branch. Mathematically, the procedure used for pore size distribution is equally valid for both adsorption and desorption branches[8]. But in practice, the pore size distribution obtained on different materials by different researchers indicate that the distribution could have good agreement in some cases and disagreement in other cases as noted in the following discussion. One such reason for the variability between sorption branches is the effect of pore networks. i.e for example if pore blocking occurs, the pore size distribution from the desorption branch will lead to a distorted picture of the pore structure[8, 40]. The IUPAC classification of hysteresis loops (Figure 25) could be used as a guidance in determining the choice of sorption branch for pore size distribution. As an example, for materials (ordered mesoporous systems like SBA-15) that exhibits H1 type hysteresis loop, the desorption branch would be the best choice for pore size analysis, while for materials (disordered mesoporous systems) that exhibit H2 or H3 type hysteresis loops, the adsorption branch would be the best choice[39-40, 66]. Several mathematical models[8, 40] have been proposed for the calculation of the pore size distribution ad one such commonly used model or approach is the Barett-Joyner-Halenda (BJH approach). BJH approach is a procedure for calculating pore size distributions from experimental isotherms using the Kelvin model of pore filling with applicability only to the mesopore and small macropore size range. It is also shown that a much more accurate pore size analysis and wider pore size analysis (complete micro/mesopore size range) is possible with the development and availability of advanced

theoretical procedures based on statistical mechanics (e.g., Non-Local Density Functional Theory (NLDFT)) and molecular simulation[39].

While obtaining pore size distribution (expressed *as dv_p/dr_p vs r_p*), it is very important to take into consideration the amount adsorbed on the walls and account for the adsorbed film thickness or statistical thickness(t). By neglecting the adsorbed film thickness t, the results obtained would be a core size distribution and not pore size distribution. The values of t are derived from standard nitrogen isotherm using the below equation:

$$t = 3.54 \left(\frac{5}{ln\left(\frac{p^0}{p}\right)} \right)^{1/3} \text{Å} \qquad (2\text{-}17)$$

The Kelvin equation as expressed in equation 2-14 can be further reduced to

$$r_c = \frac{4.078}{\log\left(\frac{p^0}{p}\right)} \text{Å} \qquad (2\text{-}18)$$

By using the t and r_c values, the pore radius r_p can be obtained using equation 2-13. Table 8 illustrates the values of r_p and t at different p/p^0 for nitrogen at 77.4 K. The set of values in this table may be considered as adequate for most practical purposes for nitrogen isotherm on hydroxylated silica.

Table 8. Values[8] of r_p and t at different p/p^o for nitrogen at 77.4 K.

	A			B	
p/p^o	r^p, Å	t, Å	*p/p^o*	r^p, Å	t, Å
0.40	15.60	5.35	0.439	17	5.5
0.45	17.40	5.60	0.490	19	5.8
0.50	19.45	5.85	0.555	21	6.2
0.55	21.85	6.15	0.574	23	6.3
0.60	24.9	6.5	0.605	25	6.6
0.65	28.7	6.85	0.667	30	7.05
0.70	33.7	7.35	0.711	35	7.5
0.75	40.5	7.85	0.746	40	7.8
0.80	50.7	8.6	0.800	50	8.6
0.85	67.5	9.65	0.832	60	9.2
0.90	101.9	12.75	0.856	70	9.8
0.95	|199|	|16|	0.875	80	10.5
			0.889	90	11.7
			0.899	100	12.75

2.4 Water Adsorption

Water vapor is present everywhere and profoundly influences material attributes thus making water adsorption studies important and interesting. Water provides many examples of Type III isotherms (see Figure 10) and Type III typically originate through the adsorption of non-polar or polar molecule accompanied with relative weak adsorbent-adsorbate forces. In Type III, the adsorbate-adsorbate interactions will play an important role. In water, the dispersion contribution to its overall interaction energy is very small compared with the polar contribution. The BET procedure for evaluation of monolayer capacity is not applicable to Type III and hence no surface area calculations are made using water as adsorbate[7-8, 40, 55]. In adsorbents that possess pore structures accessible by both nitrogen and water vapor, it would be valuable to compare pore structure curves obtained by both nitrogen and water vapor.

2.4.1 Water t-curves

The methods proposed for complete pore structure analysis are just as applicable to water vapor adsorption as to nitrogen adsorption. However the knowledge of the statistical thickness (t) of the adsorbed water film as a function of relative pressures (t-curve) is critical for the accurate determination of the radius of cores and, therefore for the calculations of contact angles. A review of the t-curves for water adsorption reported in the literature varied significantly and, especially for dehydroxylated and hydrophobic surfaces, were scarce or unknown. At best, water t-curves were reported only for some non-porous adsorbents[67] as shown in Figure 27. To address this issue, the water t-curves were measured for a series of model wide-pore silicas with known silanol content covering the wide range of silanol coverage. The selection of t-curves is of great importance for pore size analysis by water vapor adsorption and Hagymassy, Brunauer and Mikhail (1969)[68] emphasized that that the t-curve should be categorized according to the BET *c* constant of the adsorbent. The raw data and the equations for the t-curves on hydroxylated, dehydroxylated, and hydrophobic TMS silicas are reported (chapter 3) providing the reference data necessary for the quantitative analysis of water adsorption. The proposed method of the contact angles determination by combining water and nitrogen adsorption in chapter 3 depend greatly on the statistical film thickness (t-curve) of the adsorbed water.

A: alumina, N_2 BET area = 125 m^2/g, $V_m(H_2O/nm^2)$ = 7.7-7.9, BET c constant = 24-27.

B: alumina, N_2 BET area = 4 m^2/g, $V_m(H_2O/nm^2)$ = 6.47, BET c constant = 28.

C: silica (Aerosil 200), N_2 BET area = 201 m^2/g, $V_m(H_2O/nm^2)$ = 3.52-3.58, BET c constant = 11.

D: silica (Aerosil 200 calcined at 1000°C and rehydroxylated at 20°C), N_2 BET area = 178 m^2/g, $V_m(H_2O/nm^2)$ = 1.54, BET c constant = 5.

E: graphitized carbon black, N_2 BET area = 83 m^2/g, $V_m(H_2O/nm^2)$ = 0.03, BET c constant = 5.

Adsorbents were pretreated *in vacuo* at 30°C for 4h.

Figure 27. Statistical thickness of adsorbed film of water as a function of relative pressure on non-porous adsorbents. Adapted from ref.[67].

2.4.2 Water Contact Angles

Due to the complexity of real porous solids, direct measurement of the contact angles in pores is hardly possible. At the same time, the applicability of the contact angles measured for flat surfaces in pores is, generally unknown, which calls for the indirect evaluation methods of the pore wetting. This research will employ the combined vapor adsorption study using nitrogen (77K) and water (293K) isotherms to evaluate the water contact angles for a series of ordered mesoporous silicas, including MCM-41 and SBA-15, as well as for conventional silica gels. Figure 28 shows an illustration of nitrogen and water adsorption inside a cylindrical pore showing the extent of wetting and the contact angle. Specifically, the water isotherms were used to determine the most probable Kelvin radius of menisci ($r_m(H_2O)$) during evaporation of liquid water from pores. Then, $r_m(H_2O)$ was compared with the true radius of pores as assessed from

nitrogen isotherms ($r_p(N_2)$). For incomplete wetting, the radius of meniscus r_m, radius of pore

r_p, and statistical film thickness $t(H_2O)$ were related through the known equation below, which

was used to calculate the water contact angles ($\theta > 0$) in pores.

$$r_p(N_2) - t(H_2O) = r_m(H_2O) \cdot cos\theta$$
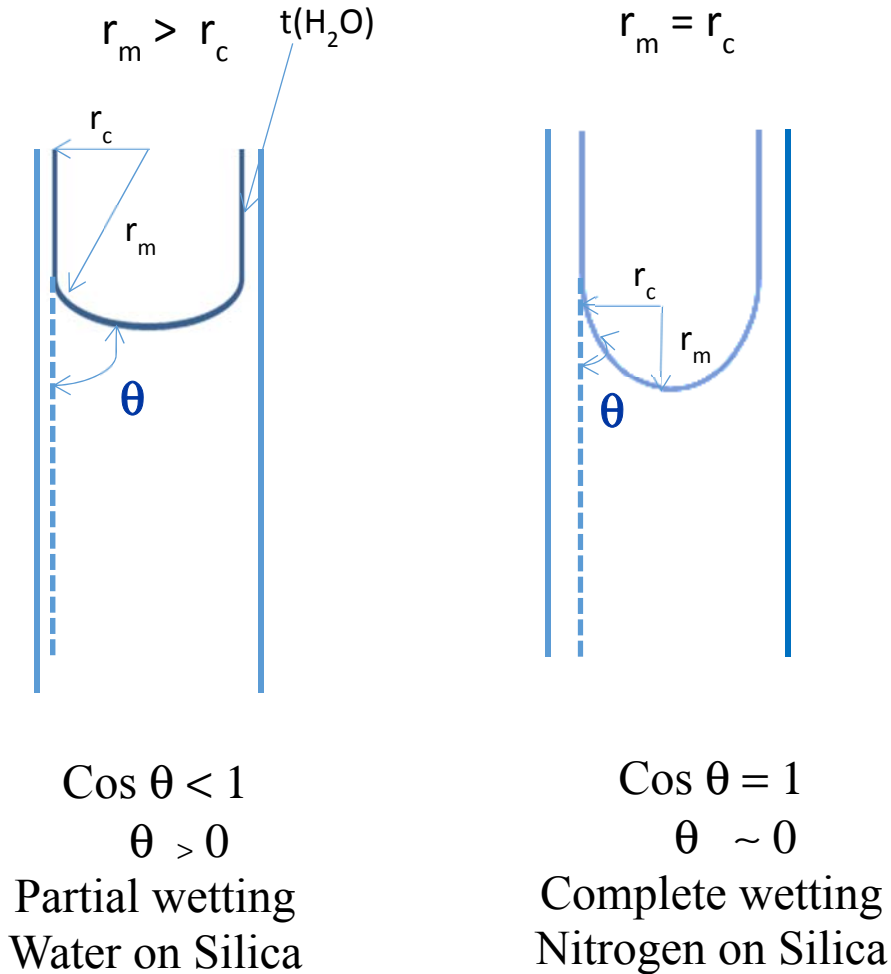
Figure 28. Illustration of nitrogen and water adsorption in a cylindrical pore showing wetting and contact angle. r_c *is the radius of the core,* r_p *is the radius of the pore,* r_m *is the evaporating water meniscus,* $t(H_2O)$ *is the statistical water adsorption thickness,* θ *is the contact angle.*

Chapter 3: Water Contact Angles in Silica Mesopores: The Results of Combined Adsorption Study

3.1 Introduction

Despite the large body of existing research on water adsorption, the deficiencies are apparent. Present work attempts to fill the voids by establishing the dependence between water adsorption and total number of hydroxyls. The surface of most metal oxides is covered by hydroxyl groups which influence many surface phenomena such as adsorption and wetting, catalysis and surface reactions. Surface chemistry of silica is a subject of exhaustive studies owing to a wide variety of practical applications of silica[6].

The hydroxylation of silica surface i.e the number of hydroxyl (-OH) groups on the surface is of utmost importance for its practical applications. Several Infra-Red (IR) gravimetric adsorption studies support that the major adsorption sites on a silica surface are surface hydroxyl groups[6, 43, 48, 51]. At an adequate number of -OH groups the silica surface is hydrophilic and the -OH groups act a site of adsorption while interacting with adsorbate (e.g. water). By the process of dehydration (exposure to high temperature), the -OH groups can be removed and the silica becomes hydrophobic. The hydroxyl groups can be restored again by the process of rehydration (exposure to aqueous environment). Using IR and adsorption studies, Young demonstrated that water vapor physically adsorbs only on the silanol sites for the silica. Young also showed that rehydration from the vapor phase was completely reversible up to 400°C (673K) and the rehydration of silanol sites above 400°C (673K) was not completely reversible[51].

A range of analytical techniques have been used by material scientists to characterize the silica surface in terms of hydroxyl groups, surface area and pore structure[6, 43-46]. Hockey and

Pethica (1961) studied the dehydration and rehydration of silica powders by infrared, water adsorption and gravimetric methods[43]. Smith and Kellum (1966) determined the OH surface density of silica samples using both thermo gravimetric analysis (TGA) and a modified Karl Fischer reagent[44]. The Karl Fischer titration technique provided the physically adsorbed water content while TGA gave the total weight loss from physically adsorbed and chemically bound water. Mueller et al and Wisser et al studied the surface hydroxyl content of silica and other oxides using thermo gravimetric analysis[45-46].

Adsorption methods are sought after for analyzing the porous texture of porous materials[51, 67-70]. The most commonly employed adsorption methods are based on adsorption-desorption isotherms of nitrogen at the boiling point of nitrogen which is 77K. Young determined the surface area of silicas using nitrogen adsorption data and compared these surface areas with gravimetric water vapor adsorption data. The surface areas obtained by water vapor adsorption were only 16% to 25% of the surface area from nitrogen adsorption and hence Young concluded that major portion of the silica is hydrophobic[51]. However, it is to be noted that these experiments were performed on limited non porous silicas.

Use of t curves (graphical comparison of two isotherms obtained from non-porous reference adsorbent and the porous material under investigation) has been adopted to understand the surface character of adsorbents. Hagymassay, Brunauer and Mikhail (1969)[68] and Naono and Hakuman (1991)[67] previously reported nitrogen and water t curves for various non-porous adsorbents. Using the above reported standard t curves for water and nitrogen Naono and Hakuman later characterized a set of porous silica gels[69]. Naono and Hakuman determined pore size distribution curves for various adsorbents from the isotherms of both water vapor and nitrogen gas[67, 69]. It was shown that when water isotherms were used for analysis of porous structure, pore

size distribution can be calculated to a 0.9 - 1.1 nm in pore radius as opposed to only 1.7 nm when nitrogen isotherms were used. For some adsorbents no hysteresis was seen in the nitrogen isotherm while a definite hysteresis was seen in water isotherm indicating that capillary condensation of water vapor takes places in the smaller pores whose radii are less than 1.7nm. This illustrates that water vapor can see pores that are not seen by nitrogen and hence water vapor isotherms give more fruitful information of the porous texture[69]. Even for practical applications, such as using silica adsorbent as a dehumidifier, it would be more valuable to have the adsorption of water vapor on silica rather than adsorption of nitrogen on silica.

Water vapor adsorption work performed by Young[51] focused only on non-porous silica and by Naono and Hakuman[67, 69] focused only on very limited adsorbents. Previously in the literature, it was suggested that there exists a universal t-curve and this was independent of the nature of the sample. Later, this idea was revised and t-curves or t-curves were devised as a function of the physiochemical and thermodynamical nature of the adsorbent. Hagymassay[68] et al proposed five t-curves in the low pressure region (p/p_0 = 0 to 0.5) and two t-curves in the high pressure region (p/p_0 = 0.5 to 0.9). The t-curves were categorized according to a range of values of the c constant of the BET equation. Raoof, Guilbaud, Van Damme, Porion and Levitz (1998)[70] demonstrated that porous t-curve for water coincided with the t-curve of non-porous adsorbents provided that their BET constants were similar

Most of the t-curves or t-curves available in the literature are based on non-porous adsorbents and their applicability to porous adsorbents largely depends on the similarity in their chemical surfaces and pore sizes. For adsorbents with wide pores, the applicability of non-porous t-curve may be more suitable. However for adsorbents with narrow pores, there is always a possibility of overlapping surface forces from the pore walls[70] and hence the applicability of t-

curves measure on non-porous adsorbents can be challenged. The present research work proposes set of reference water t-curves for a wide variety of porous adsorbents that is primarily based on the number of surface hydroxyl groups on the adsorbent.

In this work, we report the results of systematic study of the water vapor adsorption (room temperature) on surfaces of well-defined chemical composition that included fully hydroxylated silicas, silicas dehydrated at different temperatures, and silicas functionalized through the covalent attachment of organosilanes.

3.2 Experiment

General Information. All chemicals were purchased from Sigma Aldrich (St. Louis, MO, USA) except where noted.

3.2.1 Silicas: Preparation, Hydroxylation, Calcination, Silanol determination, and Grafting with TMS.

Bare SBA-15 silicas were prepared following to the procedures published elsewehere[14, 71]. Three different batches of SBA-15 were made (under similar conditions), their structural characteristics determined by the adsorption of nitrogen are given in Table 9. The hydroxylation of silicas was accomplished by placing ~0.2-0.5 g of silica in ~10 mL liquid water (HPLC grade) in presence of catalytic amount of acid (H_2SO_4). The container was sealed and placed in an oven at 100°C for 24 h. After cooling to room temperature, silica was transferred to glass filter, rinsed with excess of water, and dried at 343K overnight. To reduce silanol population, silicas were calcined at desired temperature (293K - 1273K) overnight. To minimize the exposure of the samples, silicas were placed directly in the adsorption quartz vials. After the calcination, the vial was cooled to room temperature in a flow of nitrogen and immediately used for the adsorption measurements. The amount of surface silanol groups (silanol number[6]) was determined from the TGA weight loss

of silicas in the range 473K -1273K°C at a rate of 10°/min (Q500 Thermogravimetric Analyzer, TA Instruments, USA). The amount of surface silanols was calculated as follows:[72]

$$n_{OH} \, [group/nm^2] = 667 * WL/S_{N2} \qquad \text{(3-1)}$$

where *WL* was the TGA weight loss (mass %) at 200-1000°C S_{N2} was the BET surface area obtained by nitrogen adsorption.

The TMS (trimethylsilyl)-modified silicas were prepared by the reaction of hydroxylated silicas with (N,N-dimethyl-amino)-trimethylsilane as described elsewhere[71]. The progress of the TMS surface reactions was monitored by the chemical analysis made by Schwarzkopf Microanalytical Lab. (Woodside, NY). The grafting density of TMS groups [TMS/nm^2] was obtained as follows:[2]

$$\rho = \frac{6 \times 10^5 \, (\%C)}{[1200 \cdot n_C - MW \times (\%C)]} \cdot \frac{1}{S_{SiO2}} \qquad \text{(3-2)}$$

where *MW* is the molecular weight of the (CH$_3$)$_3$SiO group (89 g/mole), $n_C= 3$, the number of carbon atoms in the grafted TMS group, S_{SiO2} is the BET surface area of bare silica by nitrogen [m^2/g], and %C is the carbon weight percent in the sample.

3.2.2 Nitrogen adsorption isotherms

The adsorption-desorption isotherms of nitrogen (77K) were obtained with a Quantachrome Autosorb-1 analyzer (Boynton Beach, FL, USA) and with a Micromeritics ASAP analyzer (Norcross, GA, USA). The isotherms were measured over a relative pressure p/p$_o$ range from ~0.005 to 0.995 and, on average, consisted of 80-130 adsorption-desorption points. Prior to the adsorption measurements, the silicas were outgassed at 200°C (473K) overnight. The TMS-modified silicas were outgassed at 100°C to avoid the damage of organic groups. Specific surface

areas were calculated via the BET method using the range of relative pressure from ~0.06 to 0.27 and the value for nitrogen cross-section 0.162 nm^2. The total pore volume was obtained from the amount adsorbed at p/p$_0$~0.99. The micropore volume was determined using the *t*-plot and *alpha-s* methods. The pore size distribution and the average (most probable) pore radius $r_p(N_2)$ was calculated by the BJH method from the desorption branch of the isotherm. Complete wetting of the pores by liquid nitrogen (co*s* $\theta = 1$) was assumed. All the calculations were performed using vendor's software.

3.2.3 Water adsorption isotherms

The adsorption-desorption isotherms of water (293K) were obtained using a Quantachrome Autosorb-1 analyzer (Boynton Beach, FL, USA). The isotherms were measured over a relative pressure p/p$_0$ range from ~0.02 to 0.99 and consisted of 78 adsorption-desorption points. Unless specified otherwise, silicas were outgassed at 200°C (473K) overnight. The statistical thickness of the adsorbed water films (t-curves) were determined for the reference silica gel Davisil 1000. Due to the large pore size (r$_p$~50 nm), capillary condensation of water did not occur (up to p/p$_0$~0.99) and its contribution to the adsorption was negligible. The thickness of the adsorbed films was calculated by equation:[8]

$$t[nm] = \frac{0.001 * V_{ads.liq.}(H2O)}{S_{BET(}(N_2)} \qquad \textbf{(3-3)}$$

where $V_{ads.liq.}$ *(H2O)* is amount of liquid water adsorbed (cm^3/g), S$_{BET}$(N$_2$) surface area of silica determined by N$_2$ (39 m^2/g). In the literature, some of the water adsorption data was reported not as t-curves, but as the amount of water adsorbed (Γ) expressed in μmole/m^2 or #H$_2$O molecules/nm^2 vs. p/p$_0$. To compare the data, the conversion between these units was done as follows:

$$t[nm] = 0.018 * \Gamma \left[\frac{\mu mole}{m^2} \right] = 0.03 * \Gamma \left[\frac{H_2O}{nm^2} \right] \qquad \text{(3-4)}$$

3.2.4 Contact angles by water

The distribution of radii of water menisci and the most probable radius r_m was calculated by the BJH method from the desorption branch of the water adsorption isotherms. At the temperature of the experiment 293K, surface tension of water was 72.8 mJ/m^2 and its molar volume 18.05 cm^3/mol, respectively[73]. Using these parameters, the Kelvin equation was:

$$r_m(H_2O) = \frac{1.078}{\ln(p_0/p)} \, [nm] \qquad \text{(3-5)}$$

The contact angles were calculated by equation 2-19 using the most probable values of $r_m(H_2O)$ and $r_p(N_2)$. The values of statistical thickness $t(H_2O)$ were taken at the relative pressure that corresponded to $r_m(H_2O)$. The standard error for the determination of cos θ by equation 2-19 was assessed for two silica samples (hydroxylated SBA-15 and SBA-15 grafted with 25%TMS) from three separate measurements of water and nitrogen adsorption performed for each sample respectively. The highest standard error for cos θ (± 0.009) was determined for hydroxylated SBA-15, which was used for all standard error calculations in the text.

3.3 Results and Discussion

The main focus of this work was to evaluate contact angles and surface energy of SBA-15 silica mesopores using the combined water and nitrogen adsorption isotherms. This task, however, was complicated by the fact that the pore structure and the surface chemistry of the freshly made SBA-15 was altered after its exposure to water vapors during the course of the water adsorption experiment[74-76]. Thus, as a first point of this work, we began with (1) the evaluation of

the changes of the SBA-15 caused by the adsorption of water and (2) the optimization of the hydrothermal treatment aimed to prepare pure SBA-15 silica stable to water.

3.3.1 Structural changes to SBA-15 on exposure to water

To quantify the changes caused by the adsorption of water, we conducted a series of sequential water adsorption-desorption cycles, each followed by the nitrogen adsorption measurements. The representative sequence of water isotherms and the corresponding nitrogen isotherms are shown in Figure 29. As assessed by nitrogen, the surface area and the pore volume of SBA-15 showed a notable ~8-10% decrease after the completion of the very first water adsorption-desorption cycle. The more prolonged exposure of SBA-15 to water vapors resulted in further reduction of the surface area and the pore volume. Overall, six cycles of water adsorption-desorption were conducted for the same SBA-15 silica and the reduction in surface area and pore volume (by nitrogen) was noted after each water cycle, though the magnitude of the changes was gradually decreasing. In addition to the structural changes observed, the adsorption of water also lead to the notable changes of the SBA-15 surface, making it more and more hydrophilic after each completed water adsorption-desorption cycle. Qualitatively, this was demonstrated by the gradual changes in the shape of the isotherm from the convex, Type V – typically observed for hydrophobic surfaces to concave, Type IV – indicating polar surfaces with higher affinity to water[8]. In agreement with previous works[74-75], these changes were attributed to the reaction of the adsorbed water with the hydrophobic siloxane groups producing hydrophilic silanols.

Indeed, the radii of the evaporating water menisci used for the calculation of the contact angles (Table 9) were obtained from the desorption branch of the isotherm. By the time the desorption began, the SBA-15 silica had been in contact with liquid water condensate for many

hours. On average, water adsorption-desorption isotherms were completed in ~70-90 h. We estimated that at least half of this time was spent on the capillary condensation loop, i.e. when liquid water condensate was present in pores. It was, therefore, highly possible that the hydroxylation and surface reconstruction via dissolution/redeposition[74-75, 77-80] of silica was taking place before the system had reached the desorption equilibrium.

SBA-15 silica (as prepared) is inherently hydrophobic and unstable towards water vapor. The improvement of the surface hydrophilicity for the SBA-15 after the exposure to water was also demonstrated by the water pore filling at saturation. In the first water adsorption cycle, the pore volume by water was 0.75 of that by nitrogen. In the second and the third cycles it was 0.78 and 0.80 respectively. We noted, however, that even for the fully hydroxylated hydrophilic silicas (see Figure 29) the pore volume by water was ~0.85, i.e. notably lower than by nitrogen. Similar observations regarding the pore volumes differences by nitrogen and by water were also reported[80-81]. Authors[81], attributed this to the microscopic heterogeneity of the pore surface and the presence of hydrophobic patches. In the following sections of this work, the hydrophobicity and the incomplete wetting of pores of these silicas will be further validated and characterized.

.
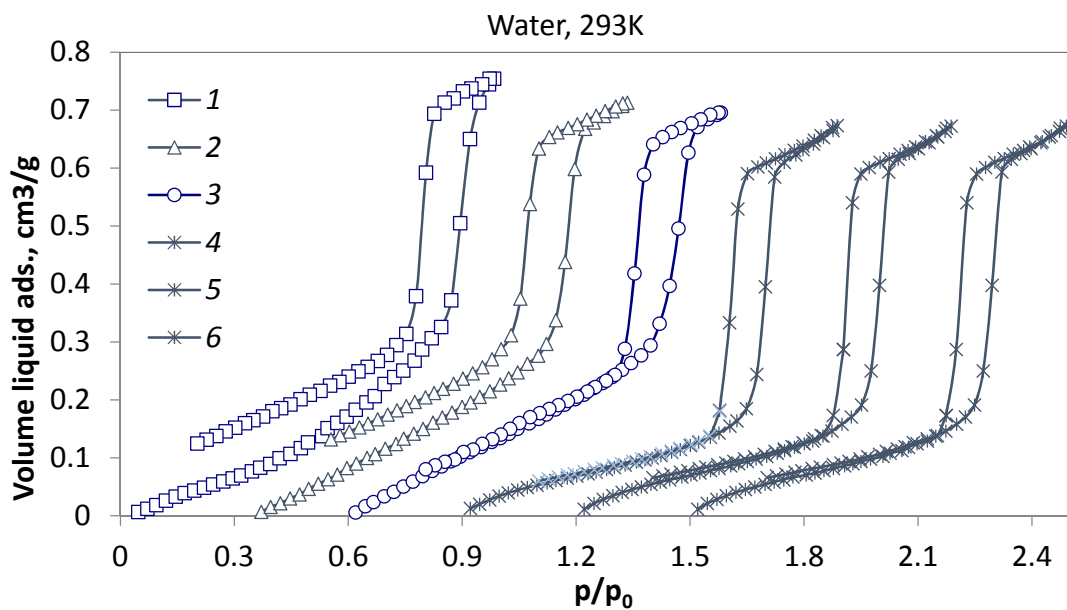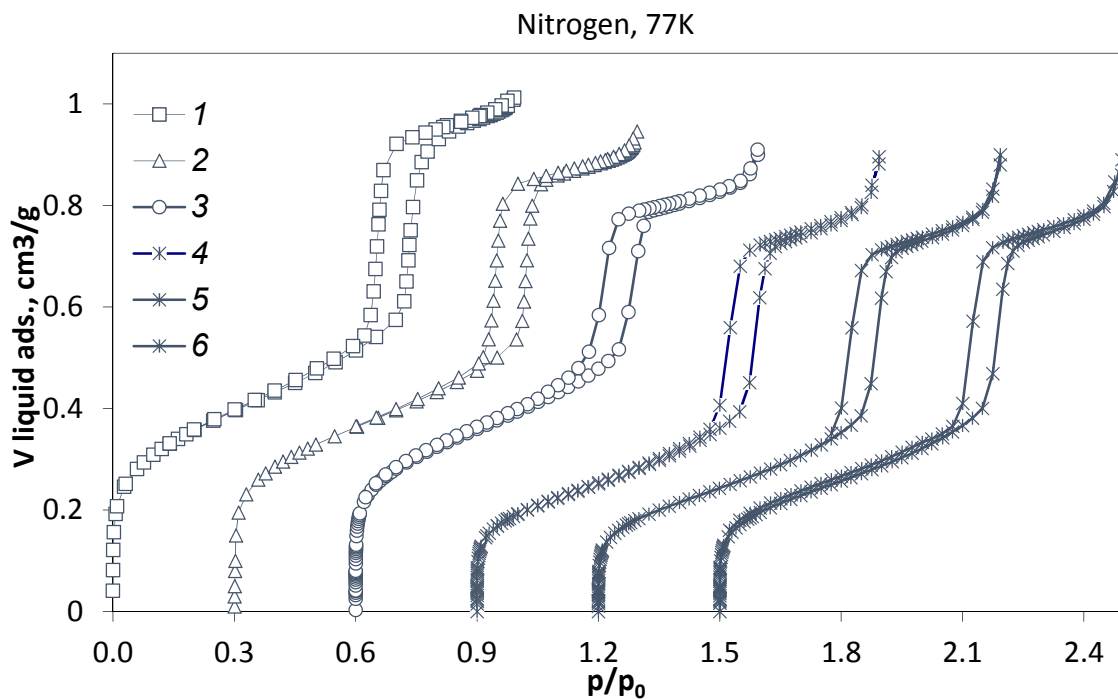
Figure 29. Top: (1-3) - first, second, and sixth consecutive water adsorption isotherms for freshly made SBA-15. (4-6) – first three consecutive water adsorption isotherms for SBA-15 after hydroxylation in liquid water. Bottom: Nitrogen adsorption isotherms for the samples described above. For ease of comparison, each isotherm is shifted by 0.3 p/p0 units in respect to the isotherm to its left.

Table 9. Water contact angles and structural parameters for three batches of freshly made SBA-15 & two batches of MCM-41 silicas and for the same silicas after hydroxylation

Sample	$S(N_2)$ m^2/g	$V(N_2)$ cm^3/g	$r(N_2)$ nm	$r_c(H_2O)$ nm	$r_m(H_2O)$ nm	$t(H_2O)$ nm	Cos θ*	$\theta^§$ deg
SBA-15-I, freshly made	790	1.04	3.30	3.12	4.05	0.18	0.770±0.009	39-40
SBA-15-I after hydroxylation	558	0.84	3.03	2.78	2.80	0.25	0.993±0.009	0-10
SBA-15-II, freshly made	745	1.05	3.25	3.07	3.60	0.18	0.853±0.009	30-32
SBA-15-II after hydroxylation	565	0.84	2.92	2.67	2.70	0.25	0.989±0.009	4-11
SBA-15-III, freshly made	718	0.98	3.21	3.03	4.06	0.18	0.746±0.009	41-43
SBA-15-III, after hydroxylation	587	0.86	3.05	2.80	2.80	0.25	0.993±0.009	0-10
MCM-41-I, freshly made	958	0.77	1.52	1.32	1.32	0.20	1.00±0.008	0-8
MCM-41-I , After hydroxylation	859	0.65	1.50	1.30	1.32	0.20	0.985±0.008	5-12
MCM-41-II, freshly made	974	0.77	1.48			0.20	0.844±0.009	31-33
MCM-41-II , after hydroxylation	863	0.68	1.47			0.20	0.988±0.009	4-12

*cosθ was calculated using equation 3-8

§The range of θ was evaluated from the standard error of cosθ.

3.3.2 Hydrothermal treatment as a means to improve hydrolytic stability of SBA-15

To facilitate the surface hydration and to "complete" the structural changes induced by water, the SBA-15 silicas were subjected to the hydroxylation, the hydrothermal treatment[2], involving the reaction of silica with liquid water at elevated temperature (373K). Three different batches of SBA-15 (Table 9) were tested and, on average, the hydroxylation resulted in ~17% reduction in the pore volume and ~25% reduction in the surface area respectively (Table 9). Also, while the micropore volume for bare SBA-15 was typically ~0.05 cm^3/g, after the hydroxylation it was down to 0.01 cm^3/g or less. Since in presence of the micropores the BET surface area was overestimated[8], the larger relative reduction in the surface area vs. the reduction in pore volumes was consistent with the disappearance of the micropores.

In the literature, the hydrothermal stability of SBA-15 silicas has been studied extensively. Although SBA-15 was reported to retained the pore order under severe conditions like prolonged treatment in boiling water[14], and 600°C (873K) steam[79] most researchers noted that the pore structure of freshly prepared SBA-15 showed dramatic changes within the first hours of contact with water. According to Gouze, Cambedouzou, Parrès-Maynadié and Rébiscoul (2014)[78] as soon as SBA-15 is in contact with water, the silica started to dissolve and re-condense forming an altered silica layer at the pore surface. The redistribution of silica in the matrix resulted in widening of the micropores, smoothening the pore walls, and hydroxylation of the surface[74-75, 77]. The results of this work confirmed previous findings and demonstrated that the native structure of the freshly made SBA-15 suffered major changes upon exposure to water vapors at room temperature. These changes were irreversible as the calcination did not restore the original structure. To conclude this section, we recommend hydroxylation in liquid water as a simple and effective treatment to obtain SBA-15 silicas with improved hydrolytic stability and reproducible properties. After the

hydroxylation, the SBA-15 silicas showed no changes in pore structure after extended period (over a year) of storage under ambient humidity, exposure to saturated water vapor, contact with liquid water, and subsequent hydroxylations. In addition to being hydrolytically stable, the hydroxylated SBA-15 silicas have high number of silanol groups. The average value of cosines of these angles (0.991) was less than 1% smaller than the cosine of zero (cos0°=1), the value of water contact angle attributed to clean fully hydroxylated silica surface[3, 82].

3.3.3 Radius of pores, Radius of water menisci, and Water contact angles

As shown in Figure 30, for bare SBA-15 silica the pore size distributions (PSD) by water was off considerably as compared to the PSD by nitrogen indicating a different type of interaction by water and nitrogen with the silica surface. Next, while the PSDs by nitrogen were nearly unchanged, the position of maximums as well as the width of the PSDs by water were strongly influenced by the exposure of silica to water. After each completed water adsorption-desorption cycle, the difference between the PSDs by nitrogen and water was diminishing. However, only for the hydroxylated SBA-15, the PSDs by water and by nitrogen were in close agreement, Figure 30.

This behavior suggested that, unlike nitrogen, water did not completely wet the surface of the pores. For incomplete wetting ($\theta > 0$), the radius of evaporating water meniscus (during the desorption process) exceeded the radius of the core and were related through the equation[8]:

$$r_c(H_2O) = r_m(H_2O) \cdot cos\theta \qquad \textbf{(3-6)}$$

The radius of the water cores was obtained from the true pore radius (assessed by nitrogen) and statistical water adsorption thickness $t(H_2O)$:

$$r_c(H_2O) = r_p(N_2) - t(H_2O) \qquad \textbf{(3-7)}$$
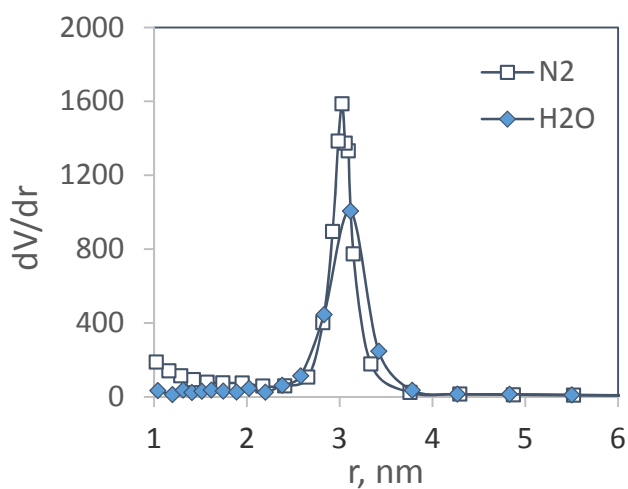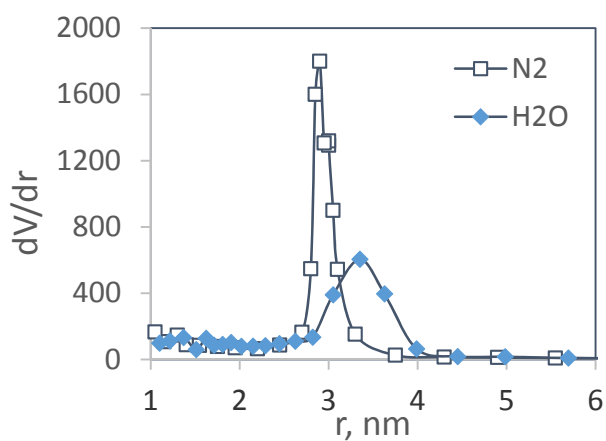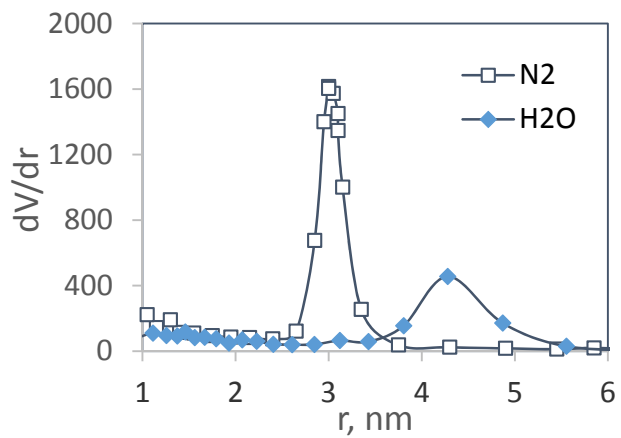
Figure 30. Pore size distributions by nitrogen and by water for the SBA-15 silicas with different exposure to water. From top to bottom: freshly made SBA-15 after the first water adsorption cycle; same silica after four sequential water adsorption cycles; same silica after hydroxylation in liquid water.

After combining equations (3-6) and (3-7), the cosines of water contact angles were calculated as:

$$cos\theta = \frac{r_p(N_2) - t(H_2O)}{r_m(H_2O)} \qquad \textbf{(3-8)}$$

To obtain the parameters needed for the calculation by equation 3-8, water and nitrogen adsorption isotherms were measured for each sample. The pore radius $r_p(N_2)$ was determined from the nitrogen isotherms, the radius of water menisci ($r_m(H_2O)$) - from the water isotherms respectively. The statistical water film thickness $t(H_2O)$ was obtained from the water adsorption data collected for reference silicas.

In the following sections, we use the above described method and report the water contact angles for (1) SBA-15 freshly-made, hydroxylated, and calcined at different temperatures and (2) hydroxylated SBA-15 silicas that were functionalized with hydrophobic trimethylsilyl groups at different surface concentrations.

3.3.4 SBA-15 freshly made, hydroxylated, and calcined at different temperatures.

Table 9 summarizes the contact angles and the parameters used for their calculations for three different batches of freshly made SBA-15 silicas and for the same silicas after the hydroxylation. The water contact angles for bare, freshly made SBA-15 silicas were in the range ~30-43°, with the average value of 38°, demonstrating fairly hydrophobic surfaces. This was consistent with the fact that preparation of the SBA-15 included[11] calcination at 550°C (823K) in order to remove the polymer template and open the pore space. Treatment at such high temperature resulted in substantial reduction of surface silanols (dehydroxylation) rendering surfaces with the increased amount of non-polar siloxanes at the expense of polar silanols. To assess the

contributions of different surface functionalities to wettability, we used the Israelachvili-Gee equation[83]:

$$(1+cos\theta)^2 = f_1(1+cos\theta_1)^2 + f_2(1+cos\theta_2)^2 \qquad \textbf{(3-9)}$$

$$f_1 + f_2 = 1 \qquad \textbf{(3-10)}$$

We treated SBA-15 surface as a mixture of silanol and siloxane groups. Using the water contact angle 0° for a silanol surface (θ_1) and 44° for a siloxane surface (θ_2)[82], we found that the observed average water contact angle of 38° corresponded to a surface mixture of 23% silanols and 77% siloxanes. The actual number of silanols in these SBA-15 silicas, as evaluated by TGA, was in the range 1.3-1.4 OH/nm^2. This was ~30% from the average value of 4.6 OH/nm^2 suggested for fully hydroxylated silica surface[6]. The use of the equation 3-9 and 3-10 for the surface consisting of 30% silanols and 70% siloxanes gave 36°, which was well within the range of the contact angles obtained from the isotherms.

As we mentioned earlier, the freshly made SBA-15 surface had been altered (hydroxylated) during the water adsorption experiment, which was also evident by the contact angles inside the mesopores. Over six sequential water adsorption-desorption cycles the water contact angles decreased after each cycle and, after the cycle #6, they leveled off ~14±3°, approaching the values observed for the hydroxylated SBA-15. The data is shown in Figure 31 and Table 9. We noted that these contact angles were not truly equilibrium as they dependent on the time of contact of silica with water. They should be interpreted as metastable contact angles characterizing the progression of the hydroxylation process of SBA-15. For SBA-15 hydroxylated in liquid water, the water contact angles showed a decrease down to 0-11°, indicating silica surface rich in silanol groups[3, 82]. The number of silanol groups in the hydroxylated SBA-15 silicas by TGA averaged around 5 silanols/nm^2 indicating fully hydroxylated silica surface. After

hydroxylation, the isotherms (by nitrogen and water) and, hence the contact angles were not influenced by the further exposure of SBA-15 to water.
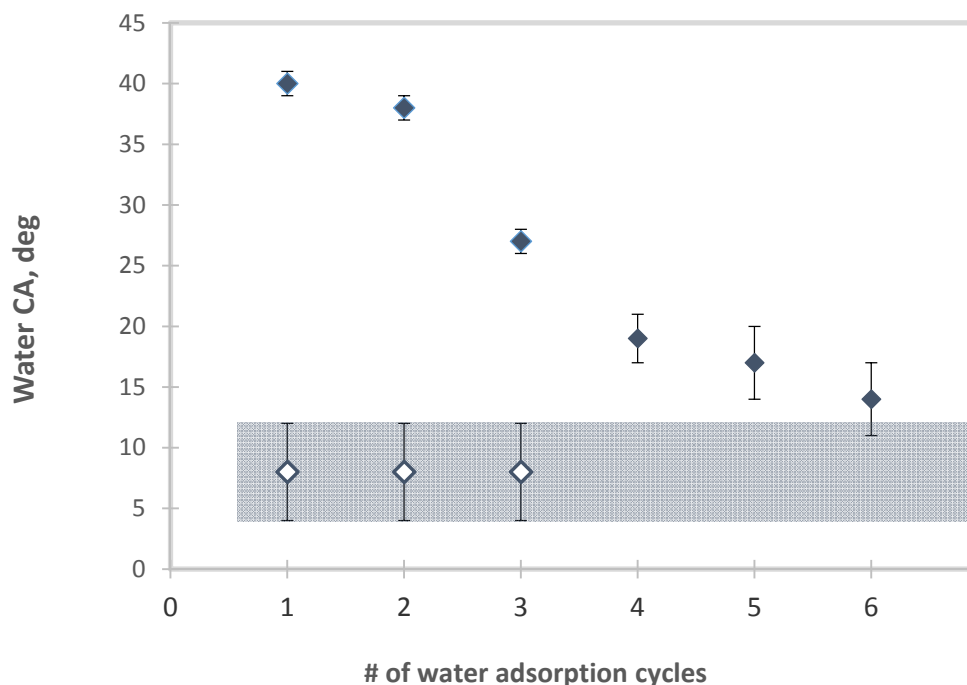
Figure 31. Water contact angles for freshly-made SBA-15 after the first six sequential water adsorption-desorption cycles (closed symbols). Open symbol – data for three sequential water adsorption-desorption cycles for the hydroxylated SBA-15.

The next group of experiments focused on the effect of the SBA-15 calcination temperature on the water contact angles. The starting SBA-15 silica was hydroxylated in liquid water and the calcination was performed at temperatures ranging from 293 to 1073K. The number of surface silanols for calcined samples was monitored by TGA. The results are shown in Figure 32 and Table 10. As assessed by nitrogen, the surface area, pore volume, and pore size distribution of SBA-15 remained nearly unchanged up to calcination temperature of 873K. At higher

temperature (1073K), the surface area, pore volume, and pore size started to show some decrease which was attributed to sintering of silica.

Table 10. Water contact angles and structural parameters for the hydroxylated SBA-15 silicas calcined at different temperatures.

T, K	$S(N_2)$, m^2/g	$V(N_2)$, cm^3/g	$r(N_2)$, nm	$r_c(H_2O)$, nm	$r_m(H_2O)$, nm	$t(H_2O)$, nm	$\cos\theta$	θ, deg
293	558	0.84	3.03	2.78	2.80	0.25	0.993±0.009	0-10
373	558	0.84	3.03	2.78	2.80	0.25	0.993±0.009	0-10
473	552	0.84	3.03	2.78	2.81	0.25	0.989±0.009	4-11
673	544	0.86	3.02	2.84	3.22	0.18	0.882±0.009	27-29
873	536	0.83	2.71	2.59	3.05	0.12	0.849±0.009	31-33
1073	488	0.81	2.55	2.45	3.24	0.10	0.756±0.009	40-42

[§]The range of θ was evaluated from the standard error of cosθ.

As it was anticipated, the contact angles showed a strong dependence on the temperature of silica treatment. The changes in the contact angles observed were consistent with the changes in silanol population with temperature as outlined in Zhuravlev's model of silica surface[6]. According to Zhuravlev[6] the process of dehydroxylation did not start until ~473K and the silicas maintained fully hydroxylated surfaces covered with isolated, geminal, and vicinal silanols with the total number close to its maximum. For silicas calcined at 373K and 473K, the contact angles were ~0-

11º, the same as for fully hydroxylated surface. At ~400°C, most of vicinal silanols were removed producing surfaces that consisted of ~50% of isolated and geminal silanols (from the maximum) and ~50% of siloxane groups. At higher temperatures (873K), the populations of silanols continued to shrink and that for siloxanes to grow respectively. For these silicas, the contact angles showed an increase to ~27-33º indicating replacement of polar silanols by the nonpolar siloxanes occurring in this temperature range. At ~1073K silica surfaces largely consisted of siloxane groups with a small amount of isolated silanols[6]. The contact angle for this sample was ~40º demonstrating
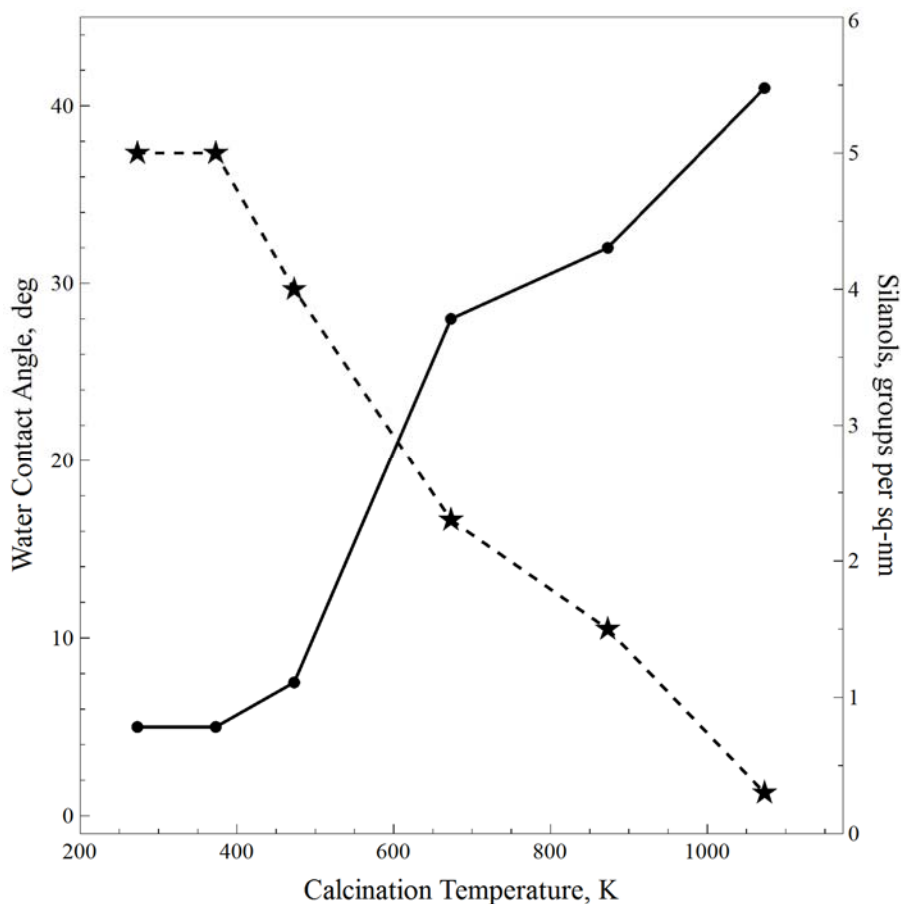
Figure 32. Water contact angles (closed symbols, left axis) and surface silanols per sq-nm (stars, right axis) for the hydroxylated SBA-15 silicas calcined at different temperatures.

hydrophobic surfaces rich in siloxane groups. Using the equation 3-9 with these contact angles, the silanol-siloxane surface composition of the SBA-15 surfaces calcined at different temperatures was calculated, Table 11.

Table 11. Water contact angles and surface composition for the hydroxylated SBA-15 silicas prepared via calcination at different temperatures.

T, K	θ, deg	Surface composition by equation 3-9		#SiOH by TGA, nm^{-2}	Fraction SiOH from max (in parenthesis Zhuravlev's model of silica surface[6])
		f$_1$(SiOH)	f$_2$(SiOSi)		
293-473	0-11	0.90-1.0	0-0.10	5.50	1.0 (1.0)
673	27-29	0.50-0.60	0.40-0.50	2.55	0.51 (0.5)
873	31-33	0.45-0.47	0.53-0.55	1.55	0.31 (0.32)
1073	40-42	0.10-0.15	0.85-0.90	0.80	0.15 (0.16)

§The range of θ was evaluated from the standard error of cosθ.

The results are summarized in Figure 33, which presents an overlay of the contact angles obtained from the isotherms with the fraction of surface silanols (% from max) for SBA-15 silicas calcined at different temperatures. The fraction of surface silanols was (i) determined experimentally by TGA, (ii) calculated by equation 3-9 using the experimental contact angles, and (iii) taken from the literature[6]. A good agreement between these three sets of data was considered as a validation of the method for the contact angle determination described in this work. Representative nitrogen and water isotherms from which all parameters required for contact angle data calculations were obtained are shown in Figure 34.
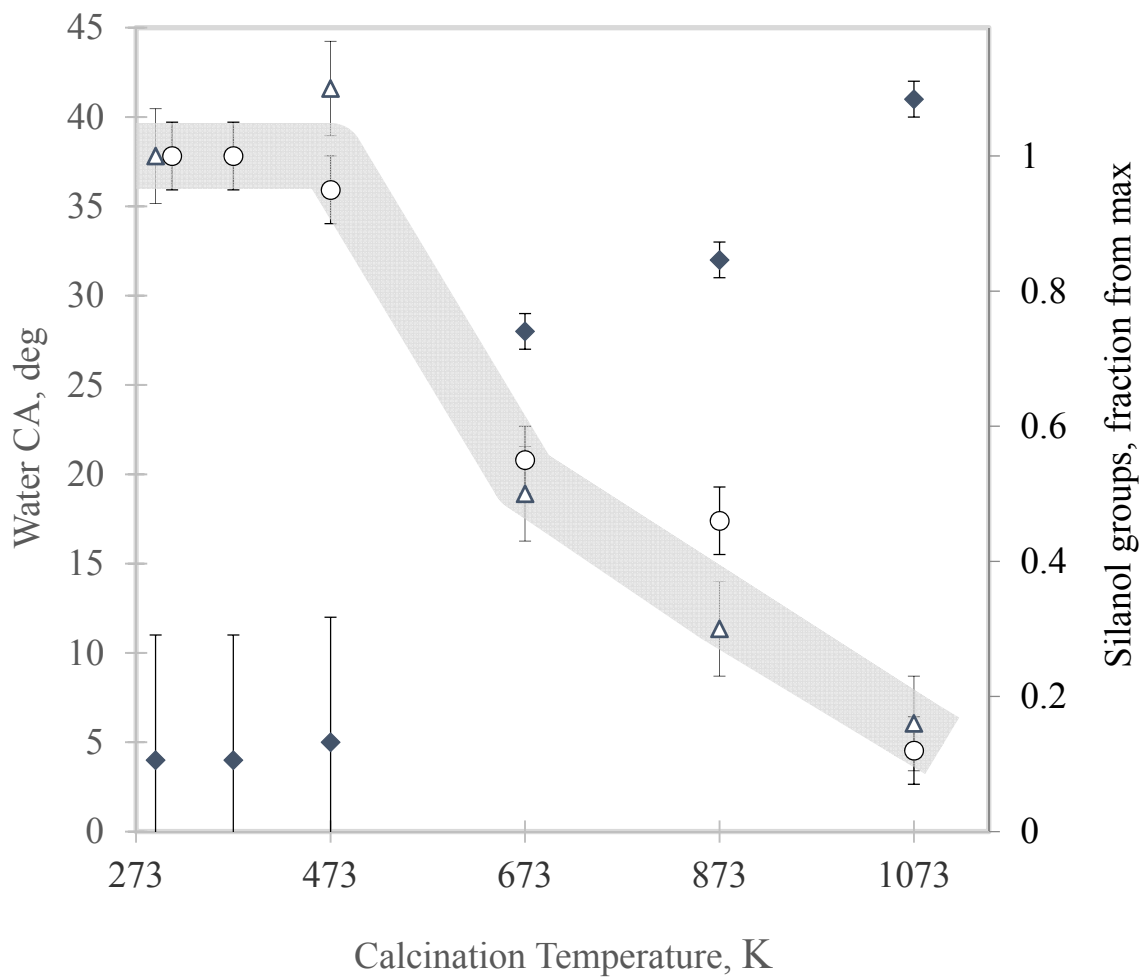
Figure 33. Water contact angles (closed symbols, left axis) and fraction of surface silanols, from maximum value (triangles, right axis) for the hydroxylated SBA-15 silicas calcined at different temperatures. Fraction of surface silanols calculated using equation 3-9 (circles). Shaded strip is the average fraction of surface silanol according to Zhuravlev's model of silica[6].
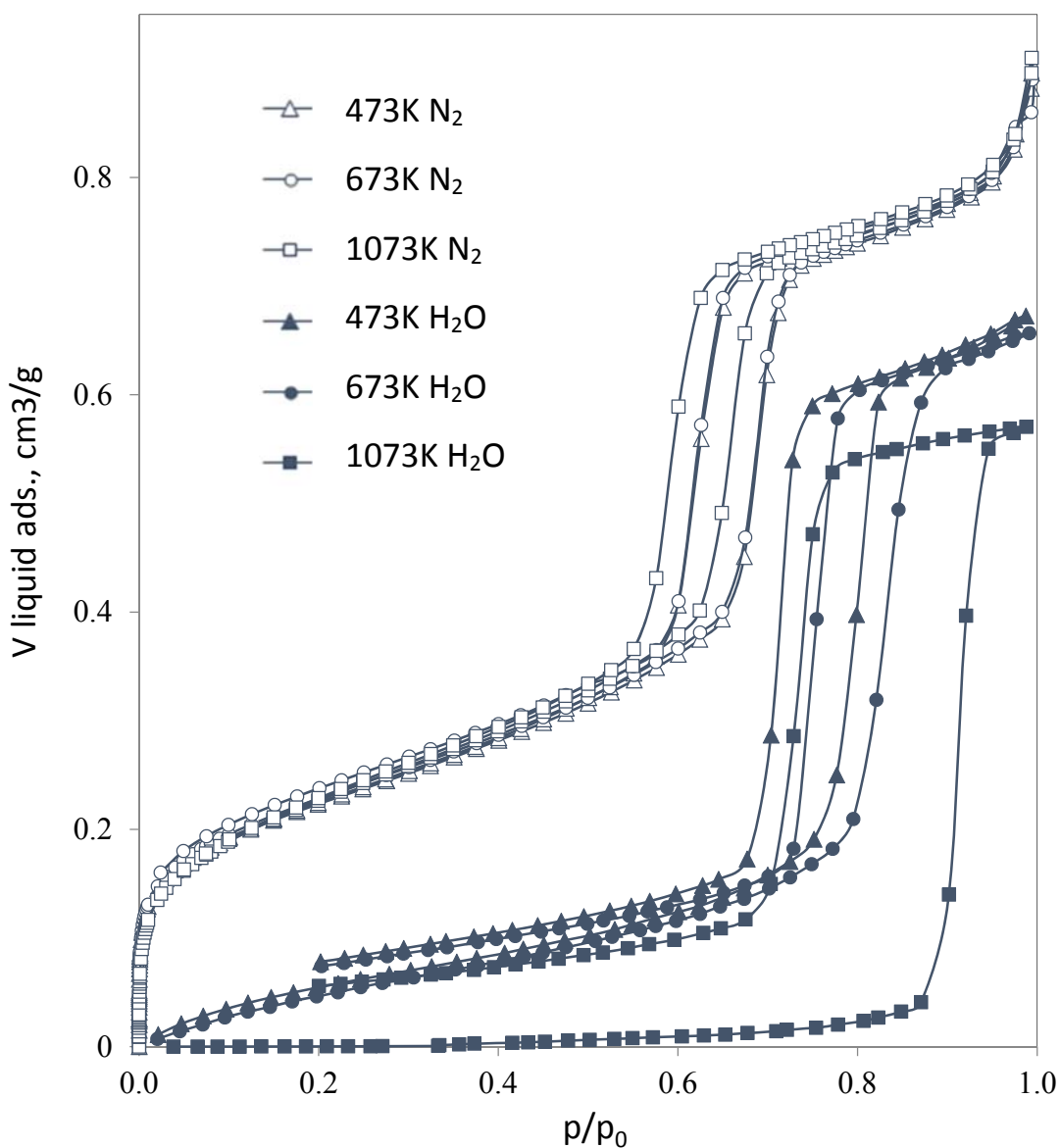
Figure 34. The adsorption isotherms by nitrogen (77K, open symbols) and by water (293K, closed symbols) for hydroxylated SBA-15 silicas calcined at different temperatures.

Note : The isotherms above show volume of liquid adsorbate on the y-axis. The pore volume (at $p/p_o=1$) by water was consistently lower than that by nitrogen. It is known from the literature, that the adsorption of water (at low p/p_o) is primarily controlled by the amount of accessible silanols rather than by the surface area. For this reason, the adsorption of water can be used to estimate the amount of accessible silanols and not for the surface area determination.

3.3.5. SBA-15 with chemically grafted hydrophobic TMS groups

Hydrophobic SBA-15 silicas were prepared via the reaction of $(CH_3)_3SiN(CH_3)_2$ with hydroxylated SBA-15. As a result of this reaction, polar silanols were replaced (and partially screened) by the trimethylsilyl (TMS) groups producing hydrophobic surfaces. By using the dilute solutions of trimethylsilane and limiting the reaction time, a series of silica surfaces with the TMS surface coverage ranging from 0.31 to 2.88 TMS group/nm^2 was prepared. Using the cross-sectional area of TMS groups[84] at 0.35 nm^2, these values corresponded to ~11-100% of TMS surface coverage (by area). The sample characteristics are summarized in Table 12. The nitrogen and water adsorption isotherms are shown in Figure 35.

As assessed by nitrogen, the uniform mesoporous structure of parental SBA-15 was preserved, however the pore volume, surface area, and pore size showed a natural decrease with an increase of the TMS coverage. The decrease in the pore volume and the average pore size was consistent with the attachment of TMS groups on the surface of the pores. Average thickness (*h*) of the TMS grafted layers was calculated from the pore volume decrease (cm^3/g, corrected per gram of silica) and the surface area of bare SBA-15 (m^2/g) as follows:

$$h\ [nm] = 1000 \times \Delta V / S_{SiO2} \qquad \textbf{(3-11)}$$

The thickness values ranged from 0.1 to 0.39 nm for 11 and 100% TMS surface coverage respectively. The value 0.39 nm was in a good agreement with the thickness of a single layer of TMS (0.35 nm) demonstrating closely packed monolayer of TMS groups. The decrease in the surface area observed for the TMS silicas was less obvious. To a certain degree, the decrease in the surface area could be attributed to the micropore blockage by the TMS groups. Although the amount of micropores in the hydroxylated SBA-15 was small by volume (V_μ<0.01 cm^3/g), in their

presence the surface area of bare silica would be overestimated. Thus, closure of the micropores would result in an apparent reduction of the surface area of the TMS-modified silicas. As another possible reason that complicated the analysis of the surface area, we pointed out the uncertainty of the nitrogen cross-section for the modified surfaces. The value of the cross-sectional area of nitrogen for the TMS silicas was probably larger than the standard value 0.162 nm^2 which was used for the calculations. On hydrophobic surfaces, the nitrogen cross section is ~20% greater as the molecules packed more loosely than on silica. So, the use of the same value of the nitrogen cross-section would result in ~20% underestimation of the surface area of the TMS-silicas.

Unlike nitrogen isotherms, the effect of the TMS surface coverage on the water adsorption isotherms was dramatic (Figure 35). The overall shape of the isotherm, the presence of the hysteresis loop and its position, and the total amount of the adsorption was strongly influenced by the TMS coverage. For silicas with high TMS coverage (77, 85 and 100%), the adsorption of water was low over the entire range of pressures, the isotherms were pressed down to the x-axis and no capillary condensation was observed. For the intermediate and low TMS surface coverage (11, 20, 26, and 50%), the capillary condensation was observed yet the amount of water adsorbed at the saturation decreased as the surface coverage of the TMS increased. For the 11% TMS silica, water occupied 72% of the available pore volume (by nitrogen), while for the 50% TMS silica only 20% of the available pore volume was filled by water at saturation. Even at saturation the amounts of water adsorbed were below the theoretical monolayer. Using 0.106 nm^2 for the water cross section, the adsorbed amounts at saturation corresponded to ~25-30% of the monolayer capacity demonstrating high quality hydrophobic surfaces of the pores. Figure 36 shows the initial parts of the water adsorption isotherms for the hydroxylated SBA-15 silicas with different TMS coverage.

Table 12. Water contact angles and structural parameters for the hydroxylated SBA-15 silica modified with TMS.

TMS % by area[&]	V(N$_2$) *cm^3/g	S(N$_2$) *m^2/g	r(N$_2$) nm	C$_{BET}$ (N$_2$)	r$_c$(H$_2$O) nm	r$_m$(H$_2$O) nm	t(H$_2$O) nm	cosθ	θ deg
0 (0)	0.84	565	2.92	142	2.67	2.70	0.25	0.989±0.009	4-11
11 (0.31)	0.82	442	2.67	65	2.48	2.73	0.21	0.908±0.009	24-26
20 (0.56)	0.78	420	2.67	57	2.49	2.92	0.18	0.853±0.009	30-32
26 (0.75)	0.72	413	2.55	41	2.42	3.19	0.13	0.759±0.009	40-42
50 (1.43)	0.70	375	2.48	25	2.41	4.45	0.07	0.542±0.009	57-58
77 (2.22)	0.68	363	2.46	20	No condensation of water in pores				
85 (2.45)	0.66	350	2.42	15	_"_				
100 (2.88)	0.62	353	2.35	11	_"_				

[&]TMS grafting density (group/nm^2) is shown in parenthesis

[*]Pore volume and surface area were calculated per gram of silica. The corrections were made to account for different mass of TMS in the samples
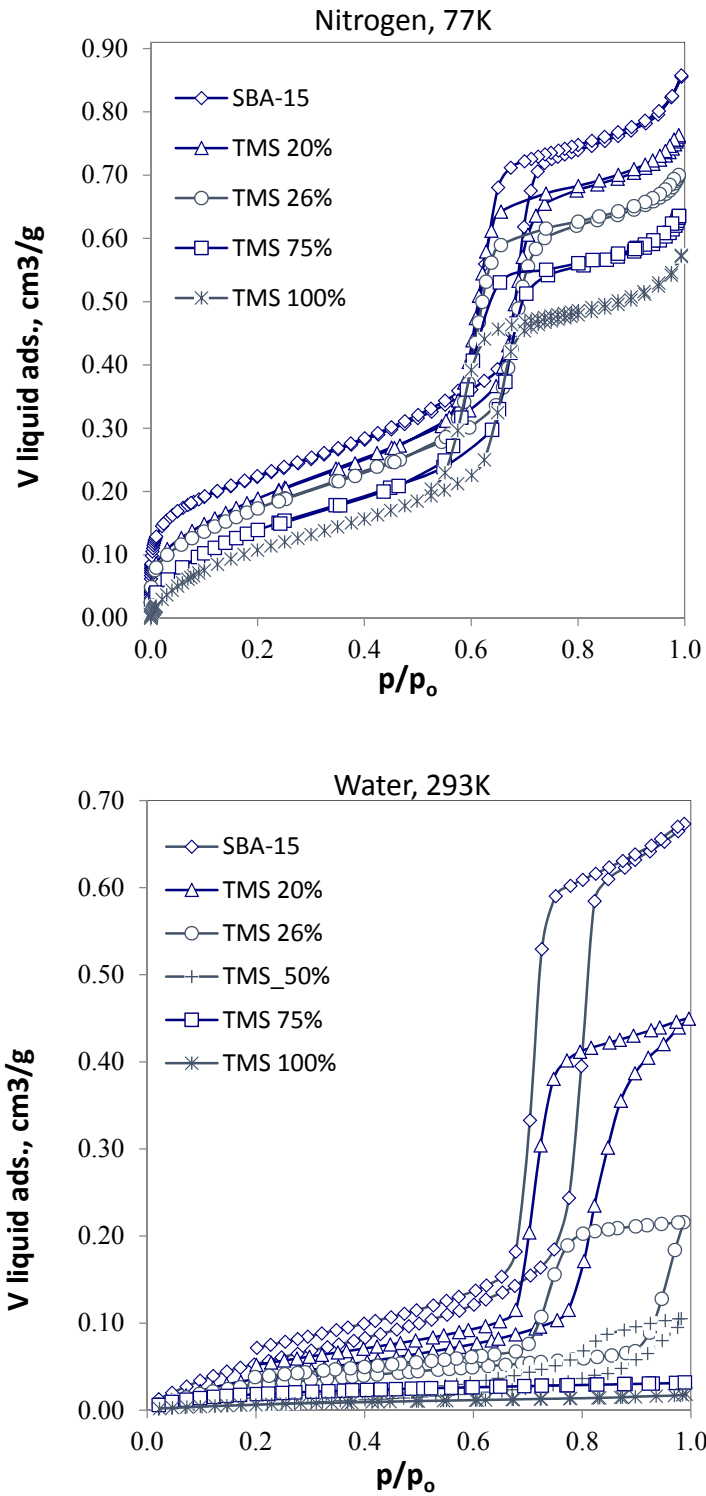
Figure 35. Nitrogen (Top) and water (Bottom) adsorption isotherms for series of SBA-15 silicas hydrophobized with TMS. The fraction of surface coverage is shown in the legends. To account for different mass of TMS in the samples, the adsorption was corrected per gram of silica.
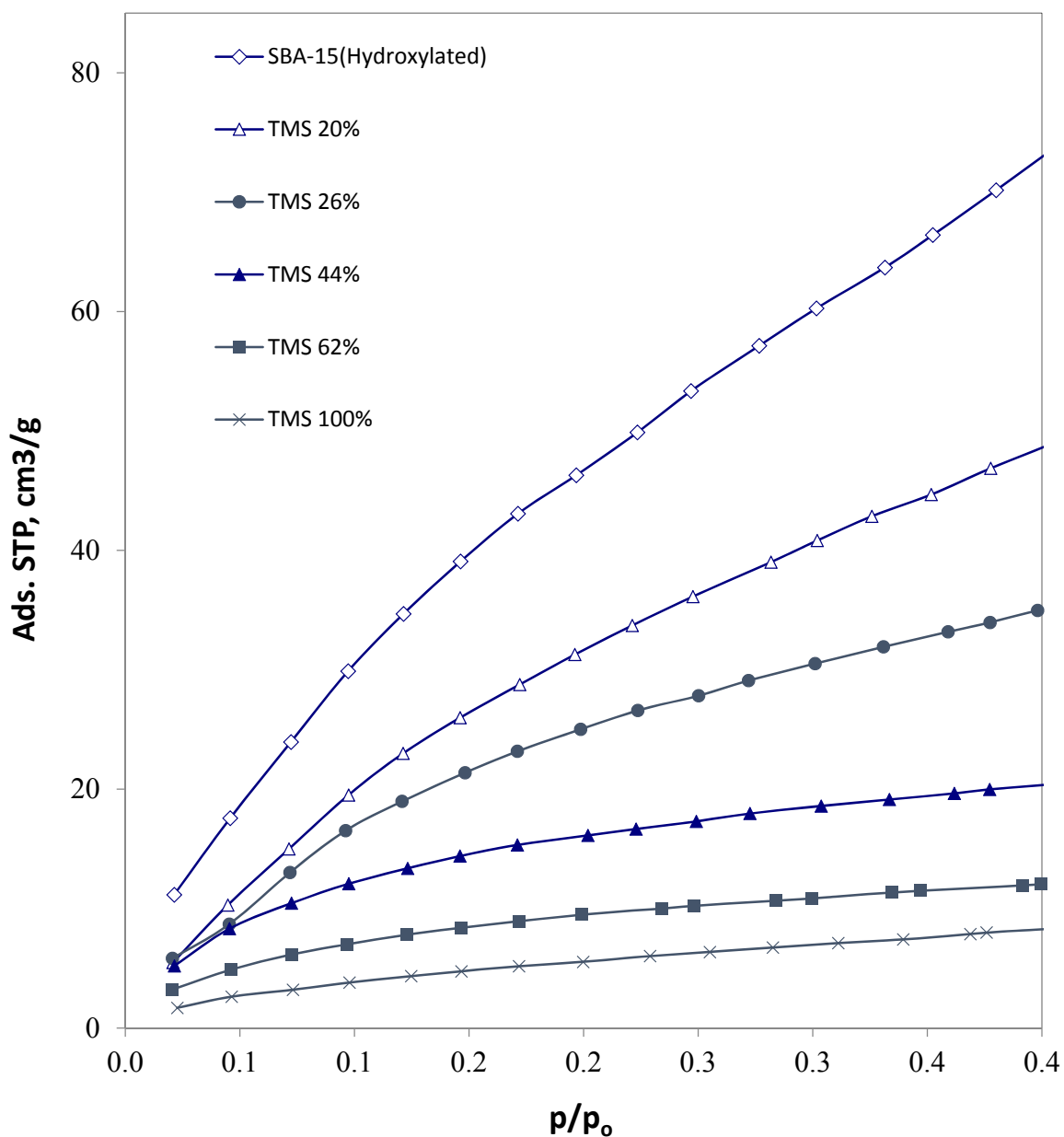
Figure 36. Water adsorption isotherms (initial parts) for the hydroxylated SBA-15 silicas with different TMS coverage.

The pore sizes of the TMS-functionalized silicas were found to decrease due to the attachment of the TMS groups to silica surface. This was clearly demonstrated by the nitrogen adsorption: the hysteresis shifted to lower pressures in accord with the Kelvin equation (Figure 35). On the contrary, the water hysteresis loop was shifting not to the lower but to the higher relative pressure. The magnitude of the shift was higher for silicas with higher TMS surface

coverage, i.e. higher hydrophobicity of the pores. The water contact angles and the structural parameters of the TMS silicas used for their calculations are summarized in Table 12. To evaluate the surface composition of the TMS surfaces we used equation 3-9. Silicas with fractional coverage were treated as a mixture of SiOH ($\theta_1=0°$) and TMS ($\theta_2=108°$)[85] functionalities. The surface compositions calculated from the water contact angles by equation 3-9 were compared with the surface composition determined by the chemical analysis (TMS grafting density), which is shown in Figure 37. The agreement between the grafting density obtained by chemical analysis and the surface compositions calculated using equation 3-9 was remarkable providing further validation of the method.
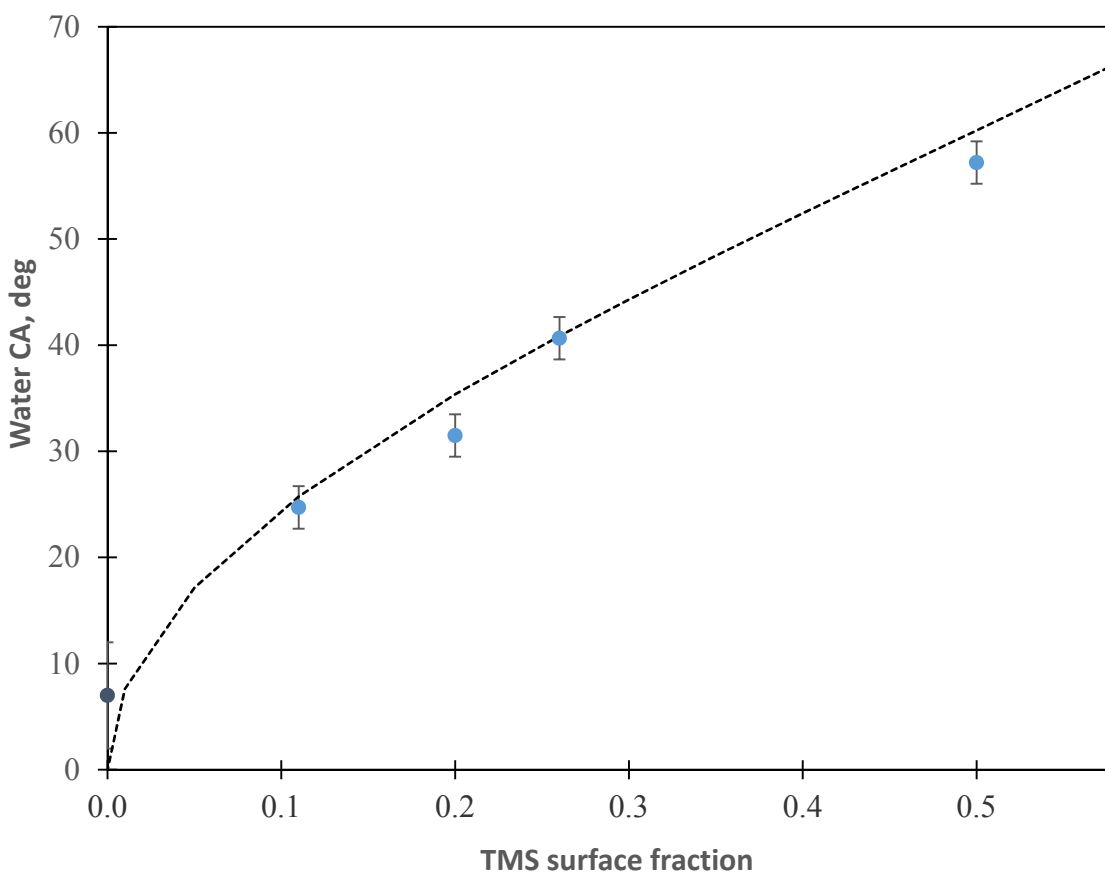
Figure 37. Water contact angles for the hydroxylated SBA-15 modified with TMS groups. Dashed line contact angles calculated by equation 3-9.

3.3.6 Statistical thickness for water adsorption.

The knowledge of the statistical thickness of the adsorbed water film as a function of relative pressures (t-curve) is critical for the accurate determination of the radius of cores (equation 3-7) and, therefore, for the calculations of contact angles described in this work. In the literature, the adsorption of water has been studied extensively and a number of water t-curves have been reported[68-69, 86]. The representative data is compiled in Figure 38. The water t-curves show strong dependence to the nature of silica (water born silica gel[68, 86] or pyrogenic fumed silica[69]) and to its preparation conditions (calcination temperature)[86]. The data presented in Figure 38 serves as a good illustration of the great sensitivity of water adsorption to the surface chemistry of silica, specifically, to the extent of its surface hydroxylation, i.e. the number of silanol groups. For example, the statistical thickness decreased more than 10-fold passing from fully hydroxylated silica to dehydroxylated silica prepared by calcination at high temperatures[86]. Clearly, for the pore size determination and for the calculations by equation 3-6 through 3-8, one should use the t-curve obtained for the reference silica with the similar extent of hydration (silanol number) to the silica under analysis.

Unfortunately, most of the water t-curves available in the literature were reported without the silanol density data. The authors[68] suggested to use the BET *c* constants as a measure of intensity of the adsorption interactions and reported several water t-curves for the adsorbents with different *c* constants. The use of the BET *c* constants, however, seems dubious since the adsorption of water involves strong cooperative interactions (hydrogen bonding) and hardly fits the BET model. To the best of our knowledge, the t-curves for the surfaces of low silanol numbers and for the hydrophobic silicas were not available. To investigate further and

to generate the appropriate t-curves, we have measured the water adsorption for a series of silica

surfaces with known amount of surface hydroxyls as listed in Table 13.
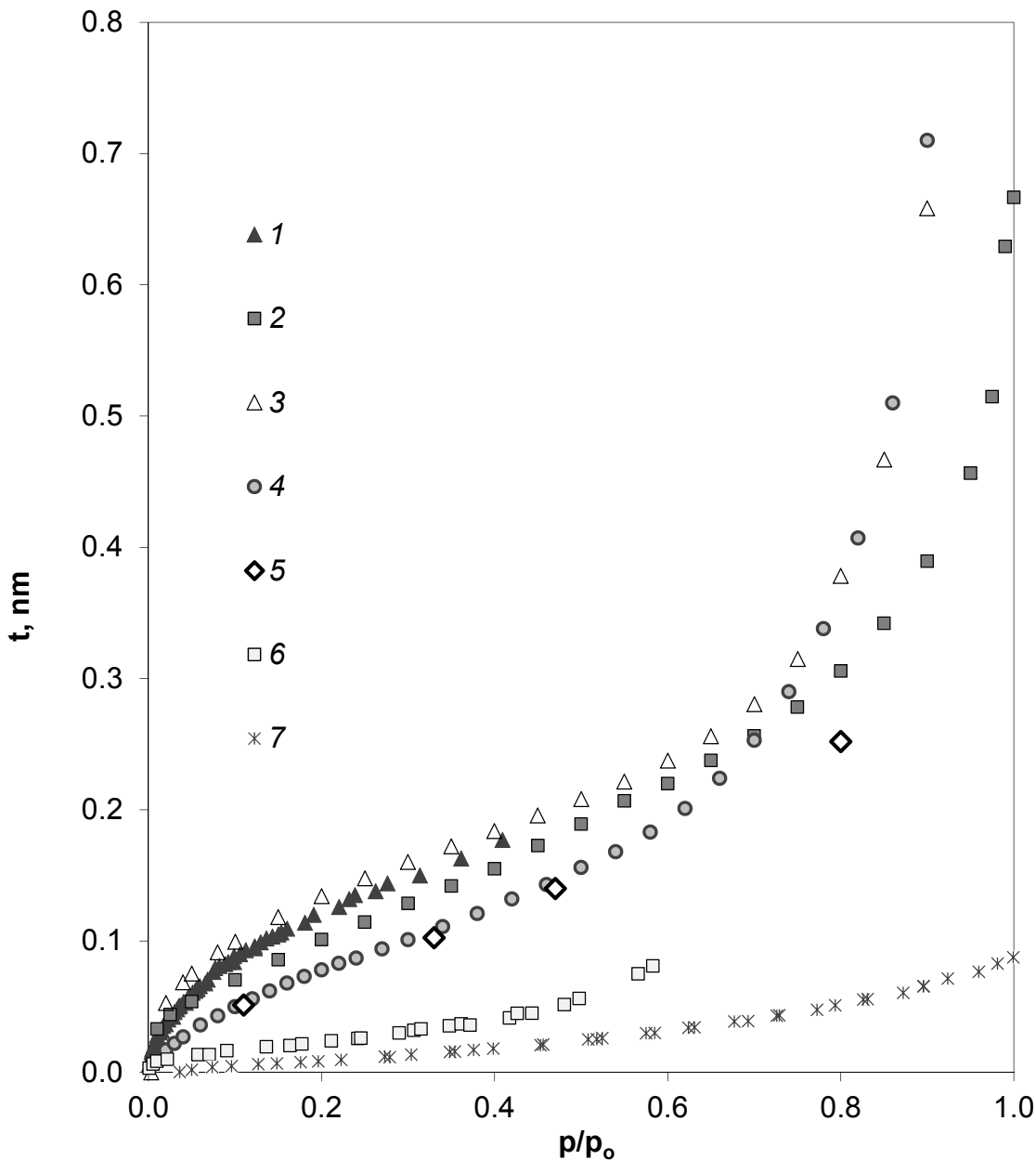
Figure 38. The statistical thickness for water adsorption (t-curves): (1) Hydroxylated silica gel[41], (2) Averaged data for silica gels, quartz, rutile, and zirconium silicate[68], (3) Hydroxylated silica gel Davisil 1000 (this work) (4) Non porous fumed silica[67], (5) Averaged for 11 silica gels[87], (6) Silica gel calcined at 1173K[41], (7) Silica gel Davisil 1000 calcined at 1273K (this work).

Table 13. Series of silica surfaces with known amount of surface hydroxyls and surface area measure by nitrogen isotherm. Water adsorption was performed on all these surfaces to generate t-curves.

#	Adsorbent	Treatment	# OH groups nm^{-2}	$S_{BET}(N2)$ m^2/g
1	Silica gel Davisil 1000	Calcined at 1073K, 1273K	0.2	41
2	Ordered mesoporous silica MCM41	Calcined at 823K	0.8	958
3	Aerosilogel S120	Calcined at 1073K	2.0	39
4	Silica gel Davisil 1000	Calcined at 873K	2.3	41
5	Fumed silica CabOSil M5	As received	2.5	176
6	Ordered mesoporous silica MCM41	Hydroxylated	3.1	859
7	Silica gel Davisil 1000	Hydroxylated	5.0	39
8	Silica gel Davisil 250	Hydroxylated	5.5	302
9	Silica gel Davisil 150	Hydroxylated	5.7	292
10	Silica gel Prodigy	Hydroxylated	6.6	326
11	Silica gel Davisil 100	Hydroxylated	7.5	172
12	Titania P25	As received	8.0	62
13	Titania Alfa Aesar	As received	8.5	258
14	Alumina NanoTeck	As received	10.5	52
15	Alumina ASM	As received	11.5	103
16	Silica Gel modified with TMS	-NA-	~0	30
17	Teflon Spheres	-NA-	~0	8

Note: All silica gels (#1, #3, #4, #7, #8, #9, #10, #11) are porous silica gels with various particle diameters. # 2 and # 6 are mesoporous silicas. #5 is fumed non-porous silica gel. #12 and #13 are Titanium metal oxides. #14 and #15 are aluminum metal oxides. #16 is silica gel modified with hydrophobic TMS. #17 is teflon material (Poly(tetrafluoroethylene)

As a reference silica, a high-purity grade, wide-pore silica gel Davisil 1000 was chosen. Due to the large pore size (r_{pore}~50 nm), capillary condensation of water was not observed up to nearly saturation (p/p_0~0.99) thus providing a data for the t-curve over wide range of pressures. Prior to the measurements, Davisil 1000 was hydroxylated in liquid water at 100°C (373K). As assessed by nitrogen, the hydroxylated Davisil 1000 had surface area 39 m^2/g, average pore radius ~50 nm, pore volume 0.95 cm^3/g, and no micropores (by alpha-s and t-plot methods). By calcination of the hydroxylated Davisil 1000 at selected temperatures (up to 1273K), a range of dehydroxylated silicas was prepared and their silanol numbers were determined by the TGA. The complete structural and silanol data for the Davisil 1000 silicas prepared at different temperatures is given in Table 14.

Table 14. Structural and silanol data for Davisil 1000 hydroxylated and calcined at different temperatures.

T, K (calcination temperature)	S(N$_2$), m^2/g	V(N$_2$), cm^3/g	r(N$_2$), nm	# OH groups nm^{-2}
298 (hydroxylated)	39	1.0	50	5.1
473	40	1.2	48	5.0
673	40	1.2	48	3.7
873	39	1.2	48	1.1
1073	40	1.2	47	0.4
1273	26	0.7	31	0.2

The t-curves obtained are shown in Figure 39 (hydroxylated silicas), Figure 40 (partially dehydroxylated silicas) and Figure 41 (fully dehydroxylated silicas). Based on the behavior of the water isotherms, at least three groups of silica surfaces (and the corresponding t-curves) could be identified. Conditionally, these groups were named (1) fully hydroxylated, (2) partially hydroxylated, and (3) rigorously dehydroxylated silica respectively. The t-curve for the hydroxylated silica was fitted by the following equation:

$$t^{Hydrox}[nm] = 0.1 * \sqrt{\frac{0.919}{0.00037 - log\left(\frac{p}{p_0}\right)}} \qquad \textbf{(3-12)}$$

The t-curve by equation 3-11 was in good agreement with the data previously reported for the hydroxylated silica gel[86] (available only up to 0.4 p/p$_0$) and it was used for the calculations of the contact angles of fully hydroxylated silica surfaces.

The second group was formed by the partially hydroxylated silicas prepared at 673-873K. The water adsorption isotherms for this group of silicas were not reversible: the desorption did not coincide with the adsorption demonstrating notable residual adsorption at low pressure. The low pressure hysteresis, a common feature observed for the water adsorption on partially dehydroxylated silicas[7], was attributed to rehydroxylation – the chemical reaction between the adsorbed water and a siloxane group yielding two surface silanols. Since the composition of these surface was modified by the water adsorption measurement, establishing the characteristic t-curve for this group of silicas was somewhat problematic. Here, we offer two t-curves (desorption) that were used for the calculations of contact angles for silicas prepared at this temperature range:

$$t^{673K}[nm] = 0.217 * \frac{p}{p_0} + 0.02 \qquad \textbf{(3-13)}$$

$$t^{873K}[nm] == 0.122 * \frac{p}{p_0} + 0.007 \qquad \text{(3-14)}$$

The 873K t-curve was used for the calculations of contact angles for bare freshly made SBA-15. The third group of surfaces was formed by rigorously dehydroxylated silicas that were prepared at 1073 and 1073K. As evidenced by the near absence of the adsorption hysteresis, the rehydroxylation of these deeply dehydroxylated surfaces over the course of the water adsorption measurements was negligible. The t-curve for these silicas surfaces were fitted with the equation:

$$t^{Dehydrox}[nm] = 0.074 * \frac{p}{p_0} + 0.004 \qquad \text{(3-15)}$$
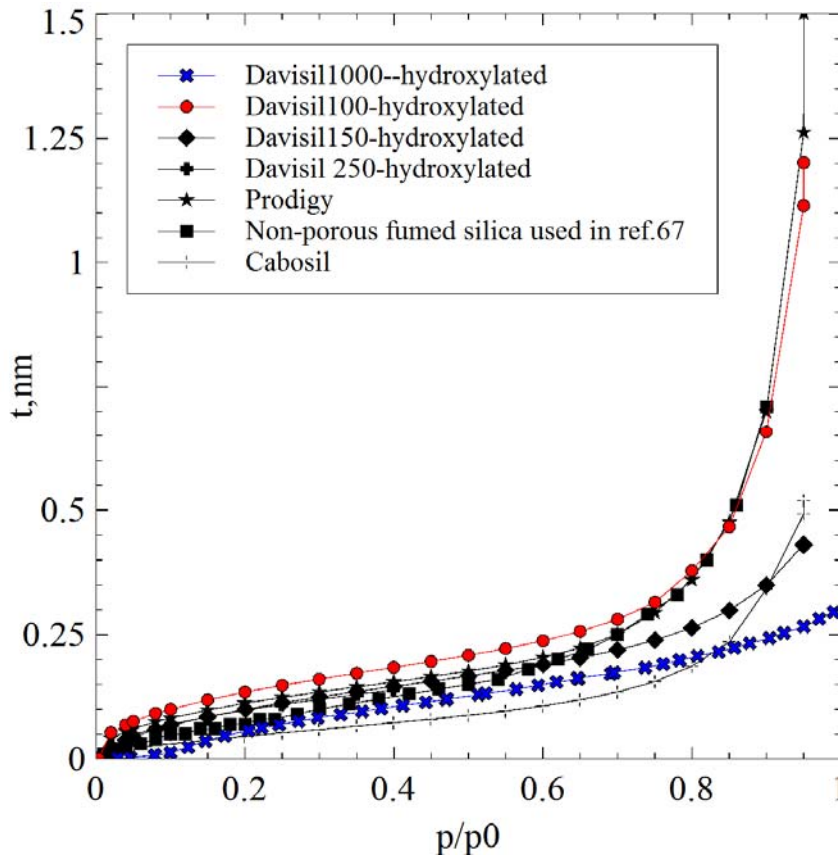
Figure 39. The statistical thickness for water adsorption (t-curves) for hydroxylated silica surfaces. See Table 13 for silanol numbers for all silicas. For non-porous fumed silica used in ref.67 see ref.[67].

100
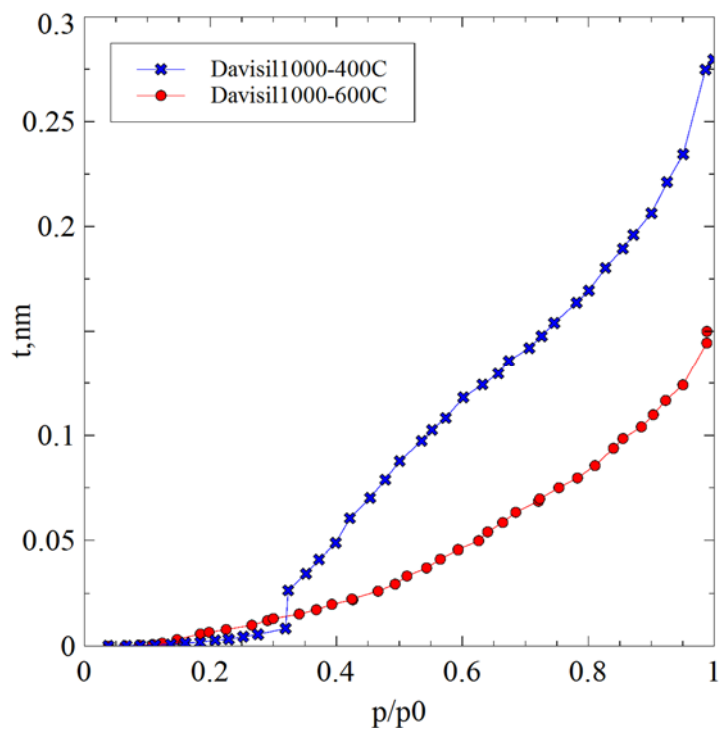
Figure 40. The statistical thickness for water adsorption (t-curves) for partially dehydroxylated silica surfaces. See Table 14 for silanol numbers.
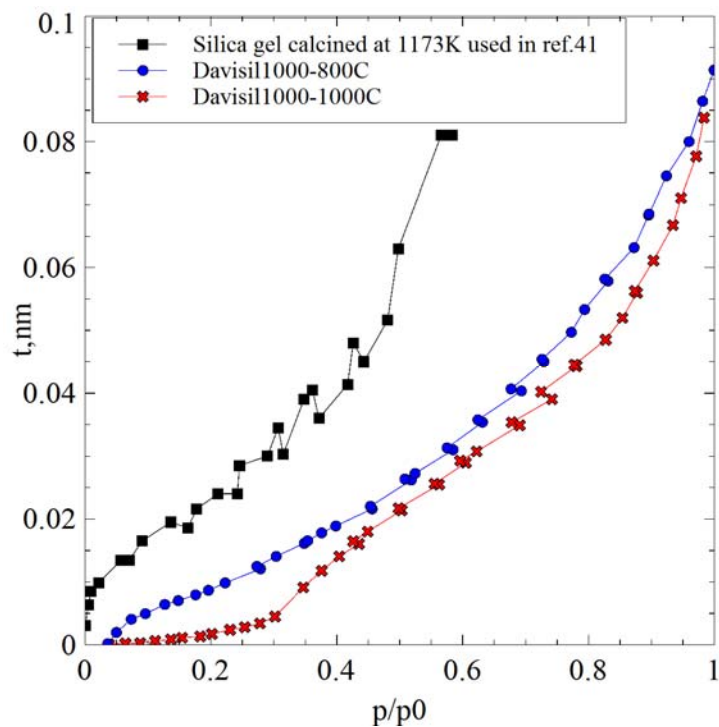
Figure 41. The statistical thickness for water adsorption (t-curves) for fully dehydroxylated silica surfaces. See Table 14 for silanol numbers. For silica gel calcined at 1173K used in ref.41 see ref.[41].

To generate the water t-curves for hydrophobic silica surfaces, the reference samples were obtained by the reaction of hydroxylated Davisil 1000 with (N,N-dimethylamino)-trimethylsilane (TMS). By varying the reaction time, surfaces ranging in the concentration of TMS groups were prepared. As assessed by chemical analysis (%C), the TMS grafting densities were 0.75, 1.45, and 2.81 TMS/nm^2 for 1 min, 15 min, and 72 h reaction time respectively. Using the cross-sectional area of TMS groups[84] at 0.35 nm^2, these values corresponded to ~25, 50 and 100% surface coverage by TMS (by area). The water t-curve data was fitted with the following equations:

$$t^{0.25\,TMS}[nm] = 0.129 * \frac{p}{p_0} + 0.048 \qquad \textbf{(3-16)}$$

$$t^{0.5\,TMS}[nm] = 0.037 * \frac{p}{p_0} + 0.032 \qquad \textbf{(3-17)}$$

$$t^{TMS}[nm] = 0.027 * \frac{p}{p_0} + 0.008. \qquad \textbf{(3-18)}$$

We noted that for silicas modified with hydrophobic TMS groups, the large fraction of silanols was still present on the surface. For the surfaces with 25, 50%, and 100% TMS coverages (by area), respectively ~85, ~71%, and 44% of the original silanols remained intact. These residual silanols are accessible to water molecules and serve as primary adsorption centers on the TMS-modified silicas[88-91].

3.3.7 Water adsorbed per silanol group

To compare the water adsorption on surfaces of different composition (different silanol numbers) the amount of water adsorbed per silanol group was calculated and plotted as a function of relative pressure for silicas of different degree of hydroxylation (Figure 42). More specifically to relate the average number of water molecules adsorbed to the number of surface silanols, the

adsorbed amounts of water were plotted vs. the number of OH groups present on the surface. Figure 43 shows these plots for two relative water pressures 0.2 and 0.5 p/p_o respectively. Figure 43 also includes the data from works[8, 41, 67], which was recalculated using the reported silanol numbers. The results in Figure 43 showed that for hydroxylated, dehydroxylated, and hydrophobic silicas, the amount of adsorbed water was directly proportional to the number of OH groups present on the surface. This was remarkable as these plots suggested a simple, approximately linear relationship between the water adsorption and the silanol number regardless of the nature of the surface. At relative pressure 0.2 the ratio between the adsorbed water molecules and the silanol groups was ~1:2, while at 0.5 this ratio was close to 1:1, in agreement with the earlier works[8, 67-68]. We point out that these ratios do not reflect the true adsorption stoichiometry, which is more complicated according to IR and modeling. These ratios, however, may be useful as empirical rules to evaluate the number of silanols from the water adsorption data or, alternatively, to predict the amount of water adsorption for a surface with known silanol number. It is important to point out, however, that the approximately linear relationship between the amount of water adsorbed and the number of silanols is valid only up to a certain relative pressure, perhaps up to ~0.5 p/p_o or so. At higher relative pressures, when the adsorption of water increasingly occur on the previously adsorbed molecules and involve cooperative hydrogen bonding and clustering, the adsorption become influenced more by the local environment and spacing between the growing water clusters than by the number of primary adsorption centers lying underneath (silanols). The difference in the adsorption behavior at high relative pressures was clearly seen upon comparison of the water isotherms for TMS-modified silicas. For silicas with low TMS coverage (<25% by area), the adsorption progressively increased with the relative pressure leading to a multilayer adsorption and, eventually, capillary condensation of water in pores. For more hydrophobic

surfaces (>50% TMS by area), no capillary condensation was observed and the adsorption at high relative pressures was nearly constant indicating that growth of water clusters was inhibited on extended hydrophobic surfaces. Considering surface hydrophobicity, it was remarkable however that the shape of the initial part of the isotherm was convex (Figure 36) indicating positive interactions between water and the surface, thereby suggesting the presence of the hydrophilic adsorption centers albeit at a small amount. We believed that the adsorption centers were residual silanol groups. The water adsorption data suggested that the residual silanols were not fully screened by the TMS groups and were available to water vapors.
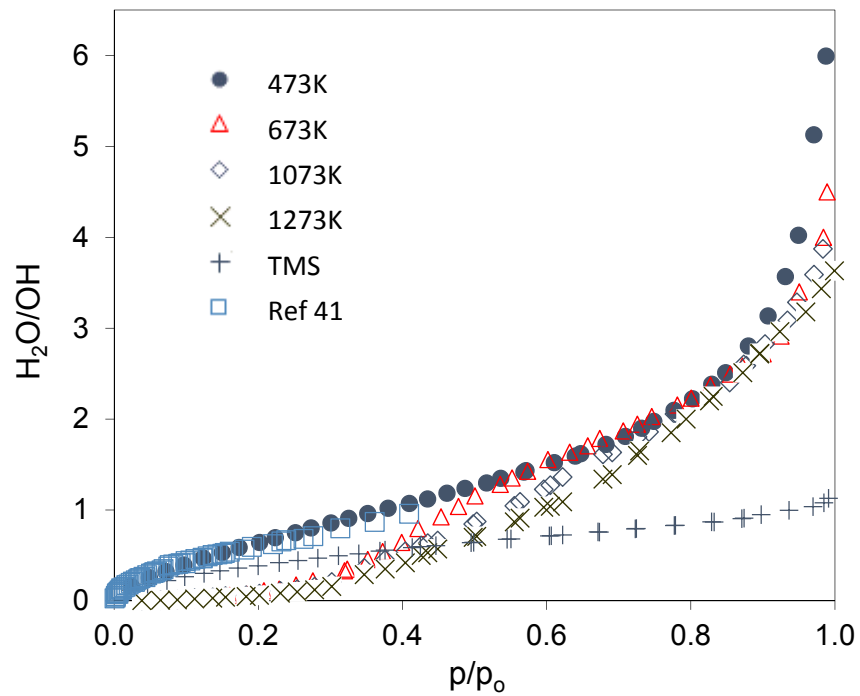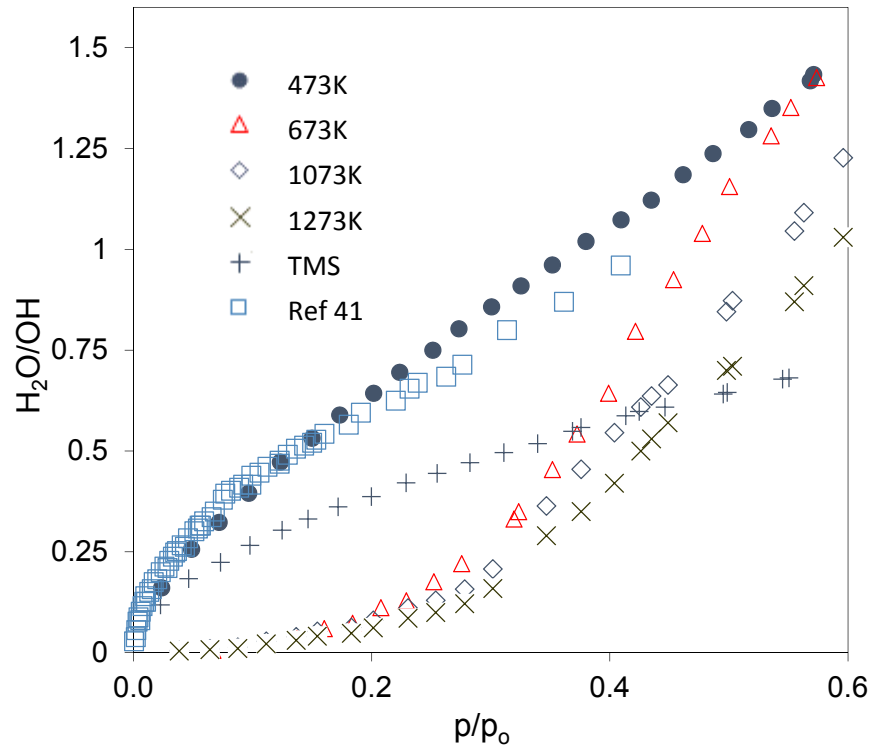
Figure 42. Water adsorption per silanol group for silicas of different degree of hydroxylation. Silica: large pore Davisil 1000, temperature of calcination is shown in the label. Top – initial parts, bottom – full isotherms.

105
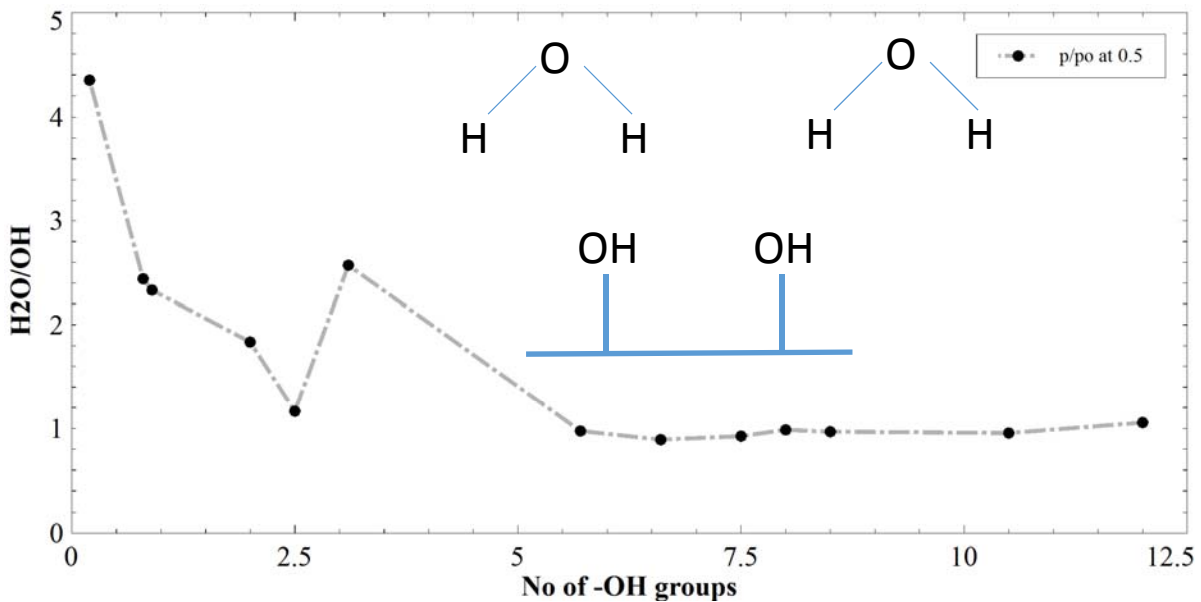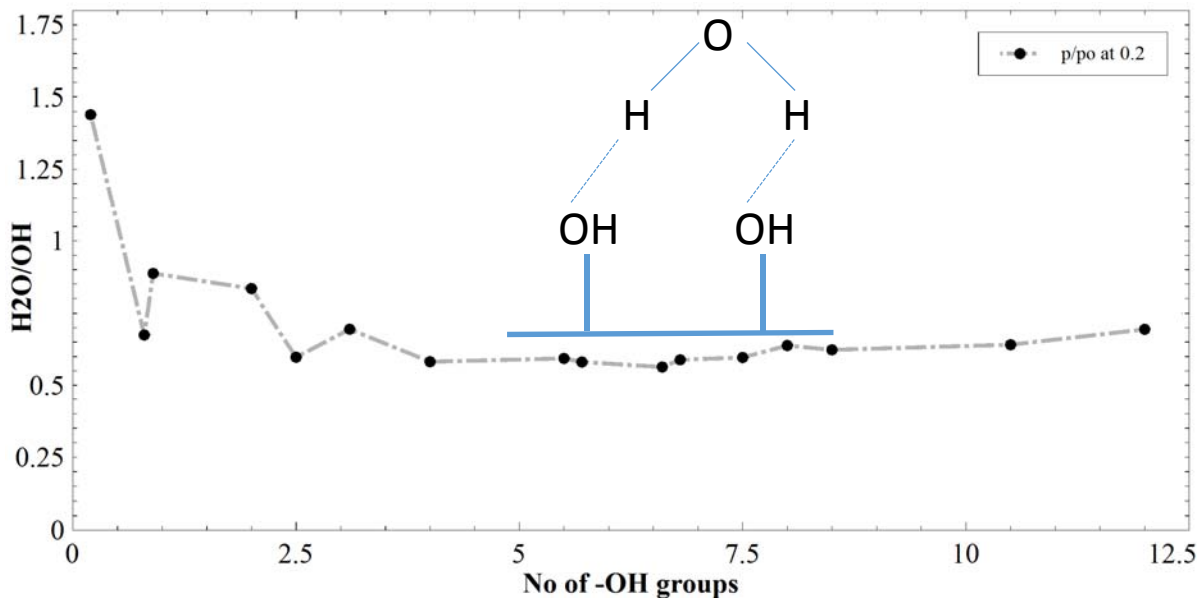
Figure 43. Water adsorption per silanol group as a function of number of silanols for silicas of different degree of hydroxylation. Top – at p/p$_o$= 0.2, bottom – at p/p$_o$= 0.5

106

3.4 Conclusions

In this work, we employed the combined vapor adsorption study using nitrogen (77K) and water (293K) isotherms to evaluate the water contact angles for a series of ordered mesoporous silicas, including MCM-41 and SBA-15, as well as for conventional silica gels. Specifically, the water isotherms were used to determine the most probable Kelvin radius of menisci $(r_m(H_2O))$ during evaporation of liquid water from pores. Then, $r_m(H_2O)$ was compared with the true radius of pores as assessed from nitrogen isotherms $(r_p(N_2))$. For incomplete wetting, the radius of meniscus, radius of pore, and statistical film thickness $t(H_2O)$ were related through the known equation: $r_p(N_2) - t(H_2O) = r_m(H_2O) \cdot cos\theta$, which was used to calculate the water contact angles ($\theta>0$) in pores.

As it was anticipated, the results obtained showed that the silica pore contact angles were strongly influenced by the number of the surface silanol groups and, therefore, by the thermal and hydration treatments of silicas. Freshly made MCM-41 and SBA-15 silicas calcined at 550°C (standard treatment to remove surfactant from the pores) demonstrated partly dehydroxylated, moderately hydrophobic surfaces with the water contact angles θ ~30-40°. Exposure of these silicas to water vapors at room temperature gradually restored the hydroxyl coverage and reduced the water contact angles down to ~15-20°. However, silicas with fully hydrophilic surfaces wettable by water were obtained only after the hydroxylation, the hydrothermal treatment by liquid water at 100°C (373K) for 24 h. Thus hydroxylated silicas showed pore surfaces with water contact angles θ ~0-12°. The changes in the pore structure of SBA-15 caused by liquid water were attributed to the dissolution/ redistribution of silica resulting in smoothening the pore walls and reduction of the micropores[74]. Depending on the preparation conditions used for the SBA-15 synthesis[74], the reflux in water for 4 h showed ~5-20% decrease in the pore volume and ~10-50%

decrease in the surface area compared to bare SBA-15, in good agreement with the results reported here.

Along with the thermal treatment, chemical substitution of silanols was a powerful method to control the pore wetting. For example, the reactions of SBA-15 with trimethyl-(N,N-dimethylamino)-silane produced a series of silicas with the increasing pore hydrophobicity as characterized by the water contact angles 26, 31, 41, and 62° for 10, 35, 50, and 60% of the TMS surface coverage respectively.

The proposed method of the contact angles determination relies on the statistical film thickness (t-curve) of the adsorbed water. We noted that the t-curves for water adsorption reported in the literature varied significantly and, especially for dehydroxylated and hydrophobic surfaces, were scarce or unknown. To address this issue, the water t-curves were measured for a series of model wide-pore silicas with known silanol content covering the wide range of silanol coverage. The raw data and the equations for the t-curves on hydroxylated, dehydroxylated, and hydrophobic TMS silicas were reported providing the reference data necessary for the quantitative analysis of water adsorption.

Chapter 4: Fluorinated Metal Phthalocyanine Encapsulated in Metal Oxides

4.1 Introduction

Phthalocyanines (Pcs) are an interesting class of molecules due to their remarkable electronic and physicochemical characteristics, their ability to be organized into different condensed systems, and their numerous applications as a functional material (dyes, gas sensors, catalysts, optoelectronic devices)[92-95]. Phthalocyanines are planar aromatic macrocycles constituted by four isoindole units linked together through azo nitrogen atoms. Pcs are intensely colored blue-green heterocyclic compounds and are structurally similar to porphyrins and their useful properties are attributed to their efficient electron transfer abilities. Pcs have been extensively studied in industry and academia, in a variety of applications ranging from conventional dyes to catalysis, coatings for read/write CD-ROM's and as anti-cancer agents[92-93, 96]. The majority of applications use the metal-substituted form of the Pc molecule. Figure 44 shows the structure of metal free and metallo phthalocyanine (MPc) as well as the numbering scheme traditionally used for their nomenclature[97]. The hydrogen atoms of the central cavity can be replaced by more than 70 different elements, generating the metallophthalocyanines (MPcs)[98].
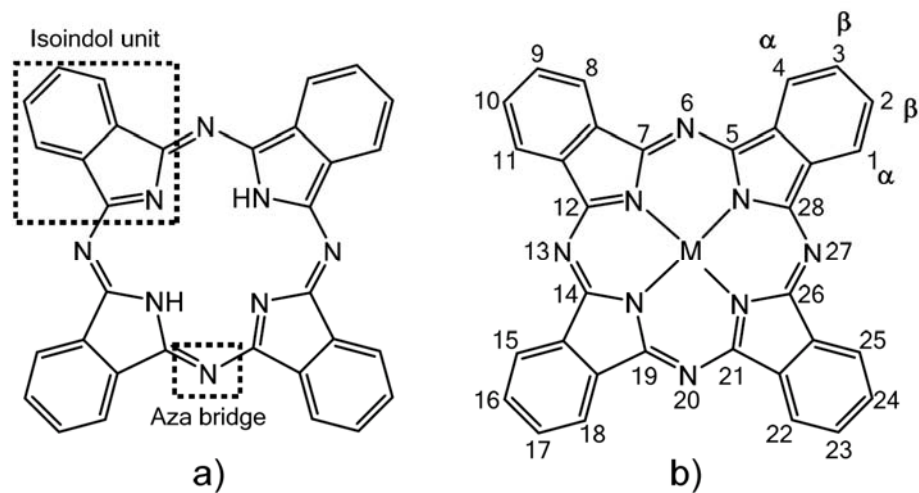
Figure 44. a) Free-base phthalocyanine b) metallophthalocyanine. Adapted from ref.[97].

MPcs are very attractive as catalysts due to their structural analogy with porphyrin complexes (catalytic properties of metalloporphyrins has been well studied) and due to the convenience of MPcs in terms of cost and direct preparation on a large scale. Porphyrin complexes are widely encountered in nature in the active sites of enzymes responsible for catalytic aerobic oxidations, reduction and transport of dioxygen, and destruction of peroxides. Figure 45 compares porphyrin and phthalocyanine complexes highlighting the structural analogy[92].

Synthetic porphyrin complexes

Costly preparation not available in large amounts

Too expensive for large scale industrial applications
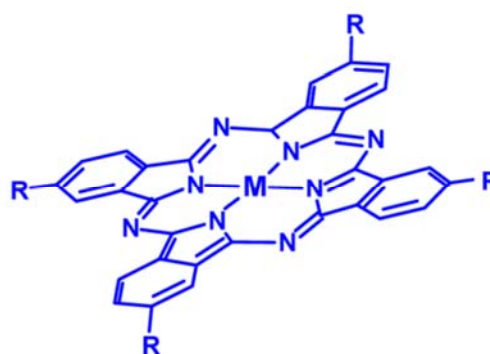
Phthalocyanine metal complexes

Readily accessible in a large scale (worldwide annual production > 80000 t), economical, stable

Viable candidates for industrial catalysis

Figure 45. Structure of porphyrin and phthalocyanine complexes. Adapted from ref.[92].

The catalytic properties of MPcs depend on the metal and complex structures and can be further tuned by appropriate structural modifications[92]. Major modifications of the Pc structure performed by changing the central metal atom and/or the axial coordination ligands and peripheral modifications. Figure 46 illustrates the numbering scheme widely used to demonstrate substituents positions on MPc.
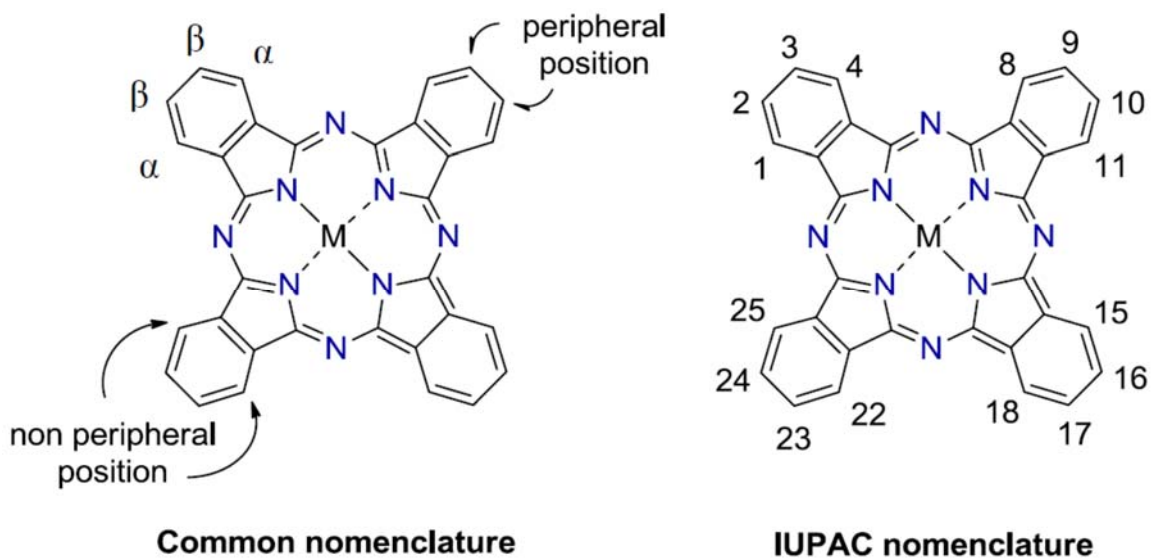
Figure 46. Numbering scheme and labeling of outer-ring positions (α, β) of the phthalocyanine molecule core. Note the 16 C-H bonds present in an unsubstituted molecule. Adapted from ref.[94, 98].

All 16 sites (16 C-H bonds, 8α and 8β) in a Pc have been subjected to a variety of modifications resulting in Pcs with dramatically improved physical and chemical properties. Peripheral substituents play a key role in the catalytic chemistry of MPcs and hence peripheral substituents have been used to tune the steric and electronic features of phthalocyanines, to yield both electron-rich and electron-poor species, the latter including the important class of halogenated phthalocyanines[95]. Additionally, the substituents play a critical role in the solubility of the MPcs. Addition of fluorinated substituents into the MPc molecule increases their stability to nucleophilic, electrophilic, and radical attacks. In addition to $MPcF_{16}$ (M = Ru,[99] Fe,[100] Co, and Cu,[101]), all-fluorinated phthalocyanines bearing perfluoroalkyl groups such as $ZnPcF_8(i-C_3F_7)_8$[95] and $CoPcF_8(i-C_3F_7)_8$[102] have been prepared and reported[92]. A change in the central metal will impact the catalytic activity and electronic, spectroscopic, and physical properties of the MPcs. The most interesting and potential MPcs for catalysis[92] contain Fe, Co, Cu, Ru, Mn, Cr, Al, and Zn. A wide

range of several transformations including reduction, preparation of nitrogen-containing compounds, and various C−C bond formation reactions can be efficiently catalyzed by MPcs. The catalytic properties of MPcs can be used in large-scale processes for the preparation of bulk chemicals and synthesis of elaborated fine chemicals[92]. The focus of Dr.Gorun and his collaborators' work[94, 98] has been the replacement of outer-ring hydrogens with fluorine and i-C$_3$F$_7$ groups to increase the relative stability and catalytic activity of MPcs.

Homogeneous catalysts have some attractive properties, such as high selectivity and accessibility to all catalytically active sites. However, the use of homogeneous catalysts is being challenged because of inherent problems, such as corrosion, toxicity, difficulty in catalyst handling and separation from the reaction system, high cost, and the creation of solid waste. A thorough review of homogenous and heterogeneous catalytic reactions using various MPcs has been published by Sorokin[92]. In general, unsubstituted MPcs have been often used as catalysts (homogeneous) in a variety of reactions. Due to their poor solubility in common organic solvents, the solubility of these MPcs under reaction conditions has always remained an issue.

One approach is to immobilize the homogeneous catalyst on an insoluble support[92, 103], forming a heterogeneous catalyst. Heterogeneous catalysts are highly preferred due to their easy separation from the reaction mixture and their reuse for successive reactions provided that catalysts retain their catalytic properties[104]. In general organic polymers and inorganic materials are used as supports for the catalyst molecule. However the stability of the support under reaction conditions, non-involvement of the support itself in the reaction, capacity of the support to introduce functionality for covalent anchoring, availability and cost of the support are various considerations. Porous materials with high surface area e.g., mesoporous silicas generally provide a good catalyst loading and a possibility to use confinement effects i.e entrapment of the catalyst molecule inside

the support. The distribution of the active sites (MPc) on the surface of the adsorbent (solid support), accessibility to the active site and the state of the adsorbent-MPc complex are heavily influenced by the method or procedure of preparation of these supported catalysts.

In the thesis completed by Graffius[98] a systematic study of the solution adsorption was performed on several substrates, including : (1) Zinc phthalocyanines with an increasingly fluorinated periphery and electron deficiency, and (2) $F_{64}PcM$ where the central metal was changed from Zn to Cu, Co, Ru, Fe, and VO. Adsorption of each series from acetone and methylene chloride was compared on several unique adsorbents. Solution adsorption of phthalocyanines was demonstrated as an effective means of producing uniform catalytically active solid surfaces. The end-goal of the research performed by Graffius[98] work was to obtain stable phthalocyanine thin films for use as recyclable, solid-supported heterogeneous catalysts.

In this effort, we have undertaken a systematic study to explore the possibility of preparing a supported catalyst material i.e loading fluorinated metal phthalocyanines onto metal oxide surfaces by two other techniques in addition to solution adsorption demonstrated by Graffius[98]. Techniques or procedures that have been used to immobilize MPcs include: i) physical adsorption (from solution) onto metal oxide surface, ii) deposition by pore filling and encapsulation and iii) mesopore entrapment or confinement. The MPcs are loaded on to metal oxides with an aim to: a) maximize the surface area of the Pcs by distributing it over the support, b) immobilize the Pcs so that they do not leach into the solution environment, c) improve the thermal stability of the Pcs and d) attempt to achieve single-site catalysis. All the immobilization techniques were carried out with $F_{64}PcZn$ as the model MPc, acetone as the immobilization solvent and silica or alumina as adsorbents (solid support).

An understanding of gas adsorption mechanisms on metal phthalocyanines (MPcs)[105] is essential for their practical application in biological processes, gas sensing, and catalysis. In this work, the surface characteristics were probed by performing nitrogen and water adsorption on the free-form MPcs (without immobilization on solid support) and characterization of their physical properties. Additionally probing into surface characteristics of MPcs facilitate the understanding of these complexes interact with or adsorb onto metal oxide pores.

4.2 Experimental

4.2.1 Chemicals

All solvents and chemicals for the synthesis of the phthalocyanines were purchased from Thermo Fisher Scientific (Waltham, MA). Commercially available phthalocyanines were purchased from Sigma-Aldrich (St. Louis, MO).

4.2.2 Metal oxides

Davisil 150 Silica (Pore Diameter: 150Å, Pore Volume: 0.5cc/g) was obtained from Grace (Columbia, MD). The pore structure of Davisil 150 was assessed by nitrogen adsorption (77 K) using a Quantachrome Autosorb-1 analyzer (Boynton Beach, FL, USA). Colloidal alumina (Aluminum oxide, 20% in H_2O, colloidal dispersion) and mesoporous alumina (activated alumina, basic, Pore Diameter: 58Å) were obtained from Alfa Aesar (Tewksbury, MA).

4.2.3 Synthesis of perfluorinated phthalocyanines

Synthesis of the perfluorinated phthalonitrile precursor and phthalocyanines was completed by Erik Carrion from the Gorun research group at Seton Hall using a previously developed procedure (Figure 47) [94, 96, 106]. Briefly, the fluorinated precursor, tetrafluorophthalonitrile, (A) was purchased

from TCI Co., Ltd. Perfluoro (4,5-diisopropyl)phthalonitrile (B) was synthesized from A by nucleophilic substitution as described in the literature[106]. The fluorinated phthalonitriles (A, B) at proper mole ratios were melted with a metal acetate using a microwave at 180 °C to yield a blue-green solid[106-107]. Synthesis using only A yielded $F_{16}PcM$. Synthesis using only B yielded $F_{64}PcM$. Synthesis of fluorinated phthalocyanines using mixed starting materials could yield, in principle, four additional organic scaffolds: $F_{28}PcM$, $F_{40}PcM$ (cis as the major) and $F_{52}PcM$. Chromatographic separation of the products yielded purified blue-green materials. The structure and purity of the material was confirmed by ^{13}C and ^{19}F NMR spectra[107].
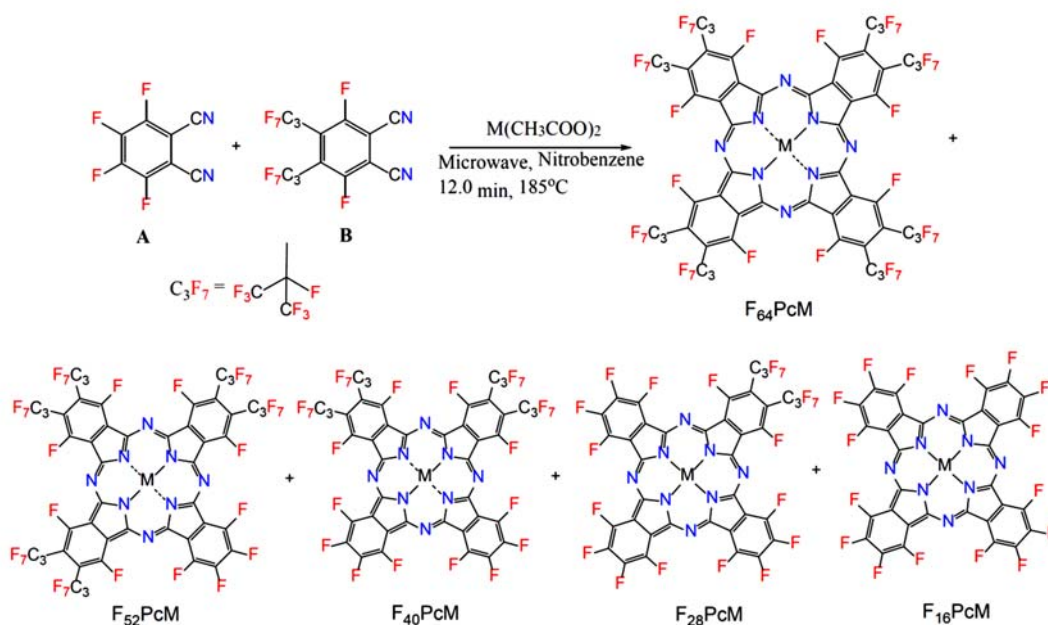
Figure 47. General synthetic scheme for the preparation of fluorinated phthalocyanines. Varying the ratios of phthalonitrile reactants, A and B, preferentially targets production of one of the five products shown. A reaction with only A will produce $F_{16}PcZn$. A reaction with only B will produce $F_{64}PcZn$. Ratios for A to B of 3:1, 1:1, and 1:3 are used for the synthesis of $F_{28}PcZn$, $F_{40}PcZn$, $F_{52}PcZn$, respectively.

In this work, $H_{16}PcZn$, $F_{16}PcZn$ and $F_{64}PcZn$ are the three metal fluorinated phthalocyanines that has been used for all studies.

4.2.4 Deposition by pore filling

The required amount of components (MPcs in the work) are introduced in the volume corresponding to the pore volume of the solid support. This method of deposition is suitable for species which interact weakly with the adsorbent surface and for deposition of quantities exceeding the number of adsorption sites on the surface. For example, one gram of silica (Davisil 150, pore volume: 0.5 cc/g) was weighed into a vial. $F_{64}PcZn$ (0.25 ml) phthalocyanine stock solution (1 mg/mL in acetone) was added slowly and let to sit for 20 minutes. Again another 0.25 ml of $F_{64}PcZn$ phthalocyanine stock solution was added slowly and let to sit for 20 minutes. The sample was dried overnight at 50°C. The amount of stock solution (0.5 mL) added was equivalent to the pore volume of the material. Figure 48 illustrates the method of deposition by pore filling.
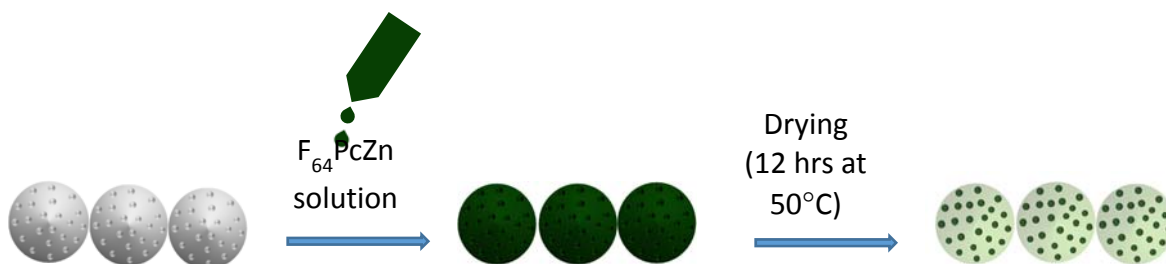
Figure 48. Deposition by pore filling method.

4.2.4.1 Encapsulation procedure

Encapsulated materials can exhibit a higher stability to temperature and solvent compared to non-encapsulated materials. The silica loaded with $F_{64}PcZn$ by pore filling technique above was encapsulated with alumina. A few grams (~0.5 g) of $F_{64}PcZn$ loaded silica was weighed into a vial and 5mL of water (adjusted to pH 4) was added. An aliquot of colloidal alumina (pH = 4) dispersed in water (2mL of colloidal alumina in 5mL of water) was added slowly to the above silica mixture in water. The solution was vortexed and let to sit for at least 20 minutes. Excess alumina was removed (from supernatant) and the mixture was washed several times with water (~20 mL). The

sample was dried at 200°C for 5 hours. The colloidal alumina which is positively charged assembles around the silica particle which is negatively charged due to electrostatic attraction completes the encapsulation procedure. Figure 49 illustrates the procedure of encapsulating $F_{64}PcZn$ deposited silica with colloidal alumina.

Vortex, settle down, removal of excess alumina, wash with water

Drying at 200°C for 5 hours

Colloidal Alumina in water at pH=4

F64PcZn loaded Silica in water adjusted to pH=4

F64PcZn loaded Silica encapsulated with alumina
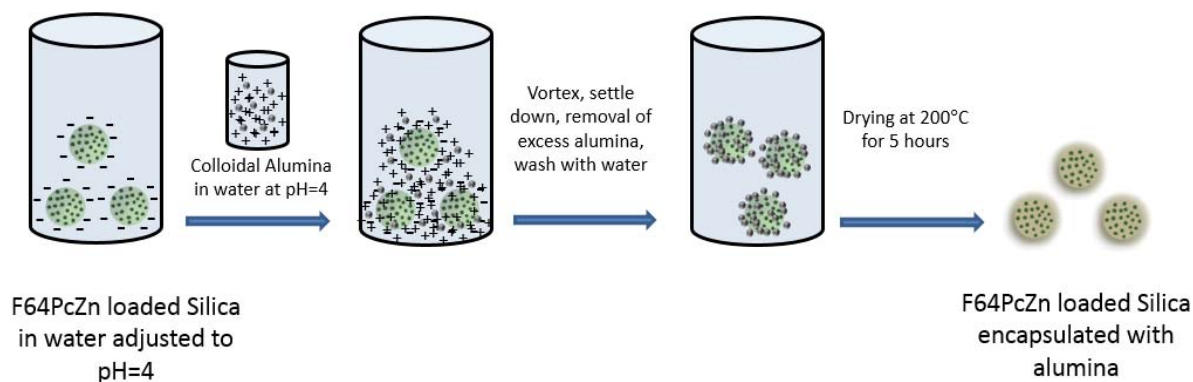
Figure 49. Encapsulation of $F_{64}PcZn$ deposited silica using colloidal alumina.

4.2.5 Mesopore entrapment

In the mesopore entrapment procedure, colloidal alumina was mixed with $F_{64}PcZn$ solution and the alumina was precipitated under certain conditions (high pH using sodium hydroxide) to obtain mesoporous alumina with $F_{64}PcZn$ entrapped inside the mesopores. An aliquot (5 mL) of $F_{64}PcZn$ phthalocyanine stock solution (1mg/mL) was added to an aliquot of colloidal alumina dispersed in water (2mL of colloidal alumina in 5mL/10mL of water). The mixture was mixed well, and vortexed. The pH was adjusted (by adding 200µL of 2M sodium hydroxide) to precipitate the colloidal alumina and mixed well. The sample mixture was centrifuged (4000 rpm for 10 min)

and the clear supernatant was removed. The sample was dried at 70°C for 12 hours. Figure 50 illustrates the synthesis of mesoporous alumina with $F_{64}PcZn$ entrapped.
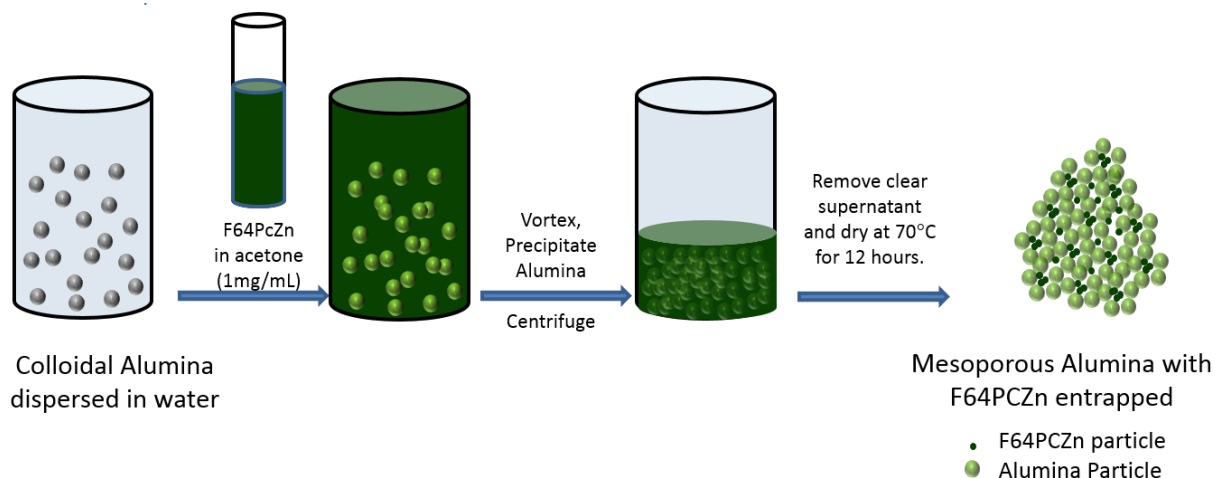
Figure 50. Mesopore entrapment of $F_{64}PcZn$ using alumina.

4.2.6 Solution adsorption

In this technique of deposition by adsorption from excess solution, deposition of active species is less than quantitative and the quantity deposited depends on the solid/liquid ratio. Deposition is slow requiring several hours or days, but allows the distribution of species to be very well controlled. In the previous work by Graffius[98] the Langmuir isotherm model[56] was employed to describe the sorption behavior of phthalocyanines on surfaces. The Langmuir model is based on assumptions that monolayer coverage of adsorbate occurs over homogeneous sites and that a saturation point is reached when no further adsorption can occur[98]. An aliquot of colloidal alumina (2mL) was dispersed in 10mL of water, mixed well and vortexed. pH was adjusted (by adding 200μL of 2M sodium hydroxide) to precipitate the colloidal alumina and mixed well. The sample mixture was centrifuged (4000 rpm for 10 minutes) and the clear supernatant was removed. The

sample was dried at 200°C for 12 hours to obtain bare mesoporous alumina. The obtained mesoporous alumina were immersed fully in phthalocyanine solution (acetone) to facilitate adsorption. Few milligrams (50mg) of mesoporous alumina was weighed into a vial. 4 ml of 1mg/mL of $F_{64}PcZn$ phthalocyanine stock solution was added and let to sit for 2 days. After 2 days, supernatant was removed. The sample was dried overnight at 60°C. UV/Vis analysis samples were collected by decanting to avoid evaporation during a filtration process. The dye concentration was determined on a Varian Cary 300 (Palo Alto, CA) double beam UV/Vis spectrometer by measuring absorbance maximum for the dye. The quantity of adsorption at equilibrium, Γ ($\mu mol/m^2$), was calculated by the equation[98]:

(4-1)

$$\Gamma = \left(\frac{(C_0 - C_e)V}{W}\right) \cdot \frac{1}{S_{BET}}$$

where C_0 and C_e were the liquid phase concentrations of Pc at initial and equilibrium conditions, respectively. V (L) was the volume of the Pc solution and W (g) was the mass of dry sorbent used. S_{BET} (m_2/g) is the surface area of the adsorbent as measured by nitrogen adsorption. Figure 51 illustrates the solution adsorption of $F_{64}PcZn$ on mesoporous alumina.
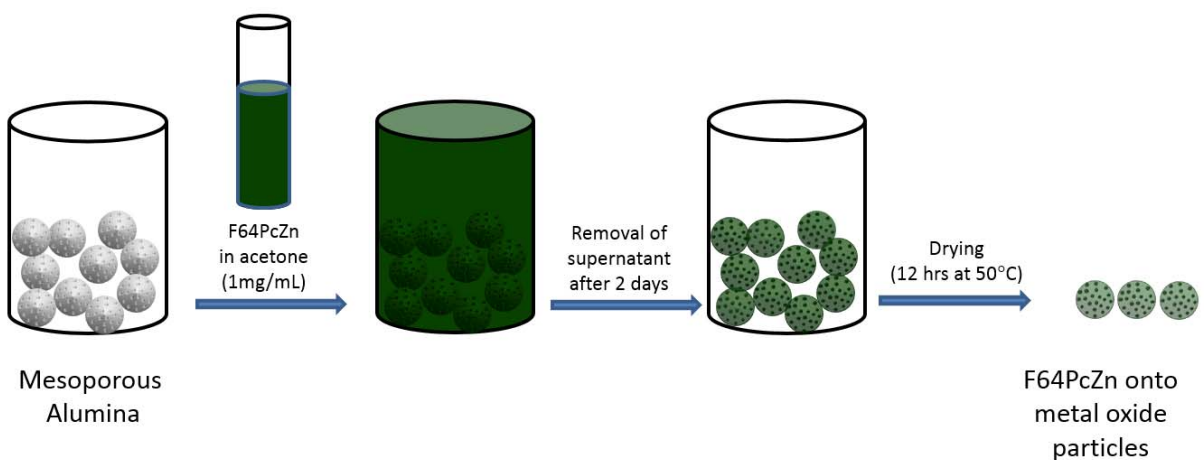
Figure 51. Solution adsorption of $F_{64}PcZn$ on mesoporous alumina

4.2.7 Solid state characterization

Reflectance UV/Vis/NIR of the resulting solids was obtained on a Varian Cary 500 (Palo Alto, CA) UV/Vis/NIR spectrometer fit with a reflectance accessory DRA-CA-5500 (Labsphere, North Sutton, NH, USA). The reflectance data collected in the adsorbed solid state was used to compare the presence or absence of Pc on the solid support and also to qualitatively demonstrate the decrease of Pc during thermal stability studies. Samples were tightly packed into a custom built quartz analysis cell. As we were using large, non-uniform and porous materials, compensation for adsorption and scattering of the signal was required. Kubelka-Munk[108-109] transformations were applied to the reflectance data as follows:

$$f(R) = \frac{(1-R)^2}{2R} = \frac{k}{s} \qquad \textbf{(4-2)}$$

where R is the absolute reflectance of the sampled layer, k is the molar absorption coefficient and s is the scattering coefficient. The SiO_2 materials were more UV/Vis transparent than Al_2O_3, limiting the linear range (Γ) under which the analysis could be used[98].

4.2.8 Calculation of phthalocyanine dimensions and theoretical monolayer coverage[98]

The dimensions of $F_{16}PcZn$ and $F_{64}PcZn$ were calculated using a combination of ACD(Toronto, ON, Canada) and Mercury Software (Cambridge, UK) to obtain the cross-sectional area (ω). From the dimensions, a square/rectangular shape was assumed to obtain Γ_{max} (maximum monolayer adsorption capacity in $\mu mol/m^2$) of a tightly packed monolayer. Due to the generally planar shape of the molecule, the Γ_{max} for densely packed molecules would be quite different for the vertical (edge on) versus the horizontal orientation (face on), as shown in Table 15[98] and Figure 52[98].

Table 15. Cross-sectional area (ω) and theoretical monolayer coverage (Γ_{max}) for densely packed fully symmetrical zinc phthalocyanines: $F_{16}PcZn$ and $F_{64}PcZn$

	Edge On		Face On	
	ω (Å^2/molecule)	Γ_{max} (μmol/m^2)	ω (Å^2/molecule)	Γ_{max} (μmol/m^2)
F$_{16}$PcZn	51	3.26	332	0.500
F$_{64}$PcZn	167	0.994	437	0.381
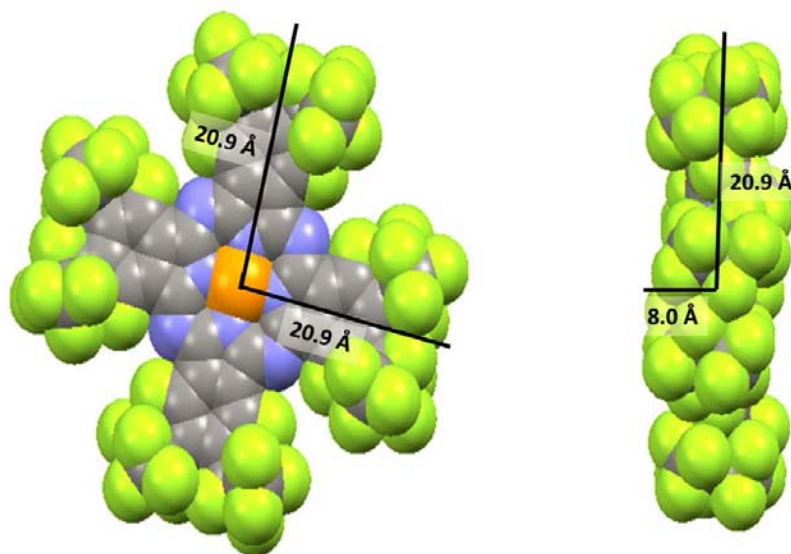
Figure 52. 3D Space-Filling Model of F64PcZn at the 'face on' and 'edge on' orientation, demonstrating the difference in cross-section area at for each possible orientation.

4.2.9 Nitrogen adsorption isotherms

The adsorption-desorption isotherms of nitrogen (77K) were obtained with a Quantachrome Autosorb-1 Analyzer (Boynton Beach, FL, USA) and with a Micromeritics ASAP Analyzer (Norcross, GA, USA). The isotherms were measured over a relative pressure p/p$_o$ range from ~0.005 to 0.995 and, on average, consisted of 80-130 adsorption-desorption points. Prior to the

adsorption measurements, the Pcs were outgassed at 200°C overnight. Specific surface areas were calculated via the BET method using the range of relative pressure from ~0.06 to 0.27 and the value for nitrogen cross-section 0.162 nm^2. The pore size distribution and the average (most probable) pore radius $r_p(N_2)$ was calculated by the BJH method from the desorption branch of the isotherm. Complete wetting of the pores by liquid nitrogen ($\cos \theta = 1$) was assumed. All the calculations were performed using vendor's (Quantachrome Instruments) software. The amount of nitrogen adsorbed (Γ) expressed in µmole/m^2 is converted to number of nitrogen molecules per MPc molecule as per equation (4-3).

$$Number\ of\ adsorbate\ molecules\ per\ MPC\ molecule = (\Gamma * 10^{-6}) * (\omega * 10^{-20}) * N_A$$

(4-3)

where Γ is amount of nitrogen adsorbed in expressed in µmole/m^2, ω is *cross-sectional area* of the MPc molecule in Å^2/molecule and N_A is the Avogadro's constant.

4.2.10 Water adsorption isotherms

The adsorption-desorption isotherms of water (293K) were obtained using a Quantachrome Autosorb-1 Analyzer (Boynton Beach, FL, USA). The isotherms were measured over a relative pressure p/p_o range from ~0.02 to 0.99 and consisted of 78 adsorption-desorption points. Unless specified otherwise, Pcs were outgassed at 100°C overnight. The thickness of the adsorbed films was calculated by equation (3-3). The value for water cross-section 0.105 nm^2. At the temperature of the experiment 20°C, surface tension of water was 72.8 mJ/m^2 and its molar volume is 18.05 cm^3/mol. The contact angles were calculated by equation 2-19 using the most probable values of $r_m(H_2O)$ and $r_p(N_2)$. The amount of water adsorbed (Γ) expressed in µmole/m^2 is converted to number of water molecules per MPc molecule using equation (4-3).

4.2.11 Thermogravimetric Analysis

Thermogravimetric analysis (TGA) was performed using a TA Instruments Thermogravimetric Analyzer operated between room temperature and 1000°C at a heating rate 10°C/min with ambient (air exposure) or a flow of dry nitrogen (20 cm^3/min). Stability of the adsorbed phthalocyanines was assessed by heating materials to set temperatures (200-400°C) and analyzing the TGA weight loss and solid state spectra.

4.3 Results and Discussions

The Zn containing Pcs have been utilized widely in developing electro and photo catalysts, thin films, infrared sensors, photovoltaic cells, light-emitting diodes, and field-effect transistors. The planar Pcs are known to aggregate through π−π interactions, there by hindering solubility and accessibility to the central metal ion which is believed to be important for catalytic activity.

As demonstrated in the work by Patel[94] and references there in the new class of perfluorometalphthalocyanines ($F_{64}PcZn$) exhibit enhanced solubility and favorable electronic structure over planar Pcs. The replacement of sixteen aromatic C-H bonds of planar $H_{16}Pc$ by aromatic C-F bonds ($F_{16}Pc$) enhances the thermal stability of Pcs, but did not improve the chemical stability due to nucleophilic attack[94]. In the research by Patel[94] the aggregation propensity and chemical stability issues of the thermally stable $F_{16}Pc$ have been eliminated via replacement of eight peripheral aromatic C-F substituents with bulky aliphatic *iso* perfluoro groups (i-C_3F_7) resulting in $F_{64}Pc$ class. In the work by Graffius[98], the solution adsorption and thermal stability of phthalocyanines: $F_{16}PcZn$ and $F_{64}PcZn$ in addition to other series of MPcs was studied on a variety of surfaces using acetone and methylene chloride as solvent. Graffius[98] reported strong, irreversible adsorption of these molecules on the surface of Al_2O_3 and aminated silicas. Graffius[98] also indicated that adsorption was dominated by Lewis acid-base interactions between the electron

deficient phthalocyanine metal center and basic moieties on these surfaces. Graffius[98] proposed a mechanism in which the phthalocyanine adsorption occurred face-down by axial coordination of the electron deficient central metal to the electron donating surfaces. To facilitate the use of MPcs in the field of catalysis immobilization of MPcs onto solid support is very crucial and the choice of solid support, solvent and method of immobilization will decide the surface coverage. Based on the report by Graffius[98] alumina is selected as one choice of adsorbent to immobilize MPcs using various techniques. Even though aminated silica showed strong irreversible adsorption in the work by Graffius[98], degradation (at ~150- 200°C) of the solid support (aminated silica) was observed during our preliminary thermal stability experiments and hence aminated silica was not further pursued as an adsorbent of choice. Even though acetone would coordinate with the Pc resulting in steric hindrance and in direct competition to the adsorption of Pcs to the adsorbent surface, acetone was preferred over methylene chloride due to the higher solubility (5-10 times) of fluorinated Zinc Pcs in acetone. Graffius[98] reported that based upon the surface concentration near to that of a monolayer and evidence of edge-to-edge packing, that the $F_{64}PcZn$ adsorbed as a uniform, closely packed monolayer oriented face-on. Hence as a model MPc, $F_{64}PcZn$ is used in the immobilization experiments. The success of a heterogeneous catalyst (MPcs immobilized on solid support through various techniques) is evaluated by surface coverage, thermal stability, solvent stability (minimal or no leaching into solvent) and catalytic activity.

4.3.1 Surface coverage through various immobilization procedures

Table 16 lists a typical monolayer surface coverage ($\mu mol/m^2$) of fluorinated zinc phthalocyanine ($F_{64}PcZn$) on metal oxide surfaces obtained using the three techniques used in this work. The material obtained using these techniques were tested for improved thermal stability and solvent stability (stability to leaching in organic solvents) as discussed in following sections.

Solution adsorption on mesoporous alumina provided the highest surface coverage, however there is poor solvent stability for the material obtained using this approach i.e the Pcs leach back into acetone almost immediately. Even though the mesopore entrapment technique did not offer any improved thermal stability, the solvent stability is much higher compared to the other two approaches. Deposition by pore filling followed by encapsulation offered the best improved thermal stability for few hours at 300C°.

Table 16. Surface coverage of final material obtained by various immobilization techniques. For monolayer coverage of $F_{64}PcZn$ (Face On) cross sectional area is 437 $Å^2$/molecule i.e 0.381 $\mu mol/m^2$

Technique and Metal oxide	Surface Coverage, $\mu mol/m^2$
Adsorption by Pore filling on Silica	0.01
Mesopore (Alumina) Entrapment	0.01
Solution adsorption on mesoporous alumina	0.17

4.3.2 Solid state UV spectra demonstrating mesopore entrapment

The presence or absence of the $F_{64}PcZn$ within the mesopore structure of alumina is verified by the solid state UV reflectance spectra as shown in Figure 53. When the colloidal alumina precipitates and aggregates together to form larger particles, the phthalocyanine molecules gets entrapped resulting in mesoporous alumina with entrapped MPcs. General broadening and splitting of the Q band (600- 800 nm region) possibly indicates evidence of multilayer formation and aggregation[98].

Additionally MPcs entrapped in mesoporous alumina exhibited catalytic activity. Figure 54 show three samples of mesoporous alumina with varying surface coverage of $F_{64}PcZn$ showing catalytic activity during photo degradation studies. In general the catalytic activity is very low,

however the maximum obtainable surface coverage for this material is only 0.008 $\mu mol/m^2$ which is only 2 % of the monolayer coverage (face on orientation). The true catalytic activity can be understood only with the materials that has improved surface coverage. The challenges in obtaining higher surface coverage necessitates the study of bare (i.e not loaded on any solid support) MPcs and use that information to understand how these MPc interact with metal oxide pores.
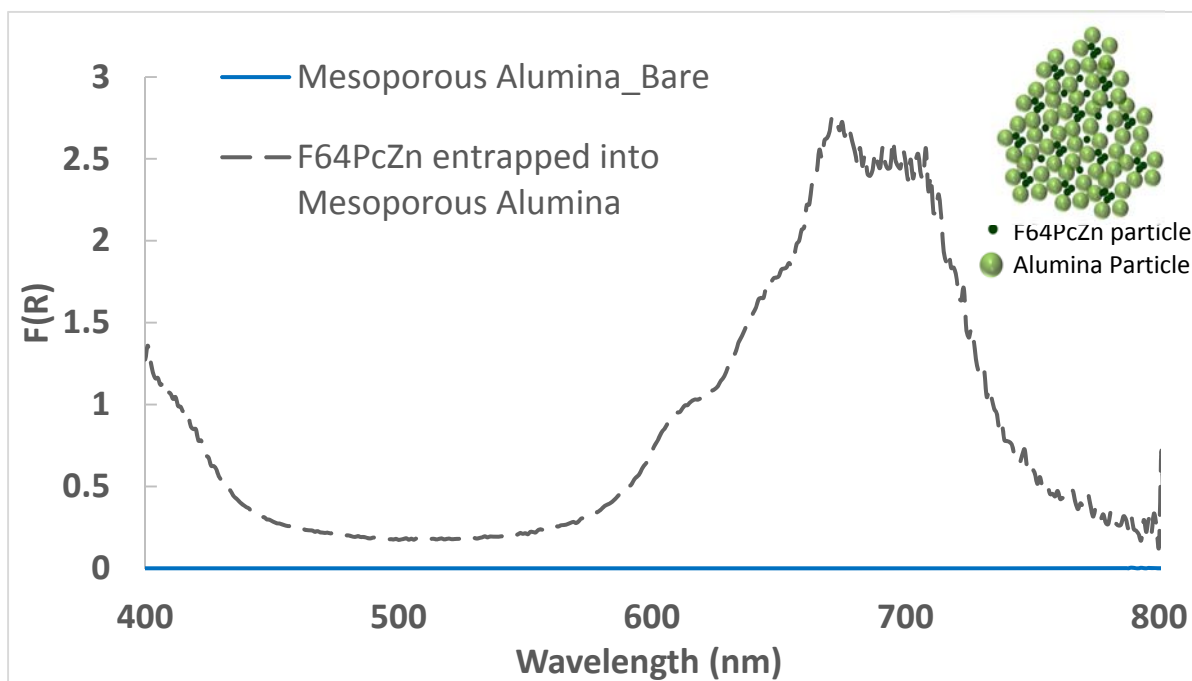
Figure 53. Comparison of the reflectance spectra for the entrapment of F₆₄PcZn inside mesoporous alumina and bare alumina (no F₆₄PcZn)
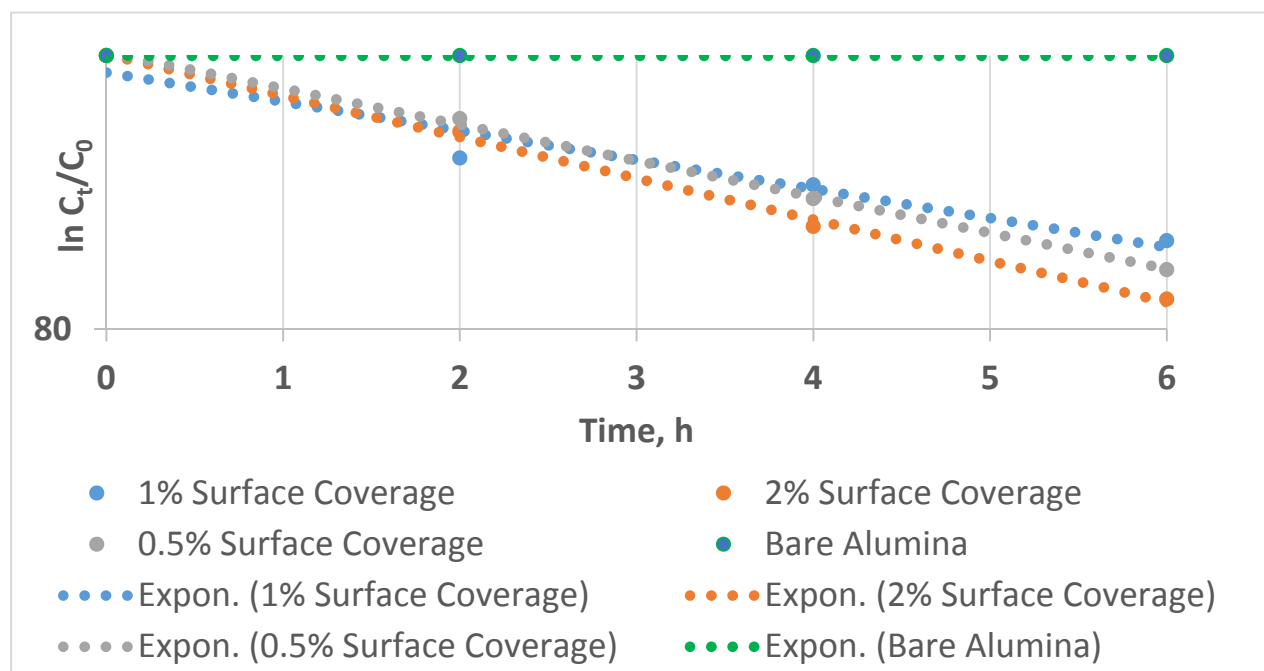
Figure 54. Mesoporous alumina with entrapped phthalocyanines showing catalytic activity

4.3.3 Encapsulation as a means to improve thermal stability

Deposition by pore filling technique alone did not improve thermal and solvent stability. However encapsulation of the material obtained by pore filling led to a final material with improved thermal stability. The $F_{64}PcZn$ loaded on to silica and encapsulated with colloidal alumina was stable at 300°C for at least 5 hours while the non-encapsulated material lost all the MPc when exposed to 300°C as shown in Figure 55. The resulting material possesses improved solvent stability, i.e leached into acetone at a slower rate as the compared with the material without encapsulation. The interaction of the MPcs with the metal oxide surfaces needs to be explored to understand the reason for low surface coverage and this in requires an understanding of how these bare MPcs interact or aggregate or stack.

.
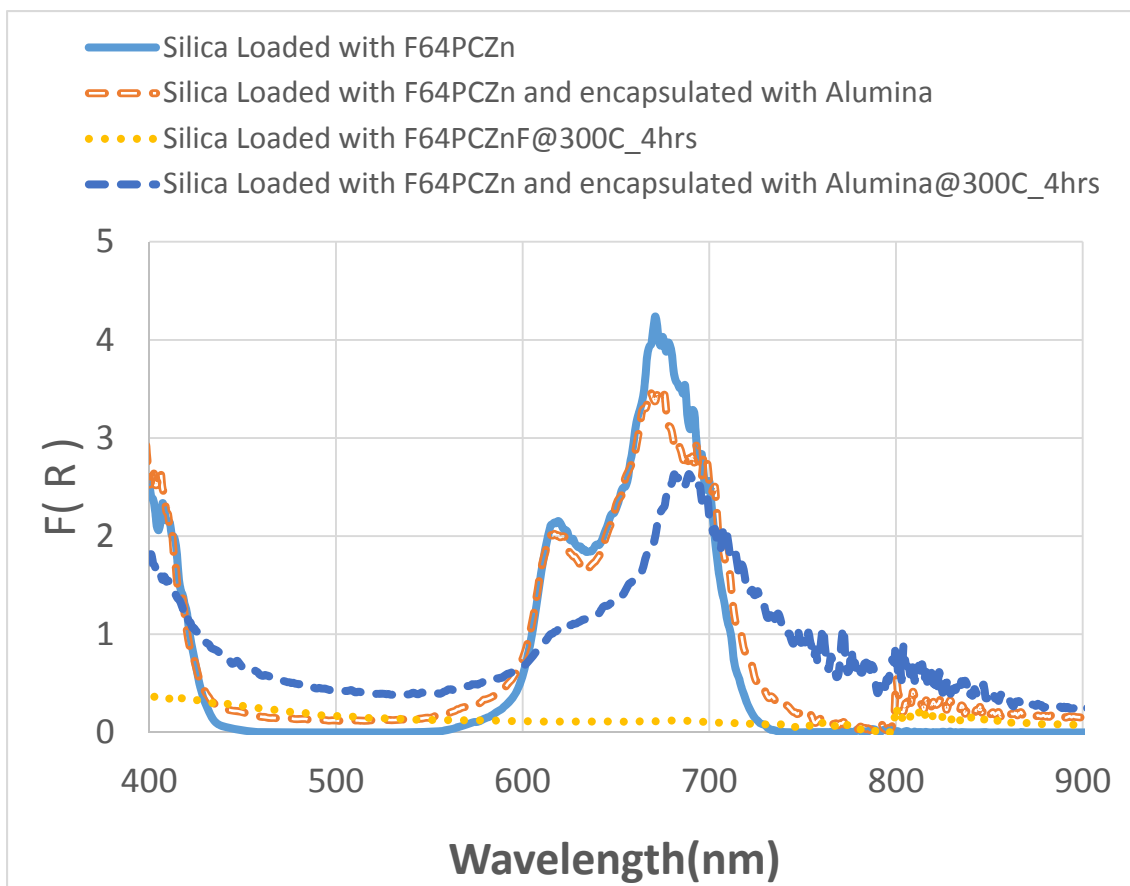
Figure 55. Comparison of the reflected spectra alumina encapsulated F₆₄PcZn (deposited on silica) and non-encapsulated F₆₄PcZn (deposited on silica)

4.3.4 Adsorption measurements on bare fluorinated phthalocyanines

The term bare Pcs used in the following discussion refers to fluorinated Zn Pcs that are not immobilized on any adsorbents. The process of identifying a suitable adsorbent and a suitable immobilization technique to obtain MPc based heterogeneous catalyst support. This method was challenged by the behavior of Pcs with regards to self-aggregation and Pc interaction with metal oxide surfaces. To understand this behavior we measured the surface characteristics or properties of these bare Pcs (H_{16}PcZn, F_{16}PcZn and F_{64}PcZn) by studying a) nitrogen adsorption[110] to measure surface area and size of aggregates. b) water adsorption to understand the hydrophobicity of these Pcs and their possible behavior when exposed reaction conditions in aqueous environment.

128

4.3.4.1 Nitrogen adsorption measurements

The bare Pcs (H_{16}PcZn, F_{16}PcZn and F_{64}PcZn) presented isotherms of the same type as assessed by nitrogen. However, the surface area showed a decrease with an increase of the fluorination. Figure 56 shows the nitrogen adsorption-desorption data on the three bare Pcs. Table 17 shows the structural parameters for the three Pcs obtained using nitrogen adsorption measurements. The BET-nitrogen surface areas are in the range 16.9–40.8 m^2/g, the lowest area being obtained with the F_{64}PcZn and the highest area with H_{16}PcZn. All the nitrogen isotherms exhibit some level of hysteresis down to low pressure, the low pressure hysteresis especially being pronounced with F_{64}PcZn (low pressure hysteresis is higher for F_{64}PcZn and lower for H_{16}PcZn). Irrespective of the presence of hysteresis, all the nitrogen isotherms can be classified as Type II. The presence of low pressure hysteresis in the fluorinated Pcs can be associated with formation of some type of aggregates or stacking. The maximum intermolecular distance between any two Pc molecule in Å (Table 17) as calculated from the theoretical 3D space filling model with face on orientation is not significantly different from the non-fluorinated and fluorinated Pcs (relative difference is only between 2 to 17%). However the diameter of a Pc molecule (aggregate) as determined from the calculation using experimental nitrogen adsorption data is significantly different for the non-fluorinated and fluorinated Pcs (relative difference is between 39 to 109%). This suggests that the Pcs actually exists as aggregates in bulk and not as a single molecule and this aggregation will eventually impact the surface properties of these Pcs i.e adsorption of species on to Pcs and also adsorption of Pcs on to an adsorbent surface. This comparison of existence of these Pcs as a single molecule *vs* aggregate is illustrated as a cartoon in Figure 57.
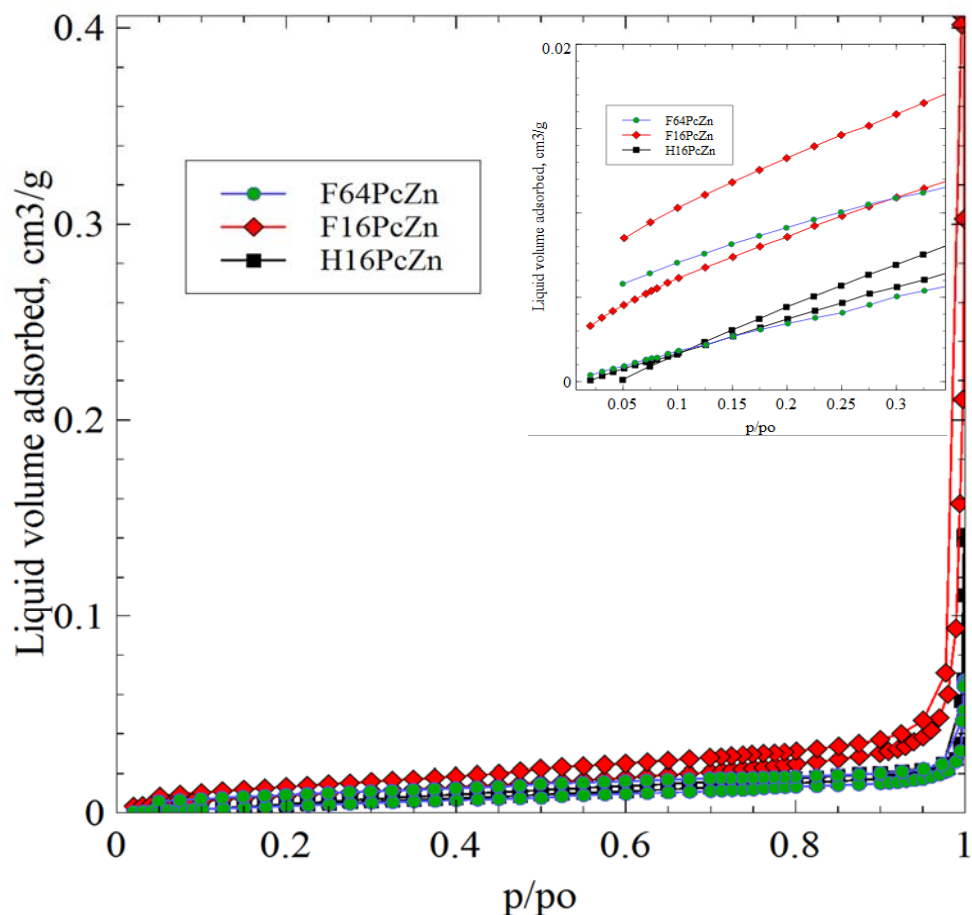
Figure 56. Nitrogen adsorption-desorption isotherm of three bare fluorinated Pcs. Inset shows the BET region for surface area calculation.

Table 17. Structural parameters of bare Pcs from nitrogen adsorption isotherm. Density was obtained from crystal structure data[94]. Maximum intermolecular distance was obtained for each Pc using 3D space filling model at face on orientation[98].

Sample Name	Surface Area, m^2/g	Density (Calculated) g/cm^3	Maximum Intermolecular Distance or Diameter (Å)	% Difference ($H_{16}PcZn$ as reference)	Diameter (calculated) Å	% Difference ($H_{16}PcZn$ as reference)
$H_{16}PcZn$	41	1.62	35.6	0	900	0
$F_{16}PcZn$	24	1.97	36.4	~2	1250	~39
$F_{64}PcZn$	17	1.89	41.8	~17	1880	~109

130
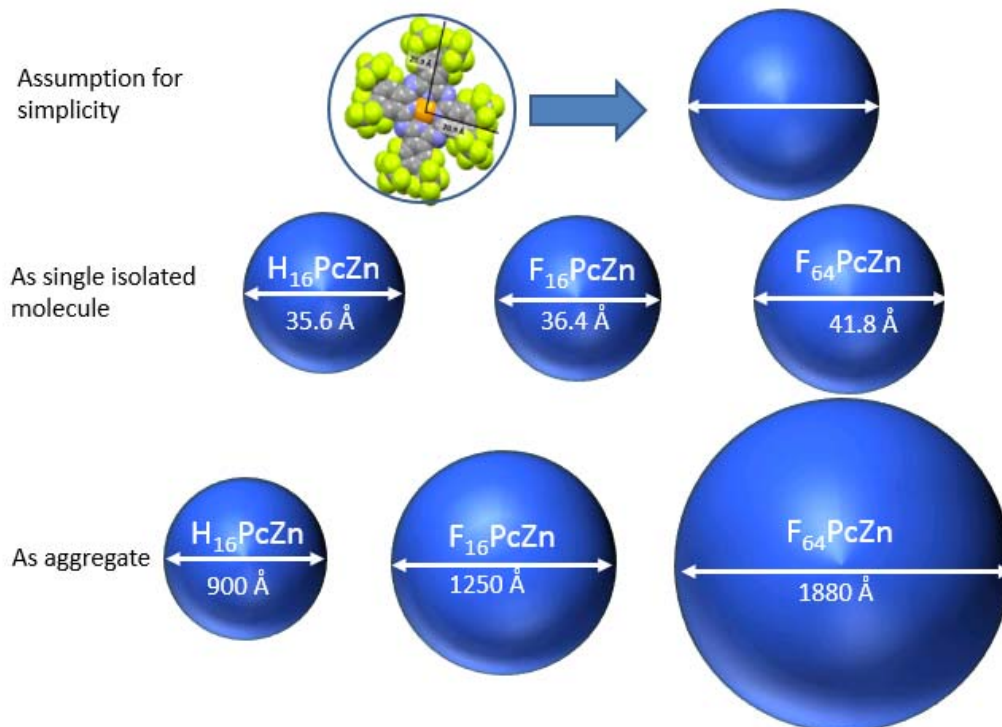
Figure 57. Cartoon comparing Pcs as a single molecule or an aggregate. For simplicity a Pc molecule in face on orientations is considered as a sphere.

If Pcs exists as aggregates in bulk solid, the size of aggregates as indicated in Table 17 can be stated as $F_{64}PcZn > F_{16}PcZn > H_{16}PcZn$. It can be further inferred that higher the size of the aggregates, higher the distance or separation between two molecules. One primary goal to incorporate bulky substituents on the periphery of Pc molecules is to provide a means to modify stacking aggregation which in turn is believed to improve electronic and optical properties of the Pcs. Dwyer, Vander Valk, Caltado, Demianicz and Kelty[111] using molecular dynamics simulations investigated equilibrium stacking and orientational intermolecular interactions of this novel class of modified phthalocyanines. Dwyer et al[111] observed significant stacking $H_{16}PcZn$ and $F_{16}PcZn$ molecules and they attribute this to the lack of bulky peripheral substituents that would induce steric hindrance as in the case of $F_{64}PcZn$(less or no stacking). Given the same number of molecules, Pc that shows significant stacking aggregations would aggregate in a much tighter

fashion leading to aggregates with lesser size (diameter) i.e higher the stacking aggregation tendency, lower the size of the aggregate. This finding (stacking aggregation order: $F_{64}PcZn \ll F_{16}PcZn < H_{16}PcZn$) by Dwyer et al[111] is in agreement with the findings in this work (calculated diameter order : $F_{64}PcZn \gg F_{16}PcZn > H_{16}PcZn$) using nitrogen adsorption data.

4.3.4.2 Water adsorption measurements

As assessed by water, the fluorinated and non-fluorinated bare Pcs ($H_{16}PcZn$, $F_{16}PcZn$ and $F_{64}PcZn$) presented different isotherms. Figure 58 shows the water adsorption data on the three bare Pcs. Amount of water adsorbed is significantly lower in the non-fluorinated Pc ($H_{16}PcZn$) as compared to the two fluorinated Pcs ($F_{16}PcZn$ and $F_{64}PcZn$). This seems to defy the common perception about water adsorption on fluorinated surfaces i.e fluorinated silica would be more hydrophobic and hence water adsorption would be low.
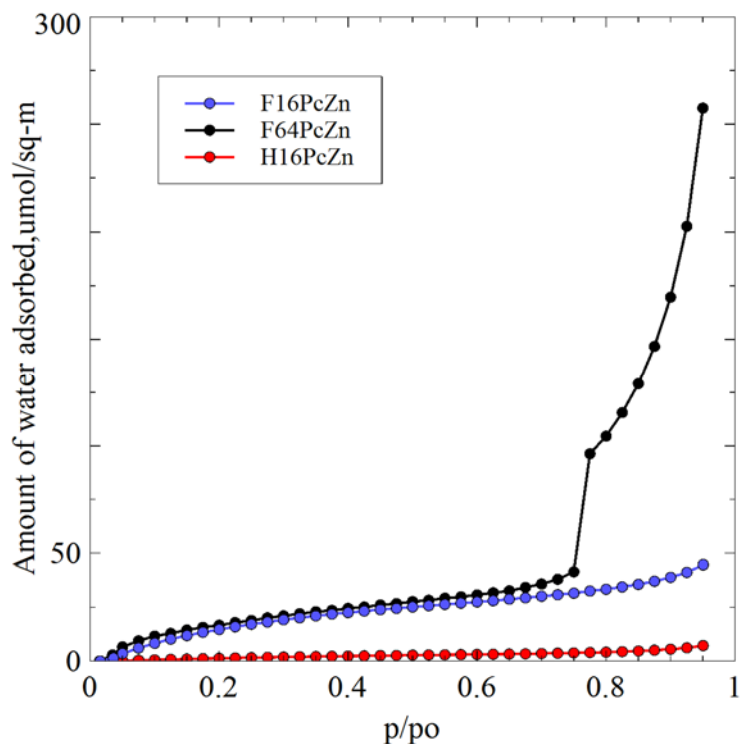
Figure 58. Water adsorption isotherm of three bare fluorinated Pcs.

To obtain further understanding, we can compare the water adsorption on these bare Pcs with our model silica surfaces (hydrophilic and hydrophobic). Figure 59 shows the water adsorption on the three bare Pcs in comparison with hydroxylated silica. Interestingly, the fluorinated Pcs ($F_{16}PcZn$ and $F_{64}PcZn$) shows significantly higher water adsorption as compared to hydroxylated silica and the non-fluorinated Pc ($H_{16}PcZn$) shows low water adsorption than the hydroxylated silica.
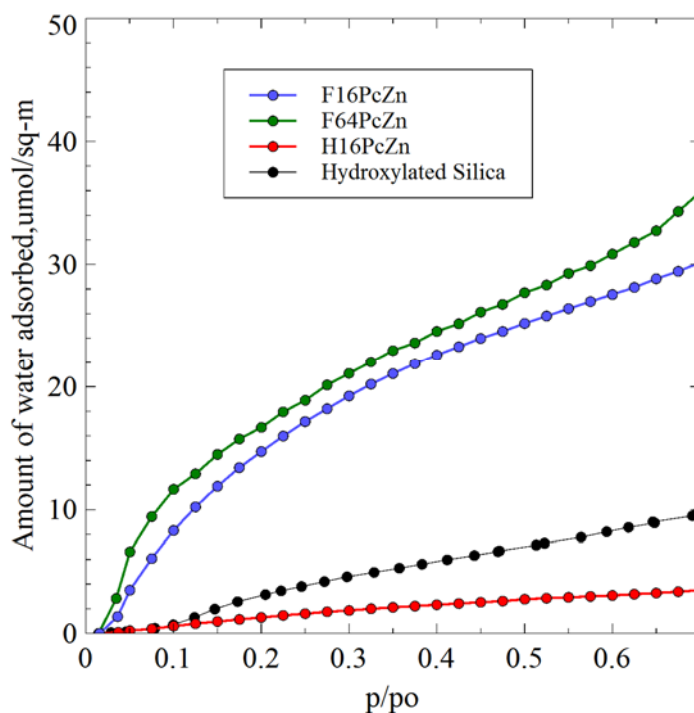
Figure 59. Water adsorption isotherm of three bare fluorinated Pcs in comparison with hydroxylated silica

Figure 60 shows the water adsorption on $H_{16}PcZn$ in comparison with hydroxylated, dehydroxylated and hydrophobic silica. Again interestingly, the water adsorption on $H_{16}PcZn$ is very comparable to water adsorption on dehydroxylated and hydrophobic silica. In an effort to understand this behavior of Pcs with respect to water adsorption, the electronic deficiency of the metal (Zn) center in the three Pcs were compared and it follows as: $H_{16}PcZn << F_{16}PcZn <$

$F_{64}PcZn$. Due to the highly electron withdrawing tendency of fluorine atoms, the central metal becomes increasingly electron deficient, as the fluorination increases. When the highly electron deficient metal center in $F_{64}PcZn$ and $F_{16}PcZn$ as compared to $H_{16}PcZn$ comes in contact with water, the metal is thirsty for electrons and hence tends to adsorb more water. Hence, the amount of water adsorbed by three different Pcs can be correlated to the electron deficiency of the metal center in the Pcs.
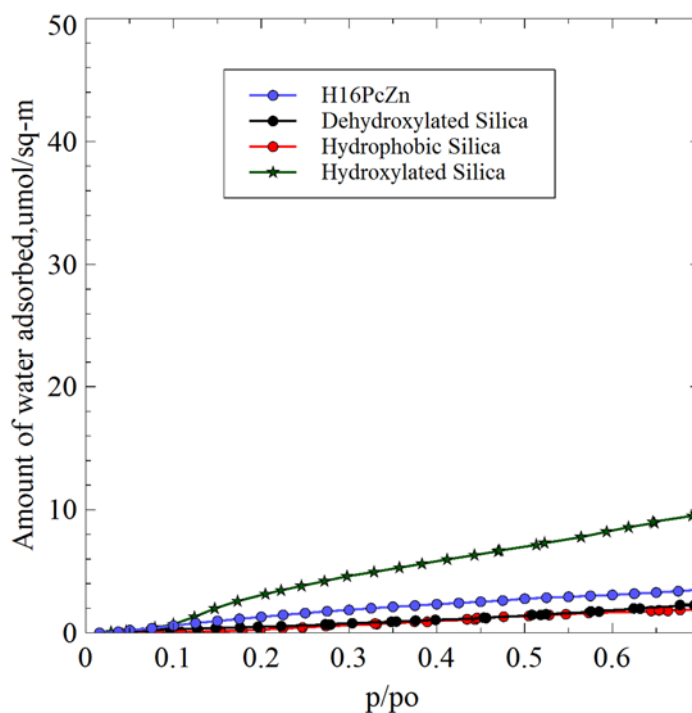
Figure 60. Water adsorption isotherm of bare $H_{16}PcZn$ in comparison with hydroxylated silica, dehydroxylated and hydrophobic silica.

4.3.4.3 Nitrogen and Water molecules per MPc

In an effort to understand how the adsorbates (water or nitrogen) interact with MPcs or vice versa, the number of nitrogen and water molecules per MPc were calculated. Table 18 provides the number of nitrogen and water molecules per MPc at $p/p_o = 0.3$ for all the three Pcs. The number of nitrogen molecules per MPc is not that significantly different for the three Pcs while the number

of water molecules per MPc is significantly different for the three Pcs . It would be expected that with increase in perfluoro groups, hydrophobicity of Pc would increase resulting in decreased affinity to water. However, the number of water molecules per MPc increases significantly as fluorination increases ($H_{16}PcZn$ to $F_{16}PcZn$ to $F_{64}PcZn$). This significant difference in water molecules per MPc further correlates with the theory that the metal center becomes increasingly electron deficient with increased fluorination.

Table 18. Calculation of nitrogen and water molecules per MPc. MPcs are considered in face on orientation and equation 4-3 is used to calculate no of adsorbate molecules per MPc.

Sample	CSA of MPc ($Å^2$/molecule)	No of water molecules per MPc (p/p_o=0.3)	No of nitrogen molecules per MPc (p/p_o =0.3)
$F_{64}PcZn$	437	55	22.5
$F_{16}PcZn$	332	39	26
$H_{16}PcZn$	317	3.5	14

Figure 61 shows the number of water molecules per MPc calculated at a range of relative pressures. In general fluorinated organic materials synthesized for electronic and optoelectronic applications are perceived to have enhanced hydrophobic properties. However form the water adsorption studies in this work and in specifically as shown in Figure 61, the number of water molecules per MPc is higher for heavily fluorinated $F_{64}PcZn$. This higher adsorption of water by fluorinated Pcs led us to believe that that fluorinated MPcs are not hydrophobic and in fact they very much prefer to interact with water molecules through metal centers.
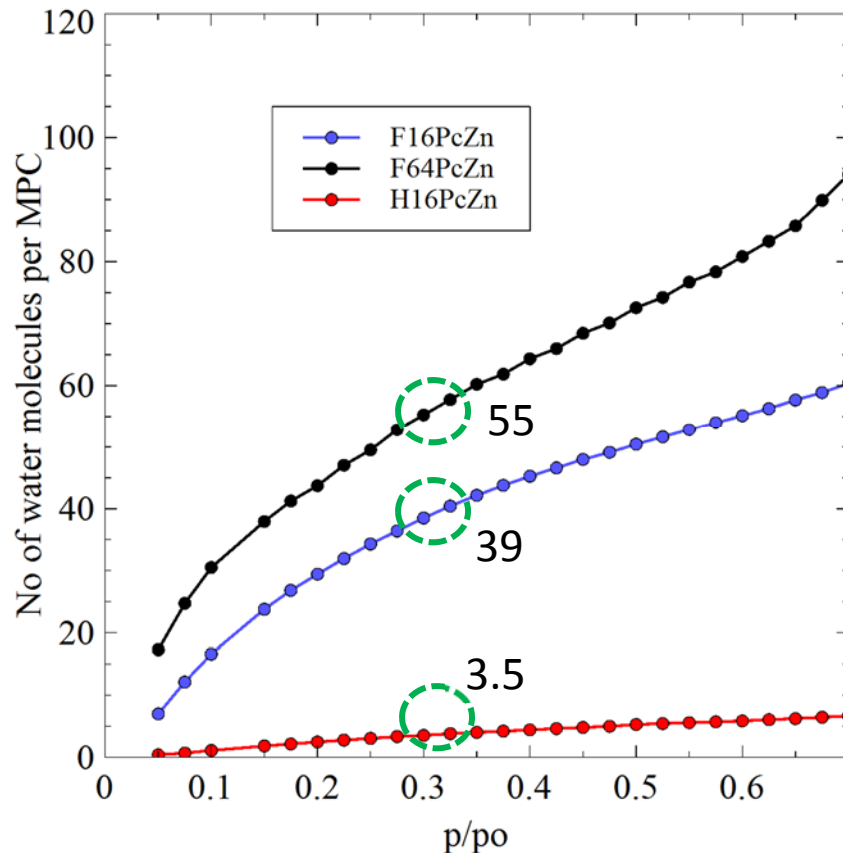
Figure 61. No of water molecules per MPc at various p/p₀. No of water molecules at p/pₒ = 0.3 is circled and value provided.

Figure 62 provides an overlay of the number of nitrogen and water molecules per $F_{64}PcZn$ molecule. Since the area requirement of a nitrogen and water molecule are 16.2 Å^2 and 10.5Å^2 respectively, the number of nitrogen and water molecules to obtain a monolayer coverage are 27 and 42 molecules respectively. As shown in Figure 62, the monolayer coverage is achieved at *p/p₀ of 0.*375 for nitrogen and at a *p/p₀ of 0.*175 for water adsorption. The number of nitrogen molecules adsorbed over a range of relative pressure depicts a linear fit suggesting a multilayer followed by monolayer, while the number of water molecules adsorbed over a range of relative pressure depicts an exponential fit suggesting a co-operative mechanism[70]. In the case of water adsorption, once a fixed number of water molecules are present on the surface, the adsorbate–adsorbate forces become dominant, and these forces promote the adsorption of additional molecules of water.
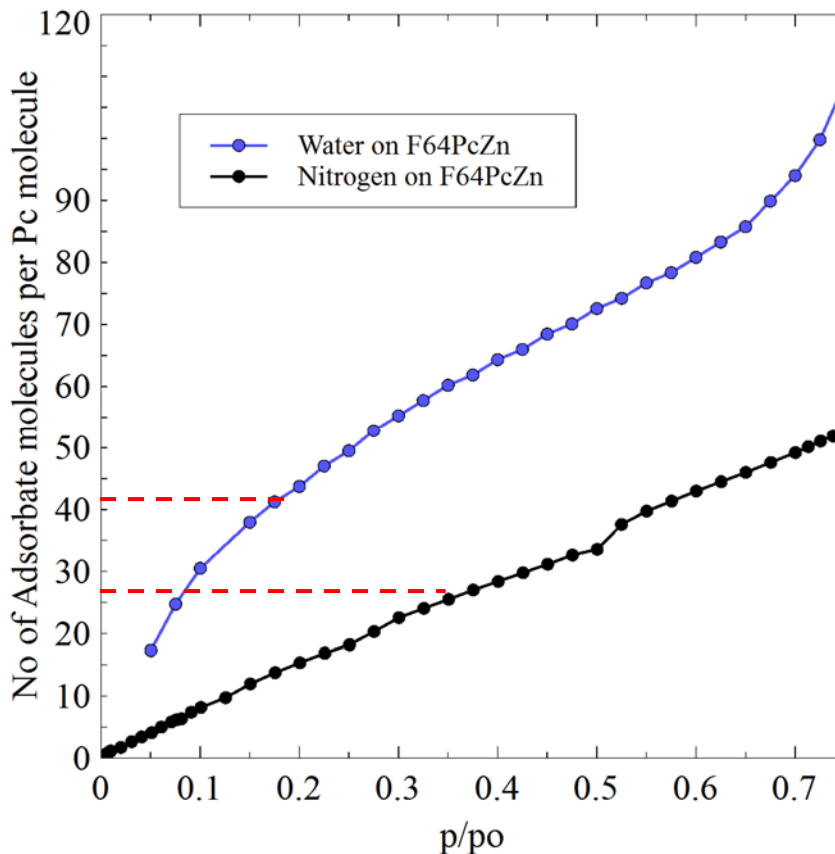
Figure 62. Overlay of no of water molecules per $F_{64}PcZn$ and no of nitrogen molecules per $F_{64}PcZn$ at various p/p_0. The red dotted lines indicate the monolayer coverage.

4.3.5 Adsorption measurements on fluorinated phthalocyanines adsorbed on mesoporous alumina

With the understanding on the adsorption of nitrogen and water on bare fluorinated phthalocyanines, it would be worthwhile to look at the adsorption of water and nitrogen on Pcs that has been entrapped or encapsulated or adsorbed on to metal oxides. However, based on the discussion in section 4.3.1, solution adsorption on mesoporous alumina gave relatively the highest surface coverage and hence this sample was chosen to for nitrogen and water adsorption measurements. Figure 63 shows the nitrogen adsorption on bare mesoporous alumina and $F_{64}PcZn$ adsorbed on mesoporous alumina. The nitrogen isotherms exhibit hysteresis and the isotherms fit the Type IV that correspond to mesoporous adsorbents. The BET surface area are 175 m^2/g and

167 m^2/g for the bare mesoporous alumina and F$_{64}$PcZn adsorbed mesoporous alumina respectively. The relatively small decrease in surface area between bare and loaded mesoporous alumina is attributed to the fact that the immobilization technique yielded a low surface coverage. Due to the low surface coverage and the fact that nitrogen does not differentiate the surface chemistry (bare alumina surface and alumina with F$_{64}$PcZn) the isotherms exactly overlay without any substantial difference.
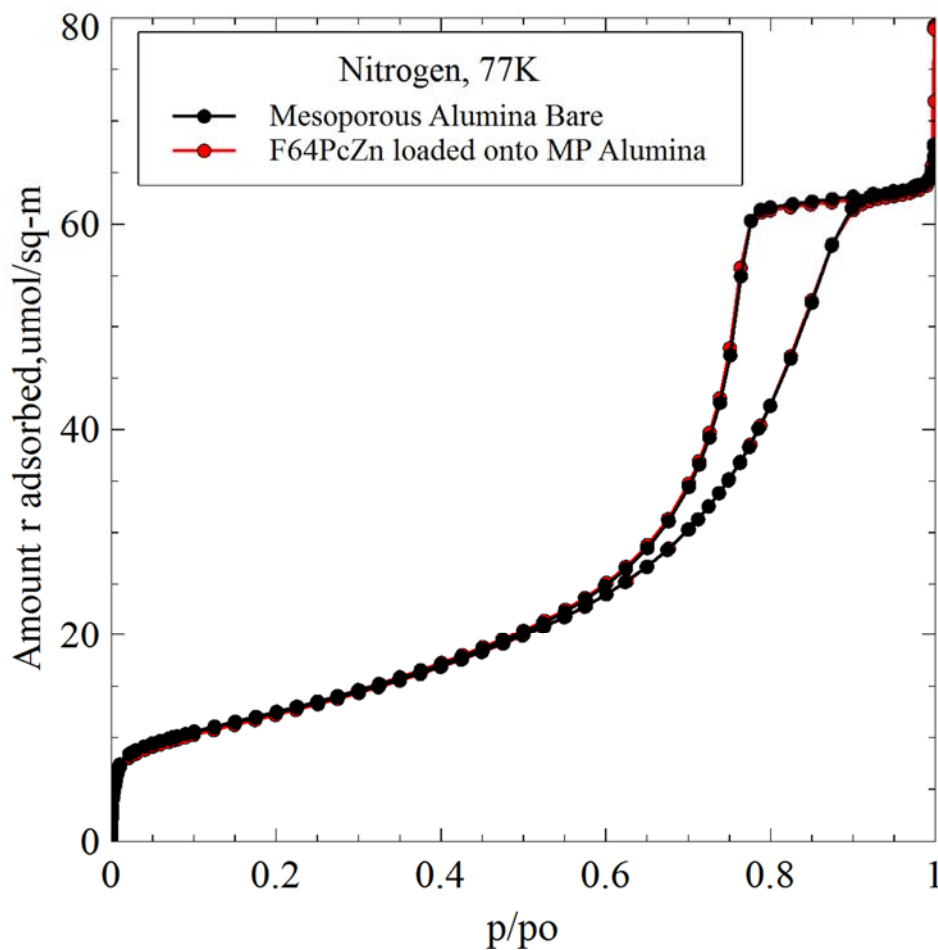
Figure 63. Nitrogen adsorption isotherms on bare mesoporous alumina and F64PcZn adsorbed mesoporous alumina.

Figure 64 shows the water adsorption on bare mesoporous alumina and F$_{64}$PcZn adsorbed on mesoporous alumina. The small difference in the shape of the hysteresis loop between bare and

$F_{64}PcZn$ adsorbed mesoporous alumina could be attributed to the presence of $F_{64}PcZn$ inside the mesopores. Using the combined vapor adsorption study to determine water contact angles inside mesopores in Chapter 3, contact angle of water in bare and $F_{64}PcZn$ adsorbed mesoporous alumina was obtained and shown in Table 19. Water contact angles for bare and $F_{64}PcZn$ adsorbed mesoporous alumina are 14.8 and 11.9 degree respectively. Since bare $F_{64}PcZn$ has great affinity for water than even hydroxylated metal surfaces, it is not surprising to see similar contact angles for bare alumina and alumina with $F_{64}PcZn$ adsorbed on it. A slightly lower contact angle in the alumina with $F_{64}PcZn$ than the bare alumina further suggest that there is $F_{64}PcZn$ inside the mesopores **.**
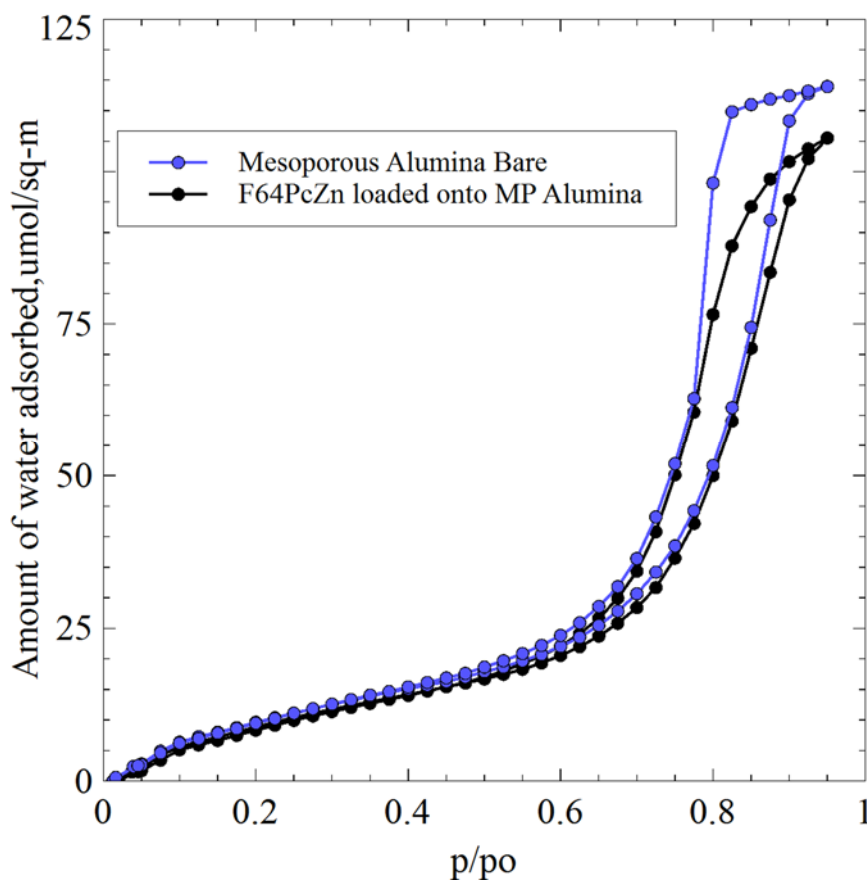
Figure 64. Water adsorption isotherms on bare mesoporous alumina and F64PcZn adsorbed mesoporous alumina.

Table 19. Water contact angles and structural parameters for the bare mesoporous alumina and $F_{64}PcZn$ adsorbed mesoporous alumina.

Sample	S(N₂), m²/g	V(N₂), cm³/g	r(N₂), nm	rₘ(H₂O), nm	t(H₂O), nm	cosθ	θ, deg
Mesoporous Alumina Bare	175	0.42	4.4	3.75	0.78	0.967	14.8
F₆₄PcZn adsorbed Mesoporous Alumina	165	0.42	4.4	3.75	0.73	0.978	11.9

4.3 Conclusions

Replacement of C-H bonds in phthalocyanines with F and/or i-C₃F₇ groups produces catalytically active materials resistant to thermal and oxidative stress with increased solubility, reduced aggregation and an increasingly electron deficient metal center[94, 98]. Several immobilization techniques to load MPcs on metal oxides were investigated for and the advantages and limitations of each technique were understood. All the three desired outcomes (thermal stability, solvent leaching resistance and catalytic activity) were not achievable solely with a single immobilization technique. Solution adsorption on mesoporous alumina provided the highest surface coverage, mesopore entrapment technique provided higher solvent stability (leaching resistance) and deposition by pore filling followed by encapsulation offered the best improved thermal stability for few hours at 300C°. The importance of nitrogen and water adsorption studies on bare metal phthalocyanines was demonstrated. The fluorinated Pcs (F₁₆PcZn and F₆₄PcZn) showed significantly higher water adsorption as compared to hydroxylated silica and the non-fluorinated Pc (H₁₆PcZn) shows low water adsorption than the hydroxylated silica. The amount of water adsorbed by three different Pcs was correlated to the electron deficiency of the metal center in the Pcs. As a continuation of this work, fluorinated metal phthalocyanines could be entrapped onto ordered mesoporous alumina in a one-step synthesis and their surface characteristics, catalytic

activity, thermal stability and solvent stability could be studied. The technique of immobilization and characterization can be extended to other fluorinated phthalocyanines with different metals-fluorinated Ru phthalocyanines would be an excellent choice to pursue further studies.

References

1.   Bergna, H. E., Colloid Chemistry of Silica. In *The Colloid Chemistry of Silica*, American Chemical Society: 1994; Vol. 234, pp 1-47.

2.   K.K.Unger, Chapter 1 General chemistry of silica. In *Journal of Chromatography Library*, Unger, K. K., Ed. Elsevier: 1979; Vol. Volume 16, pp 1-14.

3.   Iler, R. K., The Chemistry of Silica. *Wiley-Interscience: New York* **1979**.

4.   Vansant, E. F., Van Der Voort, P, Vrancken K.C., Characterization and chemical modifciation of the silica surface. *Studies in Surface Science and Catalysis* **1995,** *93*.

5.   AEROSIL® – Fumed Silica. *Technical Bulletin, Evonik Industries* **2015**.

6.   Zhuravlev, L. T., The surface chemistry of amorphous silica. Zhuravlev model. *Colloids and Surfaces A: Physicochemical and Engineering Aspects* **2000,** *173* (1–3), 1-38.

7.   Rouquerol, F. o.; Rouquerol, J.; Sing, K. S. W., *Adsorption by Powders and Porous Solids : Principles, Methodology, and Applications*. Academic Press: San Diego, 1999.

8.   S.J.Gregg; K.S.W.Sing, Adsorption, Surface Area and Porosity. *Academic Press, London* **1982**.

9.   ALOthman, Z., A Review: Fundamental Aspects of Silicate Mesoporous Materials. *Materials* **2012,** *5* (12), 2874.

10.   Beck, J. S.; Vartuli, J. C.; Roth, W. J.; Leonowicz, M. E.; Kresge, C. T.; Schmitt, K. D.; Chu, C. T. W.; Olson, D. H.; Sheppard, E. W.; McCullen, S. B.; Higgins, J. B.; Schlenker, J. L., A new family of mesoporous molecular sieves prepared with liquid crystal templates. *Journal of the American Chemical Society* **1992,** *114* (27), 10834-10843.

11.   Kresge, C. T.; Leonowicz, M. E.; Roth, W. J.; Vartuli, J. C.; Beck, J. S., Ordered mesoporous molecular sieves synthesized by a liquid-crystal template mechanism. *Nature* **1992,** *359* (6397), 710-712.

12.   Vartuli, J. C.; Schmitt, K. D.; Kresge, C. T.; Roth, W. J.; Leonowicz, M. E.; McCullen, S. B.; Hellring, S. D.; Beck, J. S.; Schlenker, J. L., Effect of Surfactant/Silica Molar Ratios on the Formation of Mesoporous Molecular Sieves: Inorganic Mimicry of Surfactant Liquid-Crystal Phases and Mechanistic Implications. *Chemistry of Materials* **1994,** *6* (12), 2317-2326.

13.   Thomas, F. D.; Wielsaw, J. R.; James, C. V., Mesoporous Materials. In *Dekker Encyclopedia of Nanoscience and Nanotechnology, Second Edition*, Taylor & Francis: 2009; Vol. null, pp 2029-2043.

14.   Zhao, D.; Huo, Q.; Feng, J.; Chmelka, B. F.; Stucky, G. D., Nonionic Triblock and Star Diblock Copolymer and Oligomeric Surfactant Syntheses of Highly Ordered, Hydrothermally

Stable, Mesoporous Silica Structures. *Journal of the American Chemical Society* **1998,** *120* (24), 6024-6036.

15.   Bagshaw, S. A.; Prouzet, E.; Pinnavaia, T. J., Templating of Mesoporous Molecular Sieves by Nonionic Polyethylene Oxide Surfactants. *Science* **1995,** *269* (5228), 1242-1244.

16.   Jun, S.; Ryoo, R., Aluminum Impregnation into Mesoporous Silica Molecular Sieves for Catalytic Application to Friedel–Crafts Alkylation. *Journal of Catalysis* **2000,** *195* (2), 237-243.

17.   Yu, C.; Yu, Y.; Zhao, D., Highly ordered large caged cubic mesoporous silica structures templated by triblock PEO-PBO-PEO copolymer. *Chemical Communications* **2000,** (7), 575-576.

18.   Che, S.; Garcia-Bennett, A. E.; Yokoi, T.; Sakamoto, K.; Kunieda, H.; Terasaki, O.; Tatsumi, T., A novel anionic surfactant templating route for synthesizing mesoporous silica with unique structure. *Nat Mater* **2003,** *2* (12), 801-805.

19.   Kulinowski, K. M.; Jiang, P.; Vaswani, H.; Colvin, V. L., Porous Metals from Colloidal Templates. *Advanced Materials* **2000,** *12* (11), 833-838.

20.   Xia, Y.; Gates, B.; Yin, Y.; Lu, Y., Monodispersed Colloidal Spheres: Old Materials with New Applications. *Advanced Materials* **2000,** *12* (10), 693-713.

21.   Velev, O. D.; Lenhoff, A. M.; Kaler, E. W., A Class of Microstructured Particles Through Colloidal Crystallization. *Science* **2000,** *287* (5461), 2240-2243.

22.   Iskandar, F.; Nandiyanto, A. B. D.; Widiyastuti, W.; Young, L. S.; Okuyama, K.; Gradon, L., Production of morphology-controllable porous hyaluronic acid particles using a spray-drying method. *Acta Biomaterialia* **2009,** *5* (4), 1027-1034.

23.   Lee, S. Y.; Gradon, L.; Janeczko, S.; Iskandar, F.; Okuyama, K., Formation of Highly Ordered Nanostructures by Drying Micrometer Colloidal Droplets. *ACS Nano* **2010,** *4* (8), 4717-4724.

24.   Cho, Y.-S.; Choi, S.-Y.; Kim, Y.-K.; Yi, G.-R., Bulk synthesis of ordered macroporous silica particles for superhydrophobic coatings. *Journal of Colloid and Interface Science* **2012,** *386* (1), 88-98.

25.   Ebelmen, Untersuchungen über die Verbindungen der Borsäure und Kieselsäure mit Aether. *Justus Liebigs Annalen der Chemie* **1846,** *57* (3), 319-355.

26.   Danks, A. E.; Hall, S. R.; Schnepp, Z., The evolution of 'sol-gel' chemistry as a technique for materials synthesis. *Materials Horizons* **2016,** *3* (2), 91-112.

27.   Brinker, C. J.; Scherer, G. W., *Sol-gel Science: The Physics and Chemistry of Sol-gel Processing*. Academic Press: 1990.

28.   Kistler, S. S., Coherent Expanded-Aerogels. *The Journal of Physical Chemistry* **1931,** *36* (1), 52-64.

29.   Roy, R., Aids in Hydrothermal Experimentation: II, Methods of Making Mixtures for Both "Dry" and "Wet" Phase Equilibrium Studies. *Journal of the American Ceramic Society* **1956,** *39* (4), 145-146.

30.   Buckley, A. M.; Greenblatt, M., The Sol-Gel Preparation of Silica Gels. *Journal of Chemical Education* **1994,** *71* (7), 599.

31.   Hench, L. L.; West, J. K., The sol-gel process. *Chemical Reviews* **1990,** *90* (1), 33-72.

32.   Li, W.; Zhao, D., An overview of the synthesis of ordered mesoporous materials. *Chemical Communications* **2013,** *49* (10), 943-946.

33.   Perego, C.; Millini, R., Porous materials in catalysis: challenges for mesoporous materials. *Chemical Society Reviews* **2013,** *42* (9), 3956-3976.

34.   Davis, M. E., Ordered porous materials for emerging applications. *Nature* **2002,** *417* (6891), 813-821.

35.   Vincent, C.; E, R. J.; D, V. C., Process for producing low-bulk density silica. Google Patents: 1971.

36.   T.Yanagisawa; T.Shimizu; K.Juroda; C.Kato, The Preparation of Alkyltrimethylammonium–Kaneinite Complexes and Their Conversion to Microporous Materials *Bull.Chem.Soc* **1990,** *63* (4), 988.

37.   Inagaki, S.; Fukushima, Y.; Kuroda, K., Synthesis of highly ordered mesoporous materials from a layered polysilicate. *Journal of the Chemical Society, Chemical Communications* **1993,** (8), 680-682.

38.   Wan, Y.; Zhao, On the Controllable Soft-Templating Approach to Mesoporous Silicates. *Chemical Reviews* **2007,** *107* (7), 2821-2860.

39.   Thommes, M., Physical Adsorption Characterization of Nanoporous Materials. *Chemie Ingenieur Technik* **2010,** *82* (7), 1059-1073.

40.   Lowell, S.; Shields, J. E.; Thomas, M. A.; Thommes, M., *Characterization of Porous Solids and Powders: Surface Area, Pore Size and Density*. Springer Netherlands: 2006.

41.   Kiselev, A. V., Non-specific and specific interactions of molecules of different electronic structures with solid surfaces. *Discussions of the Faraday Society* **1965,** *40* (0), 205-218.

42.   Zhuravlev, L. T., Surface characterization of amorphous silica—a review of work from the former USSR. *Colloids and Surfaces A: Physicochemical and Engineering Aspects* **1993,** *74* (1), 71-90.

43.   Hockey, J. A.; Pethica, B. A., Surface hydration of silicas. *Transactions of the Faraday Society* **1961,** *57* (0), 2247-2262.

44.   Smith, R. C.; Kellum, G. E., Modified Karl Fischer Titration for Determination of Water in Presence of Silanol and Other Interfering Materials. *Analytical Chemistry* **1966,** *38* (1), 67-72.

45.   Mueller, R.; Kammler, H. K.; Wegner, K.; Pratsinis, S. E., OH Surface Density of SiO2 and TiO2 by Thermogravimetric Analysis. *Langmuir* **2003,** *19* (1), 160-165.

46.   Wisser, F. M.; Abele, M.; Gasthauer, M.; Müller, K.; Moszner, N.; Kickelbick, G., Detection of surface silanol groups on pristine and functionalized silica mixed oxides and zirconia. *Journal of Colloid and Interface Science* **2012,** *374* (1), 77-82.

47.   Yang, J.; Wang, E. G., Reaction of water on silica surfaces. *Current Opinion in Solid State and Materials Science* **2006,** *10* (1), 33-39.

48.   Hair, M. L., Hydroxyl groups on silica surface. *Journal of Non-Crystalline Solids* **1975,** *19*, 299-309.

49.   Grivtsov, A. G.; Zhuravlev, L. T.; Gerasimova, G. A.; Khazin, L. G., Molecular dynamics of water: Adsorption of water on β-tridymite. *Journal of Colloid and Interface Science* **1988,** *126* (2), 397-407.

50.   Lange, K. R., The characterization of molecular water on silica surfaces. *Journal of Colloid Science* **1965,** *20* (3), 231-240.

51.   Young, G. J., Interaction of water vapor with silica surfaces. *Journal of Colloid Science* **1958,** *13* (1), 67-85.

52.   Young, G. J.; Bursh, T. P., Immersion calorimetry studies of the interaction of water with silica surfaces. *Journal of Colloid Science* **1960,** *15* (4), 361-369.

53.   Agzamkhodzhaev, A. A.; Zhuravlev, L. T.; Kiselev, A. V.; Shengeliya, K. Y., Concentration of hydroxyl groups on the surface and in the volume of silicas. *Bulletin of the Academy of Sciences of the USSR, Division of chemical science* **1969,** *18* (10), 1968-1973.

54.   Hair, M. L., *Infrared spectroscopy in surface chemistry*. Dekker: New York, 1967.

55.   Sing, K., The use of nitrogen adsorption for the characterisation of porous materials. *Colloids and Surfaces A: Physicochemical and Engineering Aspects* **2001,** *187–188*, 3-9.

56.   Langmuir, I., THE CONSTITUTION AND FUNDAMENTAL PROPERTIES OF SOLIDS AND LIQUIDS. PART I. SOLIDS. *Journal of the American Chemical Society* **1916,** *38* (11), 2221-2295.

57.   Benton, A. F.; White, T. A., THE SORPTION OF GASES BY IRON. *Journal of the American Chemical Society* **1932,** *54* (5), 1820-1830.

58.   Brunauer, S.; Emmett, P. H., The Use of Low Temperature van der Waals Adsorption Isotherms in Determining the Surface Areas of Various Adsorbents. *Journal of the American Chemical Society* **1937,** *59* (12), 2682-2689.

59.   Brunauer, S.; Emmett, P. H.; Teller, E., Adsorption of Gases in Multimolecular Layers. *Journal of the American Chemical Society* **1938,** *60* (2), 309-319.

60.   Jelinek, L.; sz. Kovats, E., True Surface Areas from Nitrogen Adsorption Experiments. *Langmuir* **1994,** *10* (11), 4225-4231.

61.   Schull, C. G., The Determination of Pore Size Distribution from Gas Adsorption Data. *Journal of the American Chemical Society* **1948,** *70* (4), 1405-1410.

62.   Barrett, E. P.; Joyner, L. G.; Halenda, P. P., The Determination of Pore Volume and Area Distributions in Porous Substances. I. Computations from Nitrogen Isotherms. *Journal of the American Chemical Society* **1951,** *73* (1), 373-380.

63.   kelvin), W. T. T. L., On the Equilibrium of Vapour at a Curved Surface of Liquid. *Phil. Mag.* **1871,** *42*, 448.

64.   Zsigmondy, A., Structure of Gelatinous Silicic Acid. Theory of Dehydration. *Zeitschrift fuer Anorganische Chemie* **1911,** *71*, 356-77.

65.   Sing, K. S. W., Reporting physisorption data for gas/solid systems with special reference to the determination of surface area and porosity (Recommendations 1984). In *Pure and Applied Chemistry*, 1985; Vol. 57, p 603.

66.   Thommes, M.; Morell, J.; Cychosz, K. A.; Fröba, M., Combining Nitrogen, Argon, and Water Adsorption for Advanced Characterization of Ordered Mesoporous Carbons (CMKs) and Periodic Mesoporous Organosilicas (PMOs). *Langmuir* **2013,** *29* (48), 14893-14902.

67.   Naono, H.; Hakuman, M., Analysis of adsorption isotherms of water vapor for nonporous and porous adsorbents. *Journal of Colloid and Interface Science* **1991,** *145* (2), 405-412.

68.   Hagymassy, J.; Brunauer, S.; Mikhail, R. S., Pore structure analysis by water vapor adsorption. *Journal of Colloid and Interface Science* **1969,** *29* (3), 485-491.

69.   Naono, H.; Hakuman, M., Analysis of Porous Texture by Means of Water Vapor Adsorption Isotherm with Particular Attention to Lower Limit of Hysteresis Loop. *Journal of Colloid and Interface Science* **1993,** *158* (1), 19-26.

70.   Raoof, A.; Guilbaud, J.-P.; Van Damme, H.; Porion, P.; Levitz, P., Analysis of the Multilayer Thickness Relationship for Water Vapor and Nitrogen Adsorption. *Journal of Colloid and Interface Science* **1998,** *206* (1), 1-9.

71.   Bernardoni, F.; Fadeev, A. Y., Adsorption and wetting characterization of hydrophobic SBA-15 silicas. *Journal of Colloid and Interface Science* **2011,** *356* (2), 690-698.

72.	Kozlova, S. A.; Kirik, S. D., Post-synthetic activation of silanol covering in the mesostructured silicate materials MCM-41 and SBA-15. *Microporous and Mesoporous Materials* **2010,** *133* (1–3), 124-133.

73.	Haynes, W. M.; Lide, D. R.; Bruno, T. J., *CRC handbook of chemistry and physics : a ready-reference book of chemical and physical data*. 2015.

74.	Galarneau, A.; Nader, M.; Guenneau, F.; Di Renzo, F.; Gedeon, A., Understanding the Stability in Water of Mesoporous SBA-15 and MCM-41. *The Journal of Physical Chemistry C* **2007,** *111* (23), 8268-8277.

75.	Pollock, R. A.; Gor, G. Y.; Walsh, B. R.; Fry, J.; Ghampson, I. T.; Melnichenko, Y. B.; Kaiser, H.; DeSisto, W. J.; Wheeler, M. C.; Frederick, B. G., Role of Liquid vs Vapor Water in the Hydrothermal Degradation of SBA-15. *The Journal of Physical Chemistry C* **2012,** *116* (43), 22802-22814.

76.	Erko, M.; Wallacher, D.; Findenegg, G. H.; Paris, O., Repeated sorption of water in SBA-15 investigated by means of in situ small-angle x-ray scattering. *Journal of Physics: Condensed Matter* **2012,** *24* (28), 284112.

77.	Celer, E. B.; Kruk, M.; Zuzek, Y.; Jaroniec, M., Hydrothermal stability of SBA-15 and related ordered mesoporous silicas with plugged pores. *Journal of Materials Chemistry* **2006,** *16* (27), 2824-2833.

78.	Gouze, B.; Cambedouzou, J.; Parrès-Maynadié, S.; Rébiscoul, D., How hexagonal mesoporous silica evolves in water on short and long term: Role of pore size and silica wall porosity. *Microporous and Mesoporous Materials* **2014,** *183*, 168-176.

79.	Zhang, F.; Yan, Y.; Yang, H.; Meng, Y.; Yu, C.; Tu, B.; Zhao, D., Understanding Effect of Wall Structure on the Hydrothermal Stability of Mesostructured Silica SBA-15. *The Journal of Physical Chemistry B* **2005,** *109* (18), 8723-8732.

80.	Ribeiro Carrott, M. M. L.; Estêvão Candeias, A. J.; Carrott, P. J. M.; Unger, K. K., Evaluation of the Stability of Pure Silica MCM-41 toward Water Vapor. *Langmuir* **1999,** *15* (26), 8895-8901.

81.	Kocherbitov, V.; Alfredsson, V., Hydration of MCM-41 Studied by Sorption Calorimetry. *The Journal of Physical Chemistry C* **2007,** *111* (35), 12906-12913.

82.	Lamb, R. N.; Furlong, D. N., Controlled wettability of quartz surfaces. *Journal of the Chemical Society, Faraday Transactions 1: Physical Chemistry in Condensed Phases* **1982,** *78* (1), 61-73.

83.	Israelachvili, J. N.; Gee, M. L., Contact angles on chemically heterogeneous surfaces. *Langmuir* **1989,** *5* (1), 288-289.

84.   Sindorf, D. W.; Maciel, G. E., Cross-polarization magic-angle-spinning silicon-29 nuclear magnetic resonance study of silica gel using trimethylsilane bonding as a probe of surface geometry and reactivity. *The Journal of Physical Chemistry* **1982,** *86* (26), 5208-5219.

85.   Fadeev, A. Y., Hydrophobic Monolayer Surfaces: Synthesis and Wettability. In *Encyclopedia of Surface and Colloid Science, Third Edition*, CRC Press: 2015; pp 3120-3140.

86.   Dzhigit, O. M. K., A.V.; Muttik, G.G., Heat of Adsorption of Water Vapor on Silica Gel with Hydrated and Dehydrated Surface. *Colloid J.* **1961,** *23*, 553-562.

87.   Collins, K. E.; de Camargo, V. R.; Dimiras, A. B.; Menezes, D. T. C.; da Silva, P. A.; Collins, C. H., Physisorbed water layer formation on fully hydroxylated mesoporous silicas. *Journal of Colloid and Interface Science* **2005,** *291* (2), 353-360.

88.   Takei, T.; Yamazaki, A.; Watanabe, T.; Chikazawa, M., Water Adsorption Properties on Porous Silica Glass Surface Modified by Trimethylsilyl Groups. *Journal of Colloid and Interface Science* **1997,** *188* (2), 409-414.

89.   Klier, K.; Shen, J. H.; Zettlemoyer, A. C., Water on silica and silicate surfaces. I. Partially hydrophobic silicas. *The Journal of Physical Chemistry* **1973,** *77* (11), 1458-1465.

90.   Zettlemoyer, A. C.; Hsing, H. H., Water on silica and silicate surfaces. III. Hexamethyldisilazane-treated silica surfaces. *Journal of Colloid and Interface Science* **1976,** *55* (3), 637-644.

91.   Zettlemoyer, A. C.; Hsing, H. H., Water on organosilane-treated silica surfaces. *Journal of Colloid and Interface Science* **1977,** *58* (2), 263-274.

92.   Sorokin, A. B., Phthalocyanine Metal Complexes in Catalysis. *Chemical Reviews* **2013,** *113* (10), 8152-8191.

93.   Moons, H.; Loas, A.; Gorun, S. M.; Van Doorslaer, S., Photoreduction and light-induced triplet-state formation in a single-site fluoroalkylated zinc phthalocyanine. *Dalton Transactions* **2014,** *43* (40), 14942-14948.

94.   Patel, H. H. Fluorinated Metallo Phthalocyanines for Chemical and Biological Catalysis. Seton Hall University, Seton Hall University Dissertations and Theses (ETDs), 2015.

95.   Bench, B. A.; Beveridge, A.; Sharman, W. M.; Diebold, G. J.; van Lier, J. E.; Gorun, S. M., Introduction of Bulky Perfluoroalkyl Groups at the Periphery of Zinc Perfluorophthalocyanine: Chemical, Structural, Electronic, and Preliminary Photophysical and Biological Effects. *Angewandte Chemie International Edition* **2002,** *41* (5), 747-750.

96.   Patel, P.; Patel, H. H.; Borland, E.; Gorun, S. M.; Sabatino, D., Chemically robust fluoroalkyl phthalocyanine-oligonucleotide bioconjugates and their GRP78 oncogene photocleavage activity. *Chemical Communications* **2014,** *50* (48), 6309-6311.

97.   Ganivet, C. R. Novel Single Molecule Magnets and Photosensitizers for Molecular Photovoltaics based on Customized Phthalocyanines Universidad Autónoma de Madrid, Universidad Autónoma de Madrid, 2015.

98.   Graffius, G. C. Functionalization of Metal Oxide Surfaces through Chemical Reactions and Physical Adsorption. Seton Hall University, Seton Hall University Dissertations and Theses (ETDs), 2016.

99.   Christendat, D.; David, M.-A.; Morin, S.; Lever, A. B. P.; Kadish, K. M.; Shao, J., Synthesis and characterization of highly soluble hexadecachloro- and hexadecafluorophthalocyanine ruthenium(II) complexes. *Journal of Porphyrins and Phthalocyanines* **2005,** *09* (09), 626-636.

100.   Gabrielov, A. G.; Balkus, K. J.; Bell, S. L.; Bedioui, F.; Devynck, J., Faujasite-type zeolites modified with iron perfluorophthalocyanines: Synthesis and characterization. *Microporous Materials* **1994,** *2* (2), 119-126.

101.   Balkus, K. J.; Gabrielov, A. G.; Bell, S. L.; Bedioui, F.; Roue, L.; Devynck, J., Zeolite encapsulated cobalt(II) and copper(II) perfluorophthalocyanines. Synthesis and characterization. *Inorganic Chemistry* **1994,** *33* (1), 67-72.

102.   Bench, B. A.; Brennessel, W. W.; Lee, H.-J.; Gorun, S. M., Synthesis and Structure of a Biconcave Cobalt Perfluorophthalocyanine and Its Catalysis of Novel Oxidative Carbon–Phosphorus Bonds Formation by Using Air. *Angewandte Chemie* **2002,** *114* (5), 776-780.

103.   Ernst, S.; Selle, M., Immobilization and catalytic properties of perfluorinated ruthenium phthalocyanine complexes in MCM-41-type molecular sieves. *Microporous and Mesoporous Materials* **1999,** *27* (2–3), 355-363.

104.   Haber, J.; Block, J. H.; Delmon, B., Manual of methods and procedures for catalyst characterization (Technical Report). In *Pure and Applied Chemistry*, 1995; Vol. 67, p 1257.

105.   Wright, J. D., Gas adsorption on phthalocyanines and its effects on electrical properties. *Progress in Surface Science* **1989,** *31* (1), 1-60.

106.   Gorun, S. M.; Bench, B. A.; Carpenter, G.; Beggs, M. W.; Mague, J. T.; Ensley, H. E., Synthesis and structural characterization of non-planar perfluoro phthalonitriles. *Journal of Fluorine Chemistry* **1998,** *91* (1), 37-40.

107.   Gorun, S. M. L., A. I.; Griswold, K.; Lapok, L.; Patel, H. H.; Gerdes, R. SYSTEM AND METHOD FOR FLUOROALKYLATED FLUOROPHTHALOCYANINES WITH AGGREGATING PROPERTIES AND CATALYTIC DRIVEN PATHWAY FOR OXIDIZING THIOLS 10.05.2012, 2012.

108.   Kubelka, P., *Zeitschrift fur Technische Physik* **1931**, 593-601.

109.   Džimbeg-Malčić, V.; Barbarić-Mikočević, Ž.; Itrić, K., Kubelka-Munk theory in describing optical properties of paper (I). *Tehnički vjesnik* **2011,** *18* (1), 117-124.

110.   Mather, R. R.; Sing, K. S. W., Surface properties of organic pigments. *Journal of Colloid and Interface Science* **1977,** *60* (1), 60-66.

111.   Dwyer, P. J.; Vander Valk, R. J.; Caltaldo, V.; Demianicz, D.; Kelty, S. P., All-Atom CHARMM Force Field and Bulk Properties of Perfluorozinc Phthalocyanines. *The Journal of Physical Chemistry A* **2014,** *118* (49), 11583-11590.